

Theoretical Exploration of Novel Topological States

Longhua Wu

February 2016

Theoretical Exploration of Novel Topological States

Longhua Wu

Doctoral Program in Materials Science and Engineering

Submitted to the Graduate School of
Pure and Applied Sciences
in Partial Fulfillment of the Requirements
for the Degree of Doctor of Philosophy in
Engineering

at the
University of Tsukuba

Abstract

The hallmark discovery of the quantum Hall effect (QHE) in two-dimensional (2D) electron gases opened a new chapter in condensed matter physics [1]. The underlying mechanism for exact quantization of Hall conductance σ_{xy} was explained from perspectives of gauge invariance and edge currents in a finite sample [2, 3]. A relationship between σ_{xy} and nontrivial bulk topology of Bloch wave functions $\sigma_{xy} = ne^2/h$ was later revealed [4], where integer n is the Chern number evaluated by using Bloch wave functions. A one-to-one correspondence between the two theories was clarified by Hatsugai, known as bulk-edge correspondence [5]. One necessary condition for achieving the ordinary QHE is strong external magnetic fields. It has been shown by Haldane that the condition can be exempted in a 2D honeycomb lattice with complex next-nearest-neighbor (NNN) hopping integrals taken into consideration [6], and a quantum anomalous Hall effect (QAHE) is then realized. Due to broken time-reversal (TR) symmetry, both QHE and QAHE are classified as Chern insulators, which can support chiral edge states. A breakthrough took place in 2005 when Kane and Mele demonstrated that the intrinsic spin-orbit coupling (SOC) in monolayer graphene can generate the complex NNN hopping integrals [7–9] and drives the system into a quantum spin Hall effect (QSHE) preserving TR symmetry. The QSHE is characterized by a \mathbb{Z}_2 topological invariant and can support helical edge states. Experimental observations of QSHE in graphene are almost impossible due to the extremely small SOC. A larger gap 2D topological insulator CdTe/HgTe/CdTe quantum well was later theoretically studied and experimentally confirmed [10, 11].

In the thesis, we focus on studying topological states in photonics, semiconductors and superconductors including both theories and material designs. We start from topological photonics. Photonic crystals are analogues of conventional crystals with atomic lattice replaced by a medium of periodic electric permittivity and/or magnetic permeability. Due to the periodicity, both Bloch and topological band theory [9] apply to photonic crystals as well. A honeycomb lattice of 2D cylindrical dielectric rods can support Dirac cones at the $K(K')$ points, which are the corner of the Brillouin zone for honeycomb lattice. Breaking the TR symmetry by introducing the magneto-optic effect into honeycomb lattice, the system is driven into a topological phase under strong external magnetic field [12]. The resultant topological state can be regarded as an optical analogue of the ordinary QHE. Without requiring any external field, we derive a 2D \mathbb{Z}_2 topological photonic state purely based on conventional dielectric materials [13]. Starting with a honeycomb lattice of cylinders, we group them into a triangular lattice of cylinder hexagons [see figure 1(a)], which can support double Dirac cones at the Γ point [14, 15]. Detuning the lattice constant of the triangular lattice, we realize a \mathbb{Z}_2 topological photonic state with bulk band gap opened at the Γ point. The photonic topology is associated with a pseudo-TR symmetry constituted by the TR symmetry respected in general by Maxwell equations and the C_6 crystal symmetry upon design, rendering the Kramers doubling in the present photonic system. We prove for the transverse magnetic mode that the role of pseudospin is played by the angular momentum of the wave function of the out-of-plane electric field. We solve Maxwell equations and demonstrate the new photonic topology by revealing pseudospin-resolved Berry curvatures of photonic bands and helical edge states characterized by Poynting vectors. With simple design backed up by the symmetry consideration, the present topological photonic crystal can be fabricated easily, and is expected to leave impacts on topological photonics and related materials science.

The size of the photonic band gap can be tuned by varying lattice constants [13], making it possible for realizing a topological state with large band gap. We generalize the idea of achieving topological

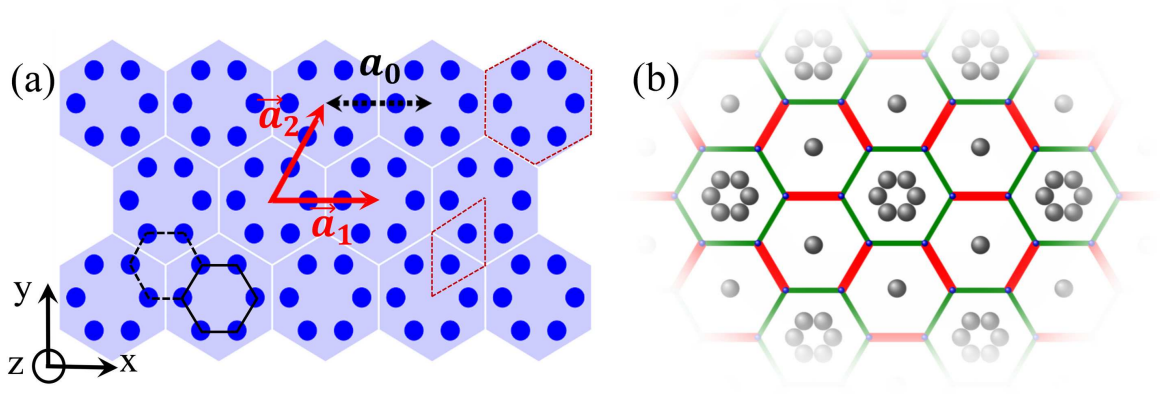


Figure 1: (a) Schematic plot of a triangular photonic crystal of “artificial atoms” composed by six cylinders of dielectric material. Red dashed rhombus and hexagon are primitive cells of honeycomb and triangular lattices. \vec{a}_1 and \vec{a}_2 are unit vectors with length a_0 as the lattice constant. (b) Honeycomb lattice with enhanced inter-hexagon hopping energies (thick red bonds) compared to intra-hexagon hopping energies (thin green bonds). Gray balls are CO molecules that modulate electron gases on Cu [111] surface.

photonics to topological insulators [16]. Starting with a honeycomb lattice and viewing it as a triangular lattice of hexagons, we propose a \mathbb{Z}_2 topological state by simply enhancing inter-hexagon hopping energies over intra-hexagon ones [see figure 1(b)]. We reveal that this manipulation opens a gap in the energy dispersion at the Γ point and drives the system into a \mathbb{Z}_2 topological state. The size of the topological gap is proportional to the difference of the inter-hexagon and the intra-hexagon hopping energies, which can be larger than typical SOC by orders of magnitude and potentially renders topological electronic transports available at high temperatures. For experimental implementations, we discuss that, along with many other possibilities, the molecular graphene with carbon monoxides (CO) placed periodically on Cu [111] surface is a very promising platform to realize the present idea, where the hopping texture can be controlled by adding extra CO molecules, as shown in figure 1(b). The present work offers a new possibility for achieving topological properties and related novel quantum properties and functionalities at high temperatures.

By breaking TR and inversion symmetries, we propose a novel QAHE characterized by simultaneous charge and spin Chern numbers [17–19], which can support non-dissipative spin-polarized edge currents in a finite sample [see figure 2(a)]. We have shown that a possible system which can host the novel QAHE is a buckled honeycomb lattice with anti-ferromagnetic (AFM) exchange field \mathbf{M} at two sublattice sites, intrinsic SOC λ and tunable electric field \mathbf{E} [17]. When magnitudes of \mathbf{M} , λ and \mathbf{E} form a triangular relation, the novel QAHE is achieved. By performing first-principles calculations, we have shown that a G-type AFM Mott insulator LaCrO_3 grown along the [111] direction with one layer of Cr atom replaced by Au or Ag can support the novel QAHE. Nevertheless, it turns out that synthesizing the system along the [111] direction is not an easy task. We further propose a sandwiched structure composed of the LaCrO_3 grown along the [001] direction with one atomic layer replaced by an inverse perovskite material Sr_3PbO [19], as shown in figure 2(b). Based on first-principles calculations, we confirm that the system is in the novel QAHE by demonstrating nonzero charge and spin Chern numbers as well as spin-polarized edge states. Since both LaCrO_3 and Sr_3PbO are stable in bulk and match each

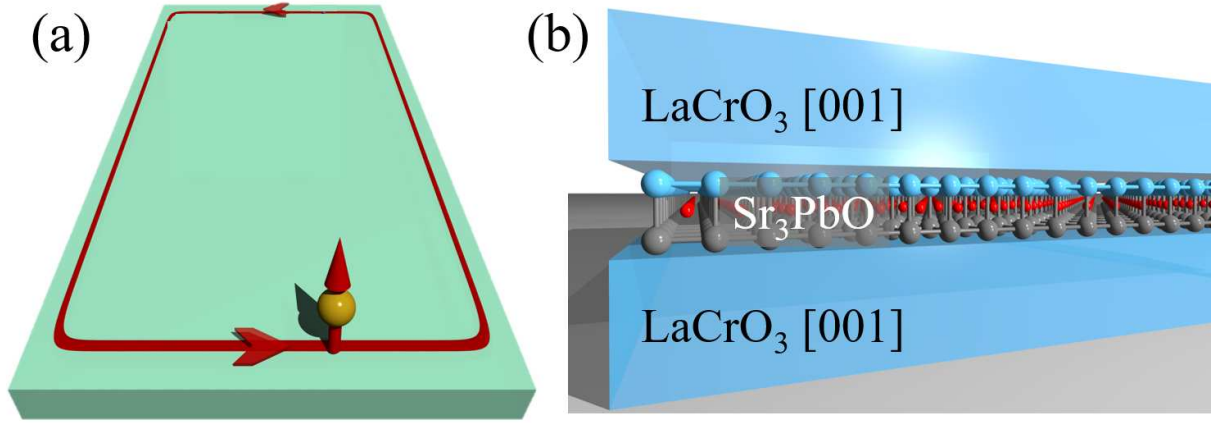


Figure 2: (a) Spin-polarized edge states at a sample edge. (b) Schematics for host perovskite material LaCrO_3 in the $[001]$ direction (blue slabs) with one atomic layer of inverse perovskite material Sr_3PbO (gray layer) inserted. Gray, red and blue balls stand for Pb, O and Cr atoms respectively.

other with small lattice distortions, the composite material is expected easy to synthesize. This novel QAHE with non-dissipative spin-polarized edge currents is robust to both non-magnetic and magnetic defects, and is thus ideal for spintronics applications with spin polarizations controlled by a gate voltage.

An important and promising application of topological states is fault-tolerance topological quantum computing. Majorana fermion (MF), a zero-energy quasi-particle that is its own anti-particle, is the key to realize novel quantum functionalities. We study topological superconductivities in a heterostructure composed of a ferromagnetic insulator, a semiconductor with strong Rashba SOC and an s -wave superconductor with vortices [20, 21], as shown figure 3(a). Non-Abelian statistics can be achieved by exchanging two vortices hosting MFs [22]. However, in experiments it is difficult to manipulate vortices. In order to circumvent this difficulty, we propose a new way to interchange MFs without moving vortices. The only operation required is to turn on and off local gate voltages [23], which liberates a MF from its original host vortex and transports it along prepared tracks, as shown in figure 3(b). We solve the time-dependent Bogoliubov-de Gennes equation numerically, and confirm that the MFs are protected provided the switching of gate voltages for exchanging MFs are adiabatic, which takes only several nano seconds given reasonable material parameters. By monitoring the time evolution of MF wave functions, we show that non-Abelian statistics is achieved. The present scheme provides a feasible way manipulating MFs and is expected to be useful in topological quantum computing.

This thesis

This thesis includes discussions of achieving novel topologically nontrivial states in photonic crystals, semiconductors as well as superconductors. In chapter 1, a brief review on developments of topological theories is given, which includes topological invariants for characterizing nontrivial states, topological models as well as materials. In chapter 2, we propose a novel topological photonic crystal purely made of conventional dielectric materials, such as silicon. The topological properties are demonstrated via an effective low-energy model, helical edge states and \mathbb{Z}_2 topological invariants. In chapter 3, we extend the theory of achieving topological photonic states to electronic systems with honeycomb lat-

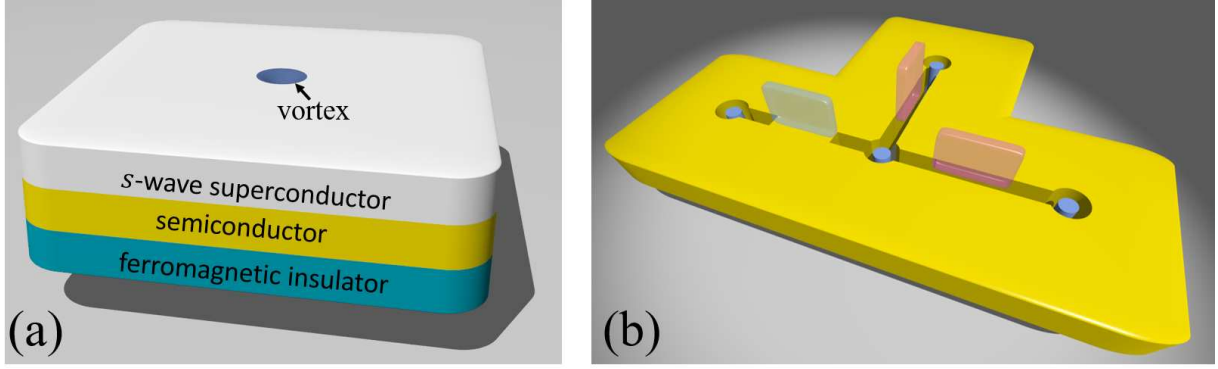


Figure 3: (a) A heterostructure of s -wave superconductor with a vortex, spin-orbit coupling semiconductor and ferromagnetic insulator. (b) Schematic device setup for braiding MFs at vortex cores (blue cylinder). There are four holes in semiconductor layer (yellow platform) with one superconducting vortex pinned right beneath each of them. The electrodes at high-voltage states (pink rectangular prisms) prohibit electron hoppings in the regions below them, and thus connect effectively the holes; the blue rectangular prism denotes an electrode at zero-voltage state.

tice simply by detuning lattice constants to form a Kekulé hopping texture. A topological band gap pure of electronic origins can be orders of magnitude larger than that opened by spin-orbit couplings due to relativistic effects. In chapter 4, we derive a novel quantum anomalous Hall effect characterized by simultaneous charge and spin Chern numbers by first-principles calculations. We confirm that a G-type Mott insulator LaCrO_3 grown along the $[001]$ direction with one atomic layer replaced by a inverse-perovskite material Sr_3PbO can support the novel quantum anomalous Hall effect. In chapter 5, we study topological superconductivities of a heterostructure composed of an s -wave superconductor with vortices, a semiconductor with strong Rashba-type spin-orbit coupling and a ferromagnetic insulator. A new scheme that only requires tuning of local gate voltages is proposed for braiding Majorana fermions hosted by vortices to achieve non-Abelian statistics. Conclusion and outlook are given in the last chapter.

Contents

Contents	5
1 Background: Topological Invariants, Materials and Models	9
1.1 Introduction	9
1.2 Topological invariants	10
1.2.1 Berry curvatures and Chern numbers	10
1.2.2 Symmetries and Berry curvatures	11
1.2.3 Berry curvatures for a 2×2 Dirac Hamiltonian	12
1.3 Topological materials and models	14
1.3.1 Chern numbers and quantum anomalous Hall effect	14
1.3.2 \mathbb{Z}_2 invariants and quantum spin Hall effect	14
1.4 Edge states at a phase transition point	18
2 A \mathbb{Z}_2 Topological Phase in an All-Dielectric Photonic Crystal	21
2.1 Maxwell equations	21
2.2 Dirac cones and topology in photonic crystals	22
2.3 Topological photonics characterized by \mathbb{Z}_2 invariant	24
2.3.1 Two-dimensional photonic crystals	24
2.3.2 Time-reversal symmetry of Maxwell equations	25
2.3.3 Pseudo-time-reversal symmetry	26
2.3.4 Pseudospins: orbital angular momentum of electric fields	29
2.4 Topological phase transitions	29
2.5 $\mathbf{k} \cdot \mathbf{P}$ model for topological photonic crystals	30
2.6 Topological edge states in photonic crystals	33
2.6.1 Edge state in 2D systems	33
2.6.2 Energy propagations via topological edge states	34
2.6.3 Experimental realizations	37
2.7 Conclusion	38
3 Honeycomb Lattice with Kekulé Distortions	39
3.1 Honeycomb lattice	39
3.1.1 Tight-binding model	39

3.1.2	Topological phases in honeycomb lattice	39
3.2	Topological properties induced by Kekulé hopping textures	41
3.2.1	Tight-binding model and emergent orbitals	41
3.2.2	Pseudo-time-reversal symmetry and pseudospin	43
3.3	Low-energy model for \mathbb{Z}_2 topological states	44
3.4	Topological phase transitions	46
3.5	Topological edge states and associated conductances	47
3.5.1	Helical edge states	47
3.5.2	Six-terminal Hall and longitudinal conductances	47
3.6	Real spin, spin-orbit coupling and QSHE	50
3.6.1	Low-energy model with SOC	50
3.7	Possible experimental realizations	51
3.8	Conclusion	52
4	Novel Quantum Anomalous Hall Effect in Perovskites Materials	55
4.1	Introduction of quantum anomalous Hall effect	55
4.2	Novel QAHE in square lattice	57
4.2.1	First-principles calculations	57
4.2.2	Effective low-energy model	60
4.2.3	Topological edge states	63
4.3	Novel QAHE in honeycomb lattice	63
4.3.1	Tight-binding model	63
4.3.2	Topological phases	64
4.3.3	Spin-polarized edge state	65
4.3.4	Robustness of the novel QAHE against Rashba-type SOC	66
4.4	Conclusion	70
5	Majorana Fermions in Topological Superconductors	71
5.1	Introduction	71
5.1.1	Majorana states	71
5.1.2	Realizations of Majorana fermions	72
5.2	Topological superconductivity	74
5.2.1	Hamiltonian in momentum space and Chern number	74
5.3	Manipulations of core Majorana fermions	76
5.3.1	Core Majorana fermions	76
5.3.2	Transportation of Majorana fermions	76
5.3.3	Braiding of Majorana fermions	78
5.3.4	Time-dependent Bogoliubov-de Gennes equation	78
5.4	Comparisons with other proposals for braiding Majorana fermions	80
5.4.1	Braiding Majorana fermions in two-dimensional p -wave superconductors	80
5.4.2	Braiding Majorana fermions in nanowire networks	83
5.5	Conclusion	86
6	Conclusion and Outlook	87

Acknowledgments	89
Bibliography	91
List of Publications	99
A Low-Energy Model for Honeycomb Lattice	101
A.1 Honeycomb lattice and Dirac cones	101
A.2 Hamiltonian on basis of sublattice	104
B Winding Number and One-Dimensional Kitaev Model	105

Background: Topological Invariants, Materials and Models

1.1 Introduction

The first topological invariant (the Chern number) was studied by Thouless, Kohmoto, Nightingale and Nijs in 1982 [4], which signals the topological properties of quantum Hall effect (QHE) by having a nonzero Chern number and explains the quantizations of Hall conductance discovered by von Klitzing [1]. A generalization of the QHE was suggested by Haldane by breaking time-reversal symmetry with complex next-nearest-neighbor hopping integrals in honeycomb lattice instead of using external magnetic fields [6], which is known as quantum anomalous Hall effect (QAHE). Because all symmetries are broken, both QHE and QAHE belong to the topological class *A* [24, 25], characterized by \mathbb{Z} invariants in two-dimensional (2D) systems. Kane and Mele revealed that the spin-orbit coupling (SOC) in monolayer graphene can effectively generate the complex next-nearest-neighbor hopping integrals in honeycomb lattice and drive the system into a quantum spin Hall effect (QSHE) [7–9], which belongs to the topological class *AII* characterized by \mathbb{Z}_2 invariants due to the preservation of time-reversal symmetry [24, 25]. QSHE was also studied in a 2D CdTe/HgTe/CdTe quantum well both theoretically and experimentally [10, 11, 26].

Investigations on topological photonics have been undergoing parallelly with developments of topological insulators. The first topological photonic state was studied theoretically in a metamaterial with the magneto-optical effect (or the Faraday effect) [12]. The authors considered a hexagonal array of 2D metamaterial cylinders, which supports Dirac cones at the K and K' points at the corner of the Brillouin zone when both inversion and time-reversal symmetries are preserved. Breaking the time-reversal symmetry with a strong external magnetic field, the system is driven into a topological nontrivial state characterized by the Chern number, which can support a chiral edge state in a finite sample. This topological state in photonics is also known as optical QHE. Experimental realizations of the one-way topological edge states in photonic crystals were demonstrated successfully in a square lattice of 2D metamaterials [27, 28]. Instead of requiring actual external magnetic fields to achieve the optical QHE, several studies suggested to realize optical QHE by effective magnetic fields via modulating couplings between lattice sites periodic in time [29] or fabricating a helical structure [30]. To realize a topological state preserving the time-reversal symmetry, an analogue of the QSHE in electronic systems [7, 8, 10],

one has to construct Kramers doublets. It has been shown that the role of pseudospins can be played by clockwise/anticlockwise circulations of light in a coupled resonator optical waveguide [31, 32] as well as the bonding/antibonding of electric and magnetic fields in bi-anisotropic metamaterials [33].

1.2 Topological invariants

1.2.1 Berry curvatures and Chern numbers

A topologically nontrivial state is signaled by nonzero invariants, which is evaluated by using Bloch wave functions of bulk systems [4]. The eigenfunction $\Psi_{\mathbf{k}}$ of a Hamiltonian $H(\mathbf{k})$ satisfies

$$H_{\mathbf{k}}\Psi_{\mathbf{k}}(\mathbf{r}) = E(\mathbf{k})\Psi_{\mathbf{k}}(\mathbf{r}), \quad (1.1)$$

where $E(\mathbf{k})$ is the eigenenergy at the \mathbf{k} point, the Bloch wavefunction is $\Psi_{\mathbf{k}}(\mathbf{r}) = u_{\mathbf{k}}(\mathbf{r})\exp(i\mathbf{k} \cdot \mathbf{r})$ with $u_{\mathbf{k}}(\mathbf{r})$ a spatially periodic function. The Chern number is

$$\begin{aligned} C &= \frac{1}{2\pi i} \sum_{j \in \text{occupied}} \int_{\mathbf{k}^2} d^2\mathbf{k} \cdot [\vec{\nabla}_{\mathbf{k}} \times \langle u_j | \vec{\nabla}_{\mathbf{k}} | u_j \rangle] \\ &= \frac{1}{2\pi i} \sum_{j \in \text{occupied}} \int_{\mathbf{k}^2} d^2\mathbf{k} \cdot \vec{\nabla}_{\mathbf{k}} \times \left(u_j^* \frac{\partial u_j}{\partial k_x} \hat{k}_x + u_j^* \frac{\partial u_j}{\partial k_y} \hat{k}_y \right) \\ &= \frac{1}{2\pi i} \sum_{j \in \text{occupied}} \int_{\mathbf{k}^2} d^2\mathbf{k} \cdot \vec{\nabla}_{\mathbf{k}} \times \vec{\mathcal{A}}_{j,\mathbf{k}} \\ &= \frac{1}{2\pi i} \sum_{j \in \text{occupied}} \int_{\mathbf{k}^2} d^2\mathbf{k} \cdot \vec{\Omega}_{j,\mathbf{k}}, \end{aligned} \quad (1.2)$$

where u_j is the $u_{\mathbf{k}}(\mathbf{r})$ for the band j , $\hat{k}_{x/y}$ is the unit vector along the $\vec{k}_{x/y}$ direction, $\vec{\mathcal{A}}_{j,\mathbf{k}} = \langle u_j | \vec{\nabla}_{\mathbf{k}} | u_j \rangle$ and $\vec{\Omega}_{j,\mathbf{k}} = \vec{\nabla}_{\mathbf{k}} \times \vec{\mathcal{A}}_{j,\mathbf{k}}$ are the Berry connection and Berry curvature of the band j at the point \mathbf{k} respectively, and the Chern number is a summation of Berry curvatures over all occupied bands. Because that the spatial function $u_{\mathbf{k}}$ remains a solution for Eq. (1.1) when multiplied by an arbitrary gauge $\exp[i\chi(\mathbf{k})]$, the Berry connection $\vec{\mathcal{A}}$ is thus gauge-dependent:

$$|u_{\mathbf{k}}\rangle \rightarrow \exp[i\chi(\mathbf{k})]|u_{\mathbf{k}}\rangle, \quad \vec{\mathcal{A}} \rightarrow \vec{\mathcal{A}} + i\partial_{\mathbf{k}}\chi(\mathbf{k}). \quad (1.3)$$

Therefore, an explicit gauge fixing is necessary to obtain a well defined Chern number generally [34, 35]. However, the gauge fixing can be difficult to implement numerically. In the current work, we adopt an efficient method for evaluating Chern numbers without specifying gauge-fixing conditions as proposed by Fukui, Hatsugai and Suzuki [36]. The above integral in Eq. (1.2) over the whole Brillouin zone can

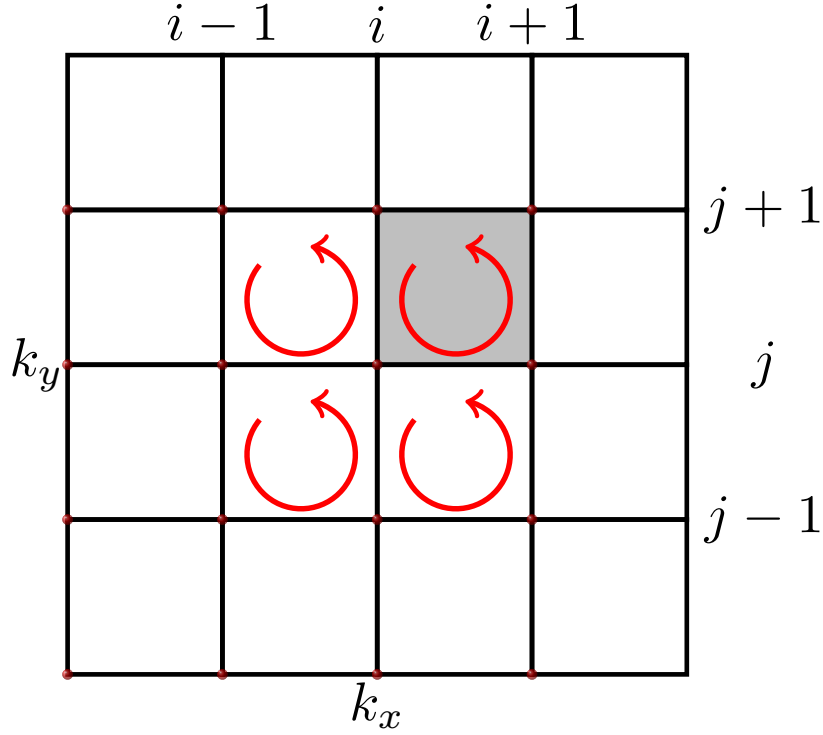


Figure 1.1: Contour integrations for evaluating Berry curvatures in the Brillouin zone. i and j are the indices of mesh grid of the Brillouin zone. Contour integration is performed along the direction of red curves.

be decomposed into contour integrations over discretized patches [36, 37] (see figure 1.1)

$$\begin{aligned}
 \int_S d^2\mathbf{k} \cdot \vec{\Omega}_{\mathbf{k}} &= \oint_{\partial S} d\mathbf{k} \cdot \vec{\mathcal{A}}_{\mathbf{k}} = \int_{\mathbf{k}_{i,j}}^{\mathbf{k}_{i+1,j}} d\mathbf{k} \cdot \vec{\mathcal{A}}_{\mathbf{k}} + \int_{\mathbf{k}_{i+1,j}}^{\mathbf{k}_{i+1,j+1}} d\mathbf{k} \cdot \vec{\mathcal{A}}_{\mathbf{k}} \\
 &\quad + \int_{\mathbf{k}_{i+1,j+1}}^{\mathbf{k}_{i,j+1}} d\mathbf{k} \cdot \vec{\mathcal{A}}_{\mathbf{k}} + \int_{\mathbf{k}_{i,j+1}}^{\mathbf{k}_{i,j}} d\mathbf{k} \cdot \vec{\mathcal{A}}_{\mathbf{k}} \\
 &= \langle u_{\mathbf{k}_{i,j}} | u_{\mathbf{k}_{i+1,j}} \rangle + \langle u_{\mathbf{k}_{i+1,j}} | u_{\mathbf{k}_{i+1,j+1}} \rangle - \langle u_{\mathbf{k}_{i+1,j+1}} | u_{\mathbf{k}_{i,j+1}} \rangle - \langle u_{\mathbf{k}_{i,j+1}} | u_{\mathbf{k}_{i,j}} \rangle
 \end{aligned} \tag{1.4}$$

where S and ∂S are the shaded region and its boundary respectively as shown in figure 1.1, $\mathbf{k}_{i,j}$ is the position of the grid point (i, j) in the Brillouin zone. The total Chern number is then

$$C = \frac{1}{2\pi i} \sum_S \int_S d^2\mathbf{k} \cdot \vec{\Omega}_{\mathbf{k}}. \tag{1.5}$$

In this way the Chern number in Eq. (1.4) can be evaluated efficiently.

1.2.2 Symmetries and Berry curvatures

For an electronic system preserving the time-reversal symmetry $\mathcal{T}_e = i\sigma_y \mathcal{K}$ with $\mathcal{T}_e^2 = -1$, it can be proven easily that the Chern number vanishes. Assuming that $u_{\mathbf{k}}^\alpha$ is an eigensolution of the system,

we immediately obtain the wavefunction of its time-reversal partner $u_{-\mathbf{k}}^\beta = \mathcal{T}_e u_{\mathbf{k}}^\alpha$. The Berry curvature for the $u_{\mathbf{k}}^\beta$ is

$$\begin{aligned}\vec{\Omega}_{-\mathbf{k}}^\beta &= \left\langle \frac{\partial \mathcal{T}_e u_{\mathbf{k}}^\alpha}{\partial k_x} \middle| \frac{\partial \mathcal{T}_e u_{\mathbf{k}}^\alpha}{\partial k_y} \right\rangle - \left\langle \frac{\partial \mathcal{T}_e u_{\mathbf{k}}^\alpha}{\partial k_y} \middle| \frac{\partial \mathcal{T}_e u_{\mathbf{k}}^\alpha}{\partial k_x} \right\rangle \\ &= \overline{\left\langle \frac{\partial u_{\mathbf{k}}^\alpha}{\partial k_x} \middle| \frac{\partial u_{\mathbf{k}}^\alpha}{\partial k_y} \right\rangle} - \overline{\left\langle \frac{\partial u_{\mathbf{k}}^\alpha}{\partial k_y} \middle| \frac{\partial u_{\mathbf{k}}^\alpha}{\partial k_x} \right\rangle} \\ &= \left\langle \frac{\partial u_{\mathbf{k}}^\alpha}{\partial k_y} \middle| \frac{\partial u_{\mathbf{k}}^\alpha}{\partial k_x} \right\rangle - \left\langle \frac{\partial u_{\mathbf{k}}^\alpha}{\partial k_x} \middle| \frac{\partial u_{\mathbf{k}}^\alpha}{\partial k_y} \right\rangle \\ &= -\vec{\Omega}_{\mathbf{k}}^\alpha,\end{aligned}\tag{1.6}$$

which indicates that the Berry curvature is an odd function under the time-reversal operation, where $\overline{\langle \cdot | \cdot \rangle}$ is the complex conjugate of the complex number $\langle \cdot | \cdot \rangle$. From the first line to the second one in Eq. (1.6), we apply the rule $\langle Ux | Uy \rangle = \overline{\langle x | y \rangle} = \langle y | x \rangle$, according to the definition of anti-unitary operator U . Therefore, for a time-reversal symmetric system the Chern number is always zero, and hence it can not be used to differentiate topological phases from trivial ones in this case.

Similarly, it is straightforward to show that the Berry curvature is an even function under the spatial inversion symmetry \mathcal{P} for any eigensolution $u_{\mathbf{k}}^\alpha$. The Berry curvature evaluated by the eigenstate $u_{-\mathbf{k}}^\beta = \mathcal{P} u_{\mathbf{k}}^\alpha$ is

$$\begin{aligned}\vec{\Omega}_{-\mathbf{k}}^\beta &= \left\langle \frac{\partial \mathcal{P} u_{\mathbf{k}}^\alpha}{\partial k_x} \middle| \frac{\partial \mathcal{P} u_{\mathbf{k}}^\alpha}{\partial k_y} \right\rangle - \left\langle \frac{\partial \mathcal{P} u_{\mathbf{k}}^\alpha}{\partial k_y} \middle| \frac{\partial \mathcal{P} u_{\mathbf{k}}^\alpha}{\partial k_x} \right\rangle \\ &= \left\langle \frac{\partial u_{\mathbf{k}}^\alpha}{\partial k_x} \middle| \frac{\partial u_{\mathbf{k}}^\alpha}{\partial k_y} \right\rangle - \left\langle \frac{\partial u_{\mathbf{k}}^\alpha}{\partial k_y} \middle| \frac{\partial u_{\mathbf{k}}^\alpha}{\partial k_x} \right\rangle = \vec{\Omega}_{\mathbf{k}}^\alpha,\end{aligned}\tag{1.7}$$

since the inversion operator \mathcal{P} is a unitary one.

1.2.3 Berry curvatures for a 2×2 Dirac Hamiltonian

We now derive Berry curvatures for a generic Dirac Hamiltonian

$$H_{\text{Dirac}} = \sum_{i=x,y,z} d_i \cdot \sigma_i\tag{1.8}$$

with σ_i the Pauli matrices and the vector $\vec{d} = (d_x, d_y, d_z)$. Parameterizing the vector \vec{d} into the spherical coordinate by letting $\vec{d}_s = |\vec{d}|(\sin \theta \cos \phi, \sin \theta \sin \phi, \cos \theta)$ with $|\vec{d}|$ the length of $|\vec{d}|$, we can easily obtain two eigenvalues $\pm |\vec{d}|$ with corresponding eigenfunctions

$$u_+ = \begin{bmatrix} \cos(\theta/2) \exp(-i\phi) \\ \sin(\theta/2) \end{bmatrix}, \quad u_- = \begin{bmatrix} \sin(\theta/2) \exp(-i\phi) \\ -\cos(\theta/2) \end{bmatrix}.\tag{1.9}$$

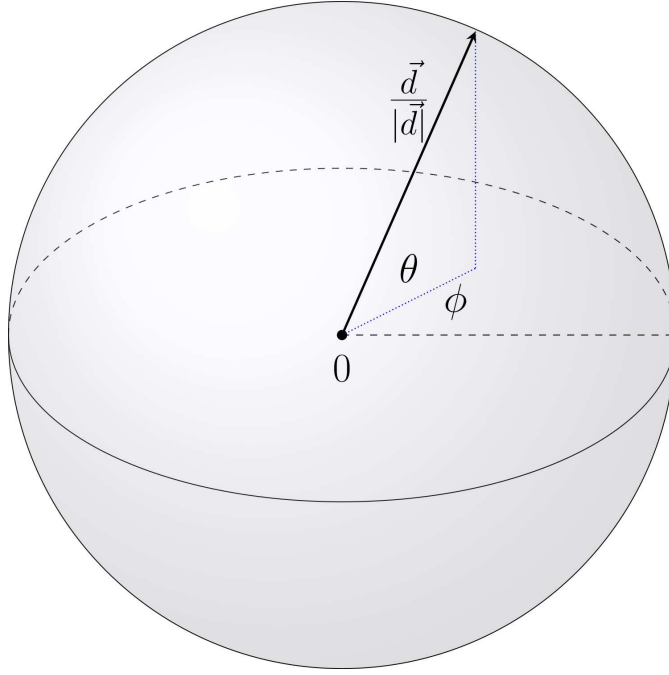


Figure 1.2: A sphere wrapped by the unit $\vec{d}/|\vec{d}|$ vector, θ and ϕ are polar and azimuth angles of the unit vector.

The Berry curvature for the lower energy state u_- in the spherical coordinate is

$$\vec{\Omega}_{\text{spherical}} = (\partial_\theta \mathcal{A}_\phi - \partial_\phi \mathcal{A}_\theta) \frac{\vec{d}}{|\vec{d}|} = i \frac{\sin \theta}{2} \frac{\vec{d}}{|\vec{d}|}, \quad (1.10)$$

where $\mathcal{A}_\theta = \langle u_+ | \partial_\theta | u_+ \rangle = 0$ and $\mathcal{A}_\phi = \langle u_+ | \partial_\phi | u_+ \rangle = -i \sin^2(\theta/2)$. Transforming the Berry curvature $\vec{\Omega}_s$ back into the rectangular coordinate, we have

$$\vec{\Omega}_{\text{rect}} = \frac{1}{\sin \theta |\vec{d}|^2} \vec{\Omega}_{\text{spherical}} = \frac{i}{2} \cdot \frac{\vec{d}}{|\vec{d}|^3}. \quad (1.11)$$

The distribution of above $\vec{\Omega}_{\text{rect}}$ is similar to the one generated by a magnetic monopole located at the origin. It is then always said that there is a magnetic monopole in the Brillouin zone of the Chern insulators.

The range of ϕ is $[0, 2\pi]$ since the vector \vec{d} can cover the whole unit sphere as \mathbf{k} changes (see figure 1.2). The θ takes

$$\theta \in \begin{cases} (0, \pi/2) & \text{if } d_z > 0, \\ (\pi/2, \pi) & \text{otherwise.} \end{cases}$$

Let us consider a simple Dirac Hamiltonian

$$H_{\text{Dirac}}(\mathbf{k}) = \begin{pmatrix} C & k_x + i k_y \\ k_x - i k_y & -C \end{pmatrix}, \quad (1.12)$$

with $C > 0$. It is easy to see that in this case the ϕ ranges from 0 to 2π and $\theta \in (0, \pi/2)$. Integrating the Berry curvature over the half sphere with unit radius, the Chern number is

$$C = \frac{1}{2\pi i} \int_{\theta, \phi} d\theta d\phi \frac{i \sin \theta}{2} = \frac{1}{2\pi} \int_0^{2\pi} d\phi \int_0^{\pi/2} d\theta \frac{\sin \theta}{2} = \frac{1}{2}, \quad (1.13)$$

indicating every Dirac fermion contributes $1/2$ to the Chern number, half of a magnetic monopole.

1.3 Topological materials and models

1.3.1 Chern numbers and quantum anomalous Hall effect

The time-reversal symmetry of the QHE discovered by von Klitzing [1] is broken by external magnetic field. It was first noticed by Haldane that the time-reversal symmetry can be broken by introducing complex next-nearest-neighbor hopping integrals in honeycomb lattice [6], which drive the system into a quantum anomalous Hall effect (QAHE) characterized by the Chern numbers. The Haldane model paves a new way for realizing Chern insulators without requiring any external magnetic field. As displayed in figure 1.3, one considers a honeycomb lattice with the nearest-neighbor hopping integrals t and the next-nearest-neighbor hopping integrals t' . The effective low-energy Hamiltonian for the system around the $K(K')$ points up to the lowest order of \mathbf{k} is (see detailed derivations in Appendix A.1)

$$H(\mathbf{k}) = -3t_1 \cos \phi \sigma_0 + \begin{pmatrix} 3\sqrt{3}\nu t_1 \sin \phi & -\sqrt{3}at(k_x - i\nu k_y)/2 \\ -\sqrt{3}at(k_x + i\nu k_y)/2 & -3\sqrt{3}\nu t_1 \sin \phi \end{pmatrix} \quad (1.14)$$

on the sublattice basis $[A, B]$, where where $t' = t_1 \exp(i\phi)$ with $t_1 = |t'|$ the real number and ϕ the phase of hopping integral t' , $\nu = \pm 1$ at the K and K' points respectively, k_x and k_y are measured from the $K(K')$ points, σ_0 is a 2×2 identity matrix. Since the first term in the above equation simply shifts all energy levels without affecting topology, it can be dropped for discussions of topology.

For $\phi \in (0, \pi)$, the sign of $d_z = 3\sqrt{3}\nu t_1 \sin \phi$ is positive (negative), which gives us $-1/2$ at both the K and K' points and results in a QAHE with Chern number -1 . Similar analyses can be carried for $\phi \in (\pi, 2\pi)$, where the system is in a QAHE with the Chern number 1 [6].

1.3.2 \mathbb{Z}_2 invariants and quantum spin Hall effect

We have shown in Section 1.2.2 that the Chern number is always zero in a system preserving the time-reversal symmetry, it thus can not be used to differentiate a QSHE from a trivial state. Another type of topological invariants is necessary to characterize QSHE. It has been suggested that the \mathbb{Z}_2 topological invariants are capable of separating a QSHE from a trivial state [7, 8, 24, 25]. By dividing total eigensolution spaces of occupied bands into two subspaces that are linked by the (pseudo-)time-reversal symmetry, one then can define the Chern numbers within each subspace. For each subspaces, the Chern number is guaranteed to be nonzero due to the absences of the (pseudo-)time-reversal symmetry. In this spirit, the \mathbb{Z}_2 topological invariants can be simply understood as the difference between the Chern numbers of the two subspaces. In conventional electronic systems with the time-reversal symmetry, one can

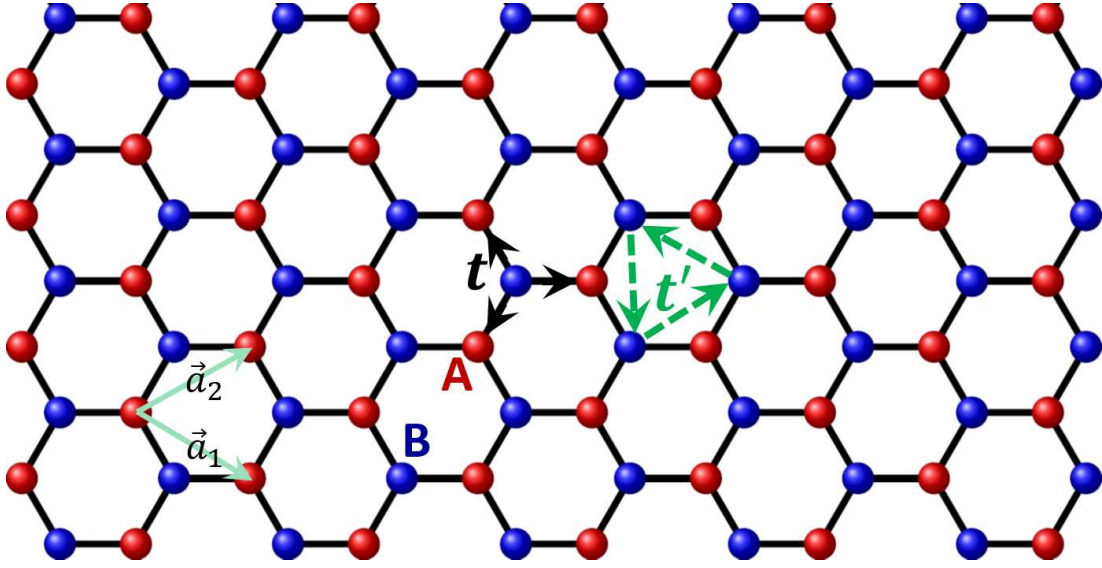


Figure 1.3: Schematic honeycomb lattice with sublattice A and B marked by red and blue balls respectively. Black solid and green dashed arrays represent nearest-neighbor and next-nearest-neighbor hoppings respectively.

divide the total eigenspaces by the spins of electrons, the \mathbb{Z}_2 topological invariant is then

$$\zeta = \frac{1}{2}(C_{\uparrow} - C_{\downarrow}) \quad (1.15)$$

with $C_{\uparrow/\downarrow}$ the Chern number for spin-up/-down channel.

The first example of a system characterized by a nonzero \mathbb{Z}_2 topological invariant was studied by Kane and Mele [7, 8]. The authors considered a spinful monolayer graphene with intrinsic spin-orbit coupling (SOC). It was pointed out that the intrinsic SOC can generate the complex next-nearest-neighbor hopping integrals with $\phi = \pi/2$ in Eq. (1.14). For one spin channel, it is equivalent to the QAHE studied by Haldane [6]. As for the other spin channel, the Chern number must take an opposite value due to the oddness of Berry curvatures under the time-reversal operator [see Eq. (1.6)]. As a result, the monolayer graphene with the intrinsic SOC has a zero total Chern number but a nonzero \mathbb{Z}_2 topological invariant, which is known as QSHE.

Another typical example of \mathbb{Z}_2 topological systems is the CdTe/HgTe/CdTe quantum well, which is described by the Bernevig-Hughes-Zhang (BHZ) model [10]

$$H_{\text{eff}}(\mathbf{k}) = \begin{bmatrix} H(\mathbf{k}) & 0 \\ 0 & H^*(-\mathbf{k}) \end{bmatrix} \text{ with } H(\mathbf{k}) = \varepsilon(\mathbf{k}) + \sum_{i=x,y,z} d_i(\mathbf{k}) \cdot \vec{\sigma}_i \quad (1.16)$$

on the basis $[|s^{\uparrow}\rangle, |p_+^{\uparrow}\rangle, |s^{\downarrow}\rangle, |p_-^{\downarrow}\rangle]$ with $p_{\pm} = (p_x \pm ip_y)/\sqrt{2}$, where $\vec{\sigma}_i$ are the Pauli matrices, $|s\rangle$ and $|p_{\pm}\rangle$ orbitals closing to the Fermi level are contributed by the Hg and the Te atoms respectively, and

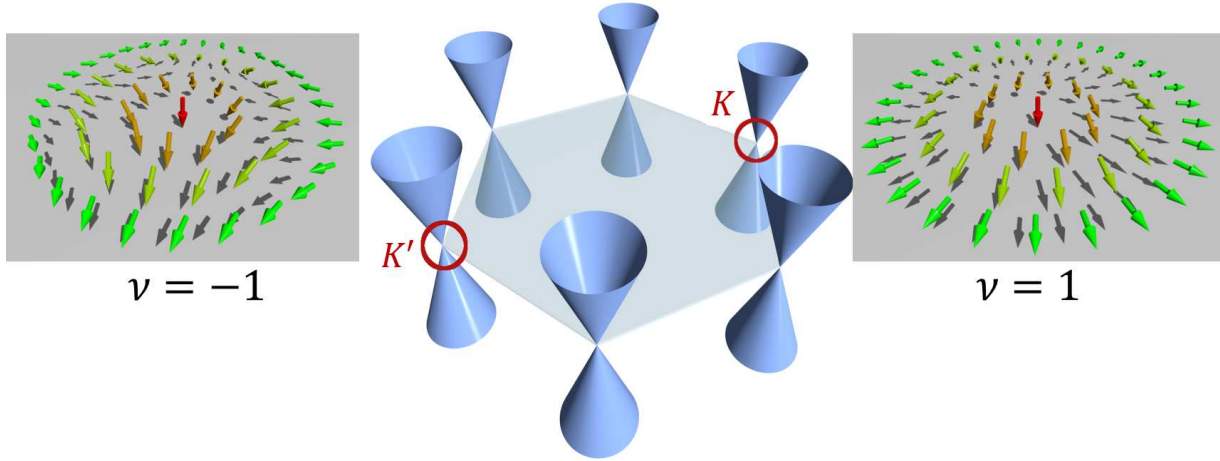


Figure 1.4: Dirac cones at the corners of Brillouin zone K and K' when $\phi = 0$. Inset: merons with a topological charge $\pm \frac{1}{2}$ at the K and K' points. $\nu = \pm 1$ are for the K and K' points respectively.

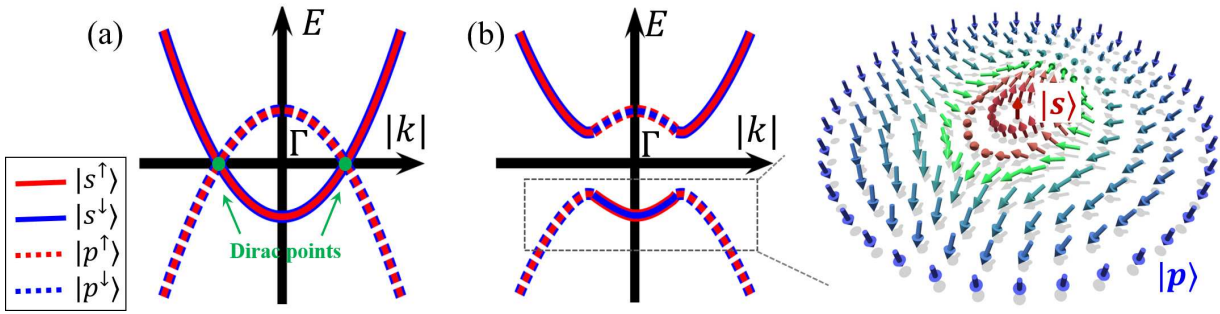


Figure 1.5: Energy dispersions of the Hamiltonian (1.16) with (a) $\alpha = 0$ and (b) $\alpha \neq 0$ around the Γ point. Two green dots in (a) are Dirac points. Red and blue curves denote spin-up and -down channels respectively, and solid and dashed curves represent $|s\rangle$ and $|p\rangle$ orbitals respectively. Right panel shows a Skyrmion structure for the valance band of either spin, where up(down) arrow is for $|s\rangle(|p\rangle)$.

$$\begin{aligned}\varepsilon(\mathbf{k}) &= E - 2F(2 - \cos k_x - \cos k_y), \\ d_x + i d_y &= A(\sin k_x + i \sin k_y), \\ d_z &= -2B[2 - (M/2B) - \cos k_x - \cos k_y].\end{aligned}$$

The $\varepsilon(\mathbf{k})$ term in the Hamiltonian (1.16) simply shifts whole dispersion relations by constants without contributing anything to the topology, and thus can be dropped in the following discussions of topology. For $A = 0$, the dispersion relation of the $|s\rangle$ and $|p\rangle$ in $H(\mathbf{k})$ are parabolic curves and can cross each other without opening a gap. By the Taylor's expansions, one can easily conclude that the dispersion relations are dominated by the first order of \mathbf{k} where the $|s\rangle$ and the $|p\rangle$ meet, i.e., we have Dirac cones there [see green dots in figure 1.5(a)]. The two Dirac cones are linked by the spatial inversion symmetry within the same spin channel. When the coupling term $A \neq 0$, a global band gap is opened at the two Dirac points. For spin-up channel, each of them contributes $1/2$ to the Chern number and totally we have $C_1 = 1$. Because of the time-reversal symmetry, the spin-down channel must have a Chern number with

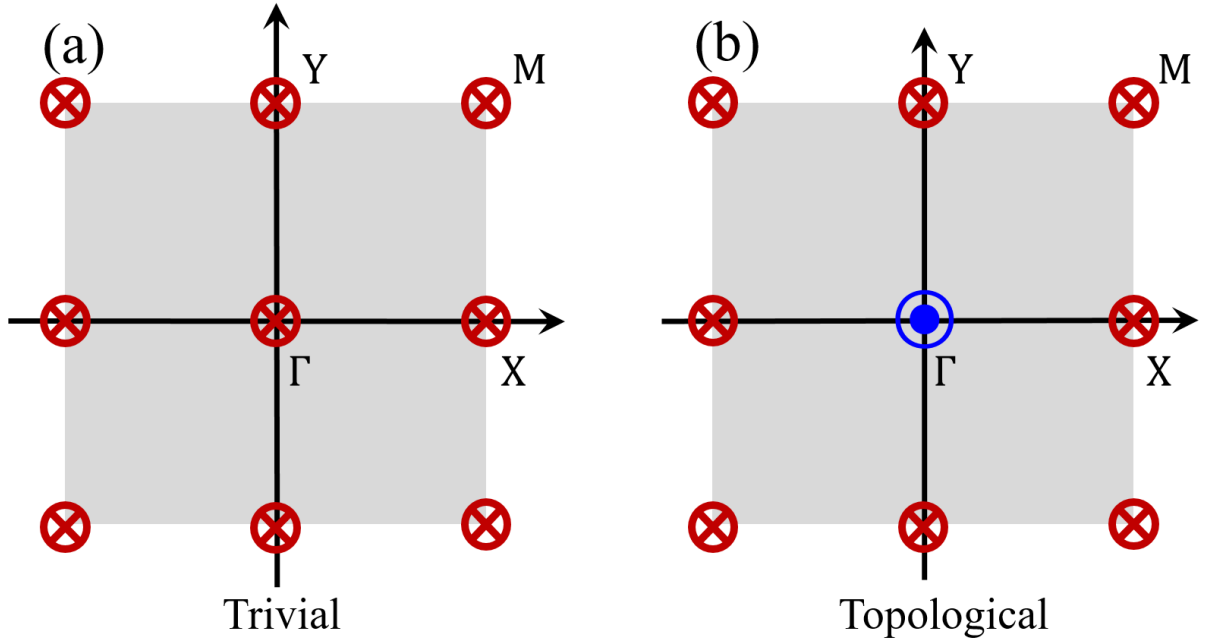


Figure 1.6: Schematic distributions of parity eigenvalues for (a) a trivial insulator with \mathbb{Z}_2 index $\zeta = 0$ and (b) a topological insulator with \mathbb{Z}_2 index $\zeta = 1$. \odot and \otimes symbols are for eigenvalues ± 1 of inversion operator \mathcal{P} , respectively.

opposite sign $C_{\downarrow} = -1$, which gives a spin Chern number

$$C_s = (C_{\uparrow} - C_{\downarrow})/2 = 1, \quad (1.17)$$

equivalent to a nonzero \mathbb{Z}_2 topological invariant $\zeta = 1$.

There is a simple way of identifying the nontrivial \mathbb{Z}_2 topology in a system with inversion symmetry [38]. For a Hamiltonian that commutes with spatial inversion operator \mathcal{P} , we have

$$(-1)^{\zeta} = \prod_i \delta_i \quad (1.18)$$

where ζ is the \mathbb{Z}_2 invariant, $\delta_i = \prod_{n=1}^N \xi_{2n}(\Gamma_i)$ with $\xi_{2n}(\Gamma_i) = \pm 1$ the eigenvalues of the operator \mathcal{P} for all $2n$ occupied bands at the time reversal invariant \mathbf{k} points Γ_i which satisfies $\mathcal{P}\mathbf{k} = \mathbf{k}$, such as $\Gamma = (0, 0)$, $X = (\pi, 0)$, $Y = (0, \pi)$, $M = (\pi, \pi)$ in a square lattice with unit lattice constants. As shown in figure 1.6(a), in the case that all eigenvalues of the inversion operator \mathcal{P} are -1 at the four time-reversal invariant points: Γ , X , Y and M , the system has a \mathbb{Z}_2 invariant $\zeta = 0$, corresponding to a trivial state. The trivial topology can also be observed in figure 1.6(a), the distribution of eigenvalues of \mathcal{P} exhibits a trivial “ferromagnetic” order. When a band inversion between $|s\rangle$ and $|p\rangle$ orbitals happens at the Γ point in the BHZ model, the eigenvalue of \mathcal{P} at the Γ point becomes $+1$ since the topmost valance band is now occupied by the s orbital [see figure 1.5(b)]. It can be easily seen that the “anti-ferromagnetic” distribution of eigenvalues of \mathcal{P} is in contrast with the trivial “ferromagnetic” order displayed in figure 1.6(a). This theory can be easily generalized into 3D systems with the only difference

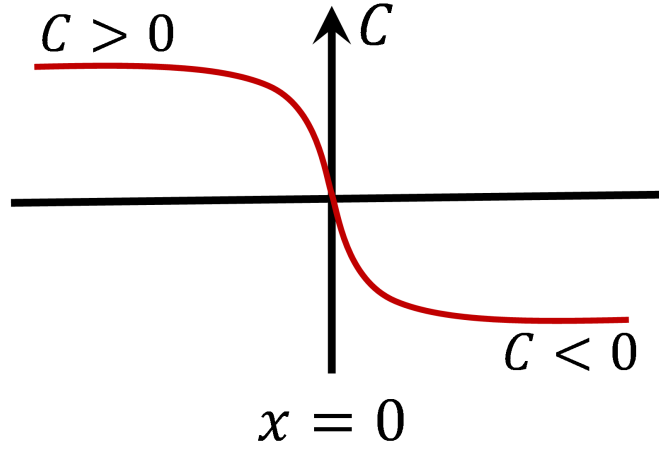


Figure 1.7: An interface at $x = 0$ with opposite Dirac mass terms C at two sides.

that there are eight time-reversal invariant points: four for $k_z = 0$ and another four for $k_z = \pi$ [38]. Many 3D topological insulators with inversion symmetry, such as $\text{Bi}_{1-x}\text{Sb}_x$ and its family members [39, 40], can be classified by using Eq. (1.18).

1.4 Edge states at a phase transition point

Let us consider the 2×2 Dirac Hamiltonian Eq. (1.12) and reduce it into one-dimensional by taking $k_y = 0$, which gives

$$\mathcal{H} = \begin{pmatrix} C(x) & k_x \\ k_x & -C(x) \end{pmatrix} \quad (1.19)$$

with $C(x) > 0$ for $x < 0$ and $C(x) < 0$ for $x > 0$, as shown in figure 1.7.

For an interface with opposite mass terms at two sides of $x = 0$ (see figure 1.7), we solve the above Hamiltonian by letting $k_x = -i\hbar\partial_x$. For simplicity, we only search for eigenstates $\psi(x) = [\psi_1(x), \psi_2(x)]^T$ at zero energy. The above Hamiltonian then can be written as

$$\partial_x \psi(x) = -\frac{C(x)}{\hbar} \sigma_y \psi(x). \quad (1.20)$$

By rotating wavefunctions $\tilde{\psi}(x) = U\psi$ for simplicity of later calculations with

$$U = \frac{1}{\sqrt{2}} \begin{pmatrix} i & -i \\ 1 & 1 \end{pmatrix},$$

we arrive at a new ordinary differential equation

$$\partial_x \tilde{\psi}(x) = \frac{C(x)}{\hbar} \sigma_z \tilde{\psi}(x), \quad (1.21)$$

which can be solved easily

$$\tilde{\psi}_{\pm}(x) = \exp\left[\pm \hbar \int_{x=0}^x dt C(t)\right] \begin{pmatrix} 1 \\ -1 \end{pmatrix}. \quad (1.22)$$

It is easy to see that $\int_0^x dt C(t) < 0$ when $x > 0$, the $\tilde{\psi}_{-}(x)$ must be the solution for the system since it is normalizable while $\tilde{\psi}_{+}(x)$ cannot. Similarly, $\tilde{\psi}_{+}$ is the solution when $x < 0$. Due to nature of exponential decaying for both $\tilde{\psi}_{\pm}$, we have a localized edge state at the interface $x = 0$ [41], which is the reason for the appearance of topological edge states at the interface of topological and trivial materials.

A \mathbb{Z}_2 Topological Phase in an All-Dielectric Photonic Crystal

2.1 Maxwell equations

Dynamics of electromagnetic (EM) field in sourceless systems are governed by the following Maxwell equations [42]

$$\vec{\nabla} \cdot \mathbf{H}(\mathbf{r}, t) = 0, \quad (2.1a)$$

$$\vec{\nabla} \cdot [\varepsilon(\mathbf{r})\mathbf{E}(\mathbf{r}, t)] = 0, \quad (2.1b)$$

$$\vec{\nabla} \times \mathbf{E}(\mathbf{r}, t) + \mu_0 \frac{\partial \mathbf{H}(\mathbf{r}, t)}{\partial t} = 0, \quad (2.1c)$$

$$\vec{\nabla} \times \mathbf{H}(\mathbf{r}, t) - \varepsilon_0 \varepsilon(\mathbf{r}) \frac{\partial \mathbf{E}(\mathbf{r}, t)}{\partial t} = 0, \quad (2.1d)$$

where $\mathbf{H}(\mathbf{r}, t)$ and $\mathbf{E}(\mathbf{r}, t)$ are magnetizing and electric fields that depend on space \mathbf{r} and time t , $\varepsilon(\mathbf{r})$ and $\mu(\mathbf{r})$ are position-dependent relative permittivity and permeability in the units of ε_0 and μ_0 for the vacuum respectively, and $\mathbf{B}(\mathbf{r}, t) = \mu_0 \mu(\mathbf{r}) \mathbf{H}(\mathbf{r}, t)$. Assuming periodicities of the $\mathbf{H}(\mathbf{r}, t)$ and $\mathbf{E}(\mathbf{r}, t)$ in time, we expand the two fields by the plane waves

$$\mathbf{H}(\mathbf{r}, t) = \sum_{\omega} \mathbf{H}(\mathbf{r}) e^{-i\omega t}, \quad \mathbf{E}(\mathbf{r}, t) = \sum_{\omega} \mathbf{E}(\mathbf{r}) e^{-i\omega t}, \quad (2.2)$$

where ω is the frequency of the plane wave. Substituting Eqs. (2.2) into Eqs. (2.1c) and (2.1d), we obtain

$$\vec{\nabla} \times \mathbf{E}(\mathbf{r}) - i\omega \mu_0 \mathbf{H}(\mathbf{r}) = 0, \quad (2.3a)$$

$$\vec{\nabla} \times \mathbf{H}(\mathbf{r}) + i\omega \varepsilon_0 \varepsilon(\mathbf{r}) \mathbf{E}(\mathbf{r}) = 0, \quad (2.3b)$$

or in the matrix form

$$i \begin{bmatrix} 0 & \vec{\nabla} \times \\ -\vec{\nabla} \times & 0 \end{bmatrix} \begin{bmatrix} \mathbf{E}(\mathbf{r}) \\ \mathbf{H}(\mathbf{r}) \end{bmatrix} = \omega \begin{bmatrix} \varepsilon(\mathbf{r})\varepsilon_0 & 0 \\ 0 & \mu_0 \end{bmatrix} \begin{bmatrix} \mathbf{E}(\mathbf{r}) \\ \mathbf{H}(\mathbf{r}) \end{bmatrix}, \quad (2.4)$$

which is a generalized eigenvalue problem.

Taking $\vec{\nabla}$ at both sides of Eq. (2.3a) and summing the two Eqs. (2.3a) and (2.3b) together, we arrive at the master equation for a harmonic electric field

$$\vec{\nabla} \times \vec{\nabla} \times \mathbf{E}(\mathbf{r}) = \left(\frac{\omega}{c}\right)^2 \varepsilon(\mathbf{r}) \mathbf{E}(\mathbf{r}) \quad (2.5)$$

with $1/c^2 = \varepsilon_0 \mu_0$, which is the core equation we will solve in this chapter.

For a photonic crystal with discrete translational symmetry, the eigen-functions of Eq. (2.5) satisfies the Bloch's theorem and can be decomposed into a product of a free-space plane wave and a spatially periodic function, i.e.

$$\mathbf{E}(\mathbf{r}) = \exp(i\mathbf{k} \cdot \mathbf{r}) u_{\mathbf{k}}(\mathbf{r}), \quad (2.6)$$

where $u_{\mathbf{k}}(\mathbf{r})$ is a periodic function in space, modulating the plane wave $\exp(i\mathbf{k} \cdot \mathbf{r})$ in a free space. Substituting Eq. (2.6) into Eq. (2.5), we arrive at

$$\begin{aligned} \vec{\nabla} \times \vec{\nabla} \times \exp(i\mathbf{k} \cdot \mathbf{r}) u_{\mathbf{k}}(\mathbf{r}) &= \left(\frac{\omega}{c}\right)^2 \varepsilon(\mathbf{r}) \exp(i\mathbf{k} \cdot \mathbf{r}) u_{\mathbf{k}}(\mathbf{r}), \\ \vec{\nabla} \times \exp(i\mathbf{k} \cdot \mathbf{r}) [(i\mathbf{k} + \vec{\nabla}) \times u_{\mathbf{k}}(\mathbf{r})] &= \left(\frac{\omega}{c}\right)^2 \varepsilon(\mathbf{r}) \exp(i\mathbf{k} \cdot \mathbf{r}) u_{\mathbf{k}}(\mathbf{r}), \\ (i\mathbf{k} + \vec{\nabla}) \times (i\mathbf{k} + \vec{\nabla}) \times u_{\mathbf{k}}(\mathbf{r}) &= \left(\frac{\omega}{c}\right)^2 \varepsilon(\mathbf{r}) u_{\mathbf{k}}(\mathbf{r}). \end{aligned} \quad (2.7)$$

By taking complex conjugate of both sides of Eq. (2.7), we have

$$[i(-\mathbf{k}) + \vec{\nabla}] \times [i(-\mathbf{k}) + \vec{\nabla}] \times u_{\mathbf{k}}^*(\mathbf{r}) = \left(\frac{\omega}{c}\right)^2 \varepsilon(\mathbf{r}) u_{\mathbf{k}}^*(\mathbf{r}). \quad (2.8)$$

Comparing the two Eqs. (2.7) and (2.8), it is easy to see that

$$u_{-\mathbf{k}}(\mathbf{r}) = u_{\mathbf{k}}^*(\mathbf{r}) \quad (2.9)$$

with a same eigenfrequency ω . In fact, this is a consequence of the time-reversal symmetry obeyed by the conventional Maxwell equations [42].

2.2 Dirac cones and topology in photonic crystals

Dirac electron is a massless relativistic particle that was considered to only exist in high-energy physics. It was first theoretically studied that honeycomb lattice can be a natural platform for supporting Dirac electrons [43]. The first hallmark material for realizing the massless fermion is the monolayer graphene with massless π electrons [44–46].

It has been revealed that Dirac cones can also be in the Brillouin zone center due to accidental degeneracy [47, 48]. A rule for searching Dirac cones in a system preserving inversion symmetry \mathcal{P} is checking whether there is a band crossing between two optical bands of opposite spatial parities. At the crossing points, Dirac cones generally exist. To prove this, we simply consider the first order perturbation term in a 2D system

$$\mathcal{H}'_{\mathbf{k}} = \mathbf{k} \cdot \mathbf{P}, \quad (2.10)$$

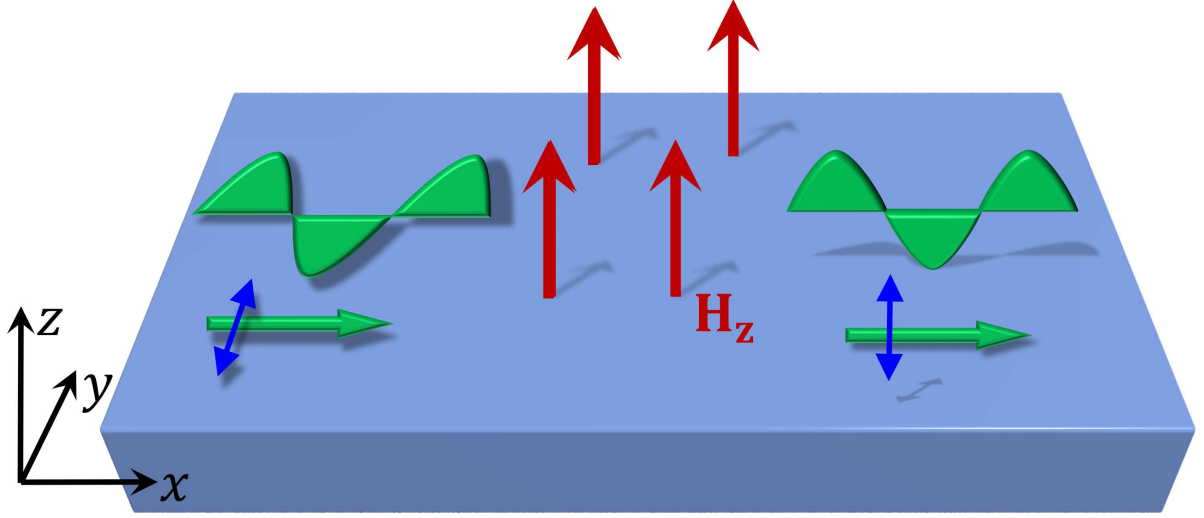


Figure 2.1: Materials with magneto-optic effects under a perpendicular external magnetic field H_z . The polarization direction of the in-plane electric wave is rotated to out-of-plane by the Faraday effect, breaking the time-reversal symmetry.

where \mathbf{P} is the momentum operator. For simplicity, we assume that u_1 and u_2 are two eigenstates of the full Hamiltonian with even spatial parity at the inversion-invariant points: $\mathcal{P} u_{1(2)} = u_{1(2)}$. Since the system respecting inversion symmetry \mathcal{P} , $\mathcal{H}'_{\mathbf{k}}$ must be invariant under \mathcal{P} , which gives

$$\langle u_1 | \mathbf{P} | u_2 \rangle = \langle u_1 | \mathcal{P}^\dagger \mathcal{P} \mathbf{P} \mathcal{P}^\dagger | u_2 \rangle = -\langle u_1 | \mathcal{P}^\dagger \mathbf{P} \mathcal{P} | u_2 \rangle = -\langle u_1 | \mathbf{P} | u_2 \rangle \quad (2.11)$$

indicating $\langle u_1 | \mathbf{P} | u_2 \rangle = 0$, i.e., the linear order term of $\mathcal{H}'_{\mathbf{k}}$ vanishes. Similarly, we can prove that the first-order coupling term between u_1 and u_2 of odd parity also vanishes. It is easy to conclude that a nonzero first-order term of \mathbf{k} only appears when the u_1 and u_2 of opposite parities touch each other in energy/frequency. Systematic studies of Dirac cones in the Brillouin center for systems with various crystal symmetries are given by Sakoda [14, 15, 49, 50].

Developments of topological theories in photonic crystals were initiated by Haldane [12], where the author started from a hexagonal lattice of 2D nanorods and demonstrated the existence of optical Dirac cones at the $K(K')$ points the corner of the Brillouin zone. The appearance of Dirac cones is guaranteed by the threefold rotation symmetry. It has been proven by the author that a topological band gap is opened at the Dirac points by introducing the Faraday effect, also known as the magneto-optic effect, which manifests itself with an imaginary off-diagonal magnetic permeability

$$\mu = \begin{pmatrix} \mu_{xx} & i\mu_{xy} & 0 \\ -i\mu_{xy} & \mu_{yy} & 0 \\ 0 & 0 & \mu_{zz} \end{pmatrix}. \quad (2.12)$$

The nonzero μ_{xy} is responsible for rotating polarization axis in the plane perpendicular to the propagation direction, as shown in figure 2.1.

Similar to the QAHE in an electronic system discussed in Section 1.3.1, time-reversal symmetry needs to be broken to realize a Chern insulator. In the photonic system with magneto-optic effect, the time-reversal symmetry is naturally broken by the nonzero μ_{xy} in Eq. (2.12) in the sense that the chirality of the polarization axis rotation is predetermined by the sign of μ_{xy} . The photonic band gap opened at the Dirac point by breaking the time-reversal symmetry is topologically nontrivial characterized by Chern numbers [6, 12]. This topological state is also known as optical QHE. Later, experimental confirmations of the one-way edge state were clearly demonstrated [28].

As in the solid state physics, the Kramers doublet is essential for realizing quantum spin Hall effect [9, 11], which is missing in a conventional photonic system with $\mathcal{T}^2 = 1$, where $\mathcal{T} = \mathcal{K}$ is the time-reversal symmetry respected by Maxwell equations. Several proposals for creating pseudo-Kramers doublets were suggested, such as the clockwise and anti-clockwise circulations of light in a coupled resonator optical waveguides [31, 32] and the bonding/antibonding electric and magnetic fields in a hexagonal lattice of metamaterials [33, 51].

2.3 Topological photonics characterized by \mathbb{Z}_2 invariant

2.3.1 Two-dimensional photonic crystals

In this section, we focus on two-dimensional (2D) photonic crystals by assuming they are infinitely long along the z axis, as shown in figure 2.2. Since

$$\begin{aligned}\sigma_z H_{x,y} &= -H_{x,y}, & \sigma_z E_z &= -E_z, \\ \sigma_z E_{x,y} &= E_{x,y}, & \sigma_z H_z &= H_z\end{aligned}$$

with σ_z the mirror operator against x - y plane, we divide EM wavefunctions by eigenvalues into the transverse magnetic (TM) mode with nonzero $\{H_x, H_y, E_z\}$ and the transverse electric (TE) mode with nonzero $\{E_x, E_y, H_z\}$, where E_i/H_i ($i = x, y, z$) are components of electric/magnetizing field along i axis.

Let us consider the TM mode, for which equation (2.5) is reduced to

$$\vec{\nabla}^2 E_z(\mathbf{r}) \hat{z} = \left(\frac{\omega}{c}\right)^2 \varepsilon(\mathbf{r}) E_z(\mathbf{r}) \hat{z} \quad (2.13)$$

with operator $\vec{\nabla}^2 = -\partial_x^2 - \partial_y^2 = k_x^2 + k_y^2 = \mathbf{k}^2$, where $k_{x(y)} = -i\partial_{x(y)}$. For homogeneous materials [$\varepsilon(\mathbf{r})$ is constant], it is easy to see that the eigenfrequency is a linear function of \mathbf{k} ($\omega \propto \mathbf{k}$), indicating appearance of Dirac dispersion relation [52]. In the case of non-homogeneous materials with position-dependent $\varepsilon(\mathbf{r})$, Dirac dispersions are removed by photonic band gaps due to Bragg scatterings of Bloch waves [49, 53], resembling electronic band gap in semiconductors or insulators [54]. However, Dirac cones can emerge again whenever two bands of opposite spatial parities touch at high-symmetric \mathbf{k} points under various crystal symmetries [14, 15, 47–49].

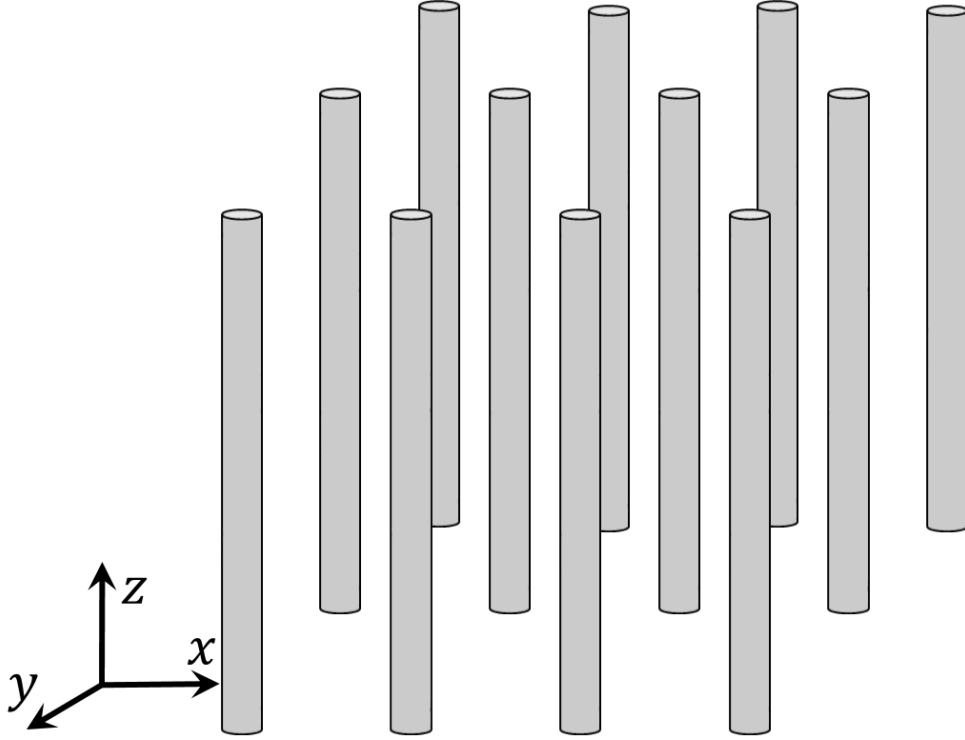


Figure 2.2: Two-dimensional photonic crystal consists of dielectric rods infinite long along the z axis.

2.3.2 Time-reversal symmetry of Maxwell equations

The Laplacian operator $\vec{\nabla}^2$ is real symmetric, which is invariant under a complex conjugate operator \mathcal{K} . We have

$$\begin{aligned} [\vec{\nabla}^2 E_z(\mathbf{r})\hat{z}]^* &= \left(\frac{\omega}{c}\right)^2 \varepsilon(\mathbf{r}) E_z^*(\mathbf{r})\hat{z}, \\ \vec{\nabla}^2 E_z^*(\mathbf{r})\hat{z} &= \left(\frac{\omega}{c}\right)^2 \varepsilon(\mathbf{r}) E_z^*(\mathbf{r})\hat{z} \end{aligned} \quad (2.14)$$

for a photonic crystal with real $\varepsilon(\mathbf{r})$. The above eigen-problem indicates that $E_z^*(\mathbf{r}) = \mathcal{K} E_z(\mathbf{r})$ is also an eigensolution of Maxwell equation if $E_z(\mathbf{r})$ satisfies Eq. (2.13), i.e., the conventional time-reversal operator for Maxwell equations is $\mathcal{T}_p = \mathcal{K}$.

As we have shown in Eq. (2.9), the eigenfrequency for $E_z(\mathbf{r})$ and $E_z^*(\mathbf{r})$ are $\omega(\mathbf{k}) = \omega(-\mathbf{k})$ respectively. The $\omega(\mathbf{k})$ and $\omega(-\mathbf{k})$ around time-reversal-invariant points is

$$\omega(\mathbf{k}) = \omega_0 + \mathbf{k}\omega' + \frac{\mathbf{k}^2}{2}\omega'' + \dots, \quad (2.15)$$

$$\omega(-\mathbf{k}) = \omega_0 - \mathbf{k}\omega' + \frac{\mathbf{k}^2}{2}\omega'' + \dots, \quad (2.16)$$

resulting in $\omega' = 0$. Therefore, the dispersion for a single band around time-reversal-invariant points must be parabolic with $\omega(\mathbf{k}) = \omega_0 + \frac{\mathbf{k}^2}{2}\omega'' + \dots$.

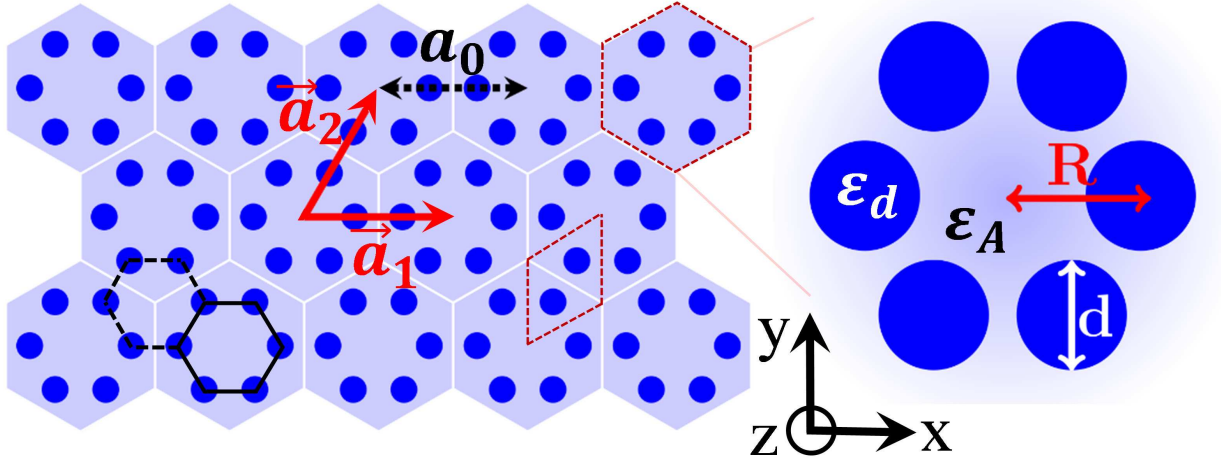


Figure 2.3: Schematic plot of a triangular photonic crystal of “artificial atoms” composed by six cylinders of dielectric material. Red dashed rhombus and hexagon are primitive cells of honeycomb and triangular lattices. Solid black hexagon labels an artificial atom, while dashed black one marks the interstitial region among artificial atoms. \vec{a}_1 and \vec{a}_2 are unit vectors with length a_0 as the lattice constant. Right panel: enlarged view of hexagonal cluster with R the length of hexagon edge and d the diameter of cylinders. ϵ_d and ϵ_A are dielectric constants of cylinders and surrounding environment.

2.3.3 Pseudo-time-reversal symmetry

Haldane demonstrated that photonic crystals can also support Dirac cones in a 2D honeycomb lattice when the time-reversal symmetry is preserved [12]. Introducing magneto-optic effect (Faraday effect) that breaks the time-reversal symmetry, the system is driven into a topological state characterized by Chern numbers [4].

Let us consider harmonic TM modes of EM wave, namely those of finite out-of-plane E_z and in-plane H_x and H_y components with others being zero in a dielectric medium (see figure 2.3). For simplicity, the real electric permittivities of both cylinders (ϵ_d) and environment (ϵ_A) are taken frequency independent in the regime under consideration. The master equation for a harmonic mode of frequency ω is then derived from the Maxwell equations [42]

$$\left[\frac{1}{\epsilon(\mathbf{r})} \vec{\nabla} \times \vec{\nabla} \times \right] E_z(\mathbf{r}) \hat{z} = \frac{\omega^2}{c^2} E_z(\mathbf{r}) \hat{z}, \quad (2.17)$$

with $\epsilon(\mathbf{r})$ the position-dependent permittivity and c the speed of light. The magnetic field are given by the Faraday relation $\mathbf{H} = [-i/(\mu_0\omega)] \vec{\nabla} \times \mathbf{E}$, where the magnetic permeability μ_0 is presumed as that of vacuum. The Bloch theorem applies for the present system when $\epsilon(\mathbf{r})$ is periodic as shown in figure 2.3. It is reminded however that the master equation (2.17) describes the EM waves instead of electrons carrying on the spin degree of freedom, with the most prominent difference lying at the response upon time-reversal operation. For simplicity, we consider first a system infinite in z direction which reduces the problem to 2D.

We start from a honeycomb lattice of dielectric cylinders, and deform it in the way keeping hexagonal clusters composed by six neighboring cylinders and the C_6 symmetry. Now the alignment of dielectric cylinders is more convenient to be considered a triangular lattice of hexagonal “artificial atoms”.

There are two irreducible representations in the C_6 symmetry group associated with the triangular lattice: E' and E'' with basis functions x/y and $xy/(x^2-y^2)$, corresponding to odd and even spatial parities respectively [55]. As can be seen in figure 2.4(a) for E_z field at Γ point, artificial atoms carry p_x/p_y and $d_{xy}/d_{x^2-y^2}$ orbitals, with the same symmetry as those of electronic orbitals of conventional atoms in solids.

We now examine matrix representations of $\pi/3$ rotation and its combinations for the basis functions of p_x/p_y and $d_{xy}/d_{x^2-y^2}$. Since p_x/p_y behave in the same way as x/y , it is easy to see

$$D_{E'}(C_6) \begin{pmatrix} p_x \\ p_y \end{pmatrix} = \begin{pmatrix} \frac{1}{2} & -\frac{\sqrt{3}}{2} \\ \frac{\sqrt{3}}{2} & \frac{1}{2} \end{pmatrix} \begin{pmatrix} p_x \\ p_y \end{pmatrix}. \quad (2.18)$$

It is noticed that $\mathcal{U} = [D_{E'}(C_6) + D_{E'}(C_6^2)]/\sqrt{3} = -i\sigma_y$ with $D_{E'}(C_6^2) \equiv D_{E'}^2(C_6)$ is associated with the $\pi/2$ rotation of p_x/p_y (σ_y being the Pauli matrix). Therefore, $\mathcal{U}^2(p_x, p_y)^T = -(p_x, p_y)^T$, which is consistent with the odd parity of p_x/p_y with respect to spatial inversion. Similarly, one has

$$D_{E''}(C_6) \begin{pmatrix} d_{x^2-y^2} \\ d_{xy} \end{pmatrix} = \begin{pmatrix} -\frac{1}{2} & -\frac{\sqrt{3}}{2} \\ \frac{\sqrt{3}}{2} & -\frac{1}{2} \end{pmatrix} \begin{pmatrix} d_{x^2-y^2} \\ d_{xy} \end{pmatrix}, \quad (2.19)$$

which is same as $D_{E'}(C_6^2)$ because the basis functions are now bilinear of x/y . It is then straightforward to check that $[D_{E''}(C_6) - D_{E''}(C_6^2)]/\sqrt{3} = \mathcal{U}$ is associated with a $\pi/4$ rotation of $d_{xy}/d_{x^2-y^2}$, which yields $\mathcal{U}^2(d_{x^2-y^2}, d_{xy})^T = -(d_{x^2-y^2}, d_{xy})^T$.

We compose the anti-unitary operator $\mathcal{T} = \mathcal{U}\mathcal{K}$ where \mathcal{K} is the complex conjugate operator associated with the TR operation respected by Maxwell systems in general. Since $\mathcal{T}^2 = -1$ is guaranteed by $\mathcal{U}^2 = -1$, \mathcal{T} can be taken as a pseudo-TR operator which provides Kramers doubling in the same way as the TR symmetry in electronic systems. It is clear that the crystal symmetry plays an important role in this pseudo-TR symmetry [56].

In order to derive the pseudo TR operator $\mathcal{T}' = U'\mathcal{K}$ on basis $[p_+, p_-]$ with $p_{\pm} = (p_x \pm ip_y)/\sqrt{2}$, we need to transform the \mathcal{U} operator to

$$\mathcal{U}' = V^\dagger \mathcal{U} V = \begin{pmatrix} i & 0 \\ 0 & -i \end{pmatrix}, \quad (2.20)$$

with

$$V = \begin{pmatrix} 1/\sqrt{2} & 1/\sqrt{2} \\ -i/\sqrt{2} & i/\sqrt{2} \end{pmatrix}$$

the transformation matrix between the basis wave functions. It is straightforward to see

$$\begin{aligned} \mathcal{T}' p_{\pm} &= \mathcal{U}' \mathcal{K} p_{\pm} = \mathcal{U}' p_{\mp} = \mp i p_{\mp}, \\ \mathcal{T}'^2 p_{\pm} &= \mathcal{T}'(\mp i p_{\mp}) = \pm i \mathcal{U}' p_{\pm} = -p_{\pm}, \end{aligned} \quad (2.21)$$

which gives $\mathcal{T}'^2 = -1$ in the irreducible representation E' . Similarly, one can show $\mathcal{T}'^2 = -1$ in irreducible representation E'' . From Eq. (2.21), it is clear that the wave functions for E_z field of positive and negative angular momenta are two pseudo spins of our photonic system since \mathcal{T}' transforms the pseudo spin-up state to the spin-down state, and vice versa.

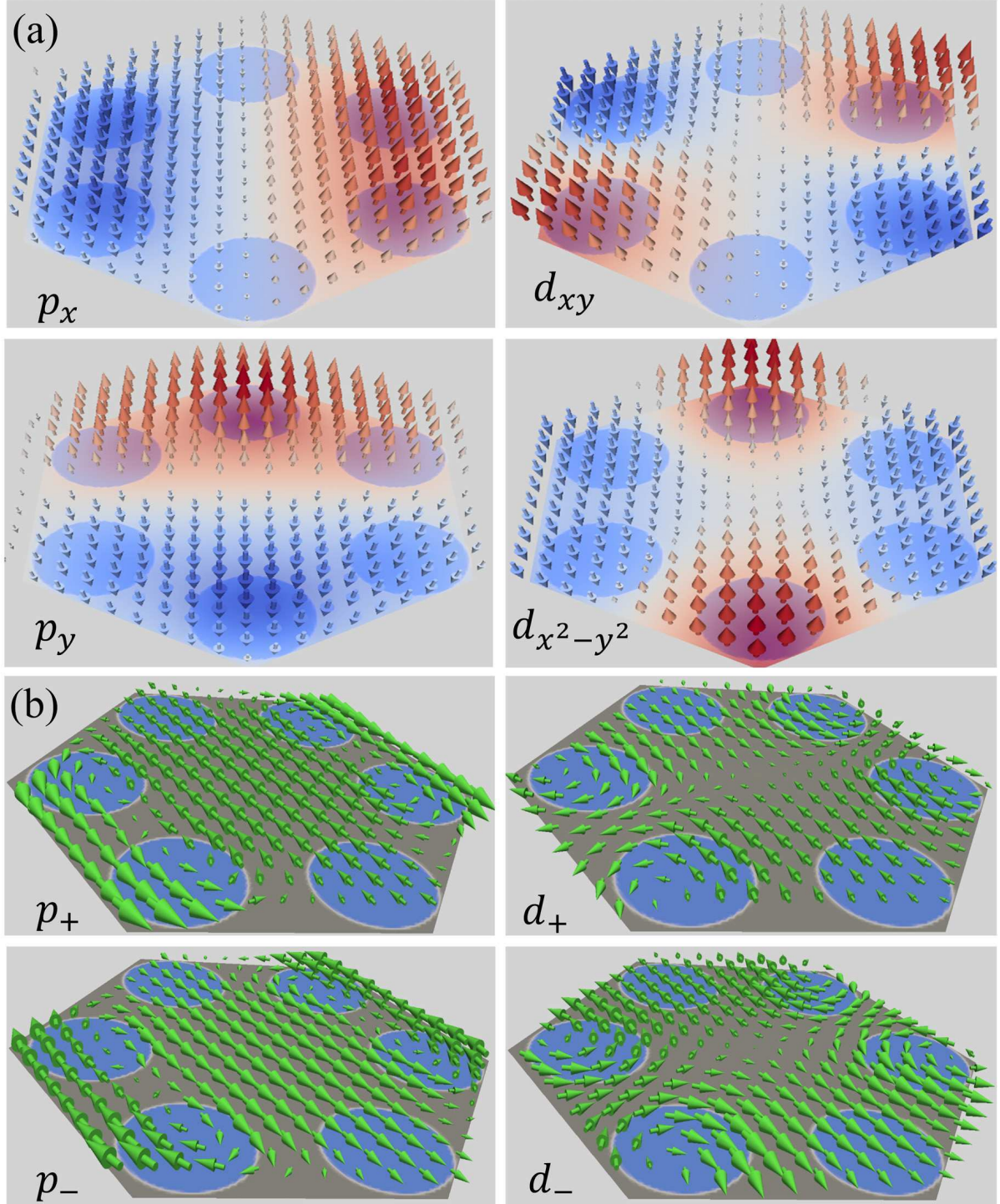


Figure 2.4: (a) Electric fields E_z of the p_x/p_y and $d_{xy}/d_{x^2-y^2}$ photonic orbitals hosted by the artificial atom at Γ point. (b) Magnetic fields associated with E_z fields with wave functions of positive and negative angular momenta $p_{\pm} = (p_x \pm i p_y)/\sqrt{2}$ and $d_{\pm} = (d_{x^2-y^2} \pm i d_{xy})/\sqrt{2}$. The angular momentum of wave function of E_z field constitutes the pseudo spin in the present photonic crystal.

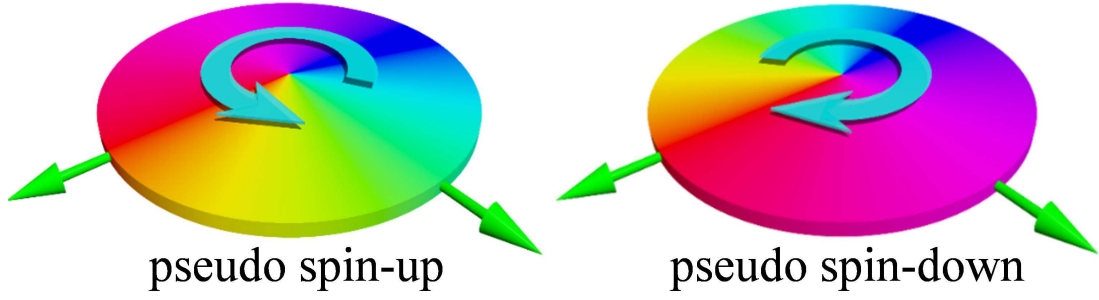


Figure 2.5: Berry curvatures around Γ point for pseudo spin-up and -down channels when the band inversion of p and d orbitals happens at Γ point.

2.3.4 Pseudospins: orbital angular momentum of electric fields

For the harmonic transverse magnetic (TM) mode, the in-plane magnetic fields associated with the E_z fields $p_x(\mathbf{r})$ and $p_y(\mathbf{r})$ are given by the Faraday relation

$$\mathbf{H}_1 = \frac{-i}{\mu_0 \omega} \vec{\nabla} \times (p_x \hat{z}), \quad \mathbf{H}_2 = \frac{-i}{\mu_0 \omega} \vec{\nabla} \times (p_y \hat{z}), \quad (2.22)$$

where $\mathbf{H}_i = h_{ix} \hat{x} + h_{iy} \hat{y}$ ($i = 1, 2$) with \hat{x} and \hat{y} the in-plane unit vectors. Distributions of real parts of magnetic fields associated with p_{\pm} are shown in figure 2.4(b). Since the wave functions of E_z field $p_x(\mathbf{r})$ and $p_y(\mathbf{r})$ are linked to each other by $\pi/2$ rotation, one has at origin

$$\begin{pmatrix} h_{2x} \\ h_{2y} \end{pmatrix} = \begin{pmatrix} h_{1y} \\ -h_{1x} \end{pmatrix}. \quad (2.23)$$

It is then easy to see that the wave functions of E_z field with positive and negative angular momenta generate the magnetic fields

$$-\frac{i}{\mu_0 \omega} \vec{\nabla} \times [(p_x \pm i p_y) \hat{z}] = (h_{1x} \pm i h_{1y})(\hat{x} \mp i \hat{y}). \quad (2.24)$$

Because the harmonic mode evolves with time according to $\exp(i\omega t)$, the term $\mp i$ in front of \hat{y} in Eq. (2.24) corresponds to a $\mp \pi/2$ phase shift in x and y components of magnetic field, which is nothing but the circular polarization of magnetic field. Therefore, the circular polarization of in-plane magnetic field corresponds to the angular momentum of the wave function of out-of-plane electric field in the present photonic crystal, a property useful for stimulating electromagnetic waves with specific pseudospin (see figure 2.5).

2.4 Topological phase transitions

Now we calculate the photonic band dispersions described by the master equation (2.5) imposing periodic boundary conditions along unit vectors \vec{a}_1 and \vec{a}_2 given in figure 2.3. As shown in figure 2.6, double degeneracy in the band dispersions appears at Γ point, which can be identified as p_{\pm} and d_{\pm} states, consistent with the symmetry consideration. For large lattice constant a_0 , the photonic band

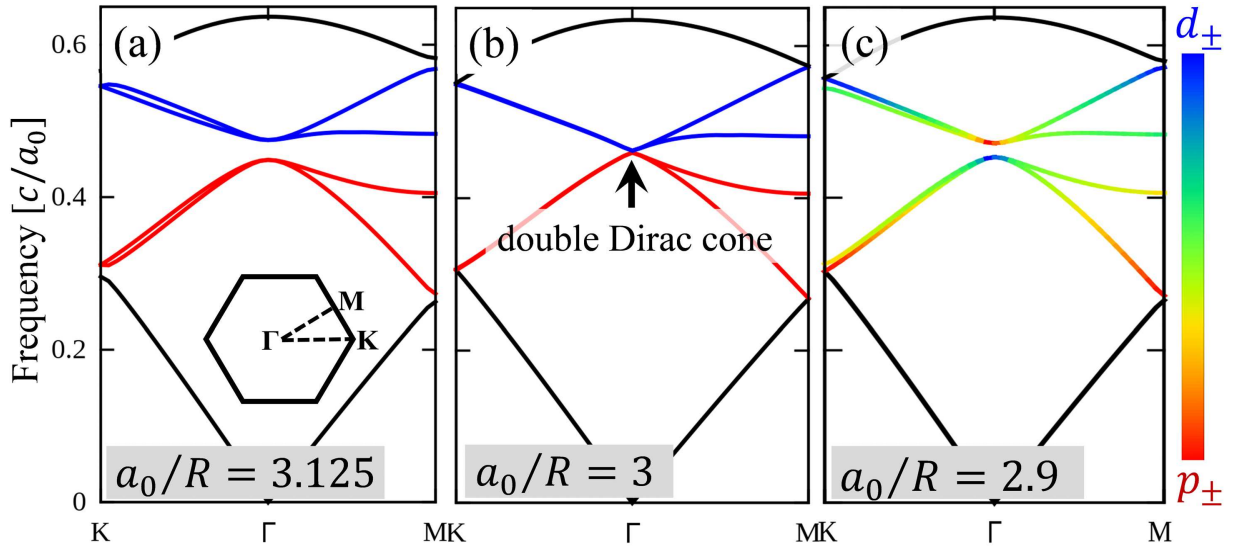


Figure 2.6: Dispersion relations of TM mode for the 2D photonic crystals with $\varepsilon_d = 11.7$, $\varepsilon_A = 1$ and $d = 2R/3$ for (a) $a_0/R = 3.125$ (Inset: Brillouin zone of triangular lattice), (b) $a_0/R = 3$ and (c) $a_0/R = 2.9$. Blue and red are for d_{\pm} and p_{\pm} bands respectively, and rainbow for hybridization between them. The case of $a_0/R = 3$ corresponds exactly to the honeycomb lattice of individual cylinders.

below (above) the gap is occupied by p_{\pm} (d_{\pm}) states (see figure 2.6(a) for $a_0/R = 3.125$ with R the length of hexagon edge).

Reducing the lattice constant to $a_0/R = 3$, the p and d states become degenerate at Γ point, and two Dirac cones appear as shown in figure 2.6(b). This is because that at this lattice constant the system is equivalent to honeycomb lattice of individual cylinders [see figure 2.7(a)]. It has been shown that the honeycomb lattice can support Dirac cones at the K and K' points [57]. By folding the Brillouin zone of honeycomb lattice of individual cylinders, we observe that the K and K' points in the Brillouin zone of honeycomb lattice are equivalent to the Γ point of the triangular lattice of hexagons, as shown in figure 2.7. Therefore, the doubly degenerate Dirac cones at the Γ point are nothing but those at the K and K' point in the Brillouin zone of honeycomb lattice based on the primitive rhombic unit cell of two sites.

When the lattice constant is further reduced, a global photonic band gap is reopened near the Dirac point as shown in figure 2.6(c) for $a_0/R = 2.9$. Now the E_z field at low-(high)-frequency side of the band gap exhibits d_{\pm} (p_{\pm}) characters around the Γ point, opposite to the order away from the Γ point. Namely a band inversion takes place upon reducing the lattice constant in the present system. Quantitatively, the band gap is $\Delta\omega = 5.47$ THz at $\omega = 138.77$ THz with $a_0 = 1 \mu\text{m}$, with all the quantities scaling with the lattice constant.

2.5 $\mathbf{k} \cdot \mathbf{P}$ model for topological photonic crystals

In this section we evaluate the \mathbb{Z}_2 invariant of the present photonic crystal based on $\mathbf{k} \cdot \mathbf{P}$ perturbation theory. We consider the photonic crystal with C_6 point group symmetry. We denote the eigenstates at Γ point as $\Gamma_1 = p_x \equiv |x\rangle$, $\Gamma_2 = p_y \equiv |y\rangle$, $\Gamma_3 = d_{x^2-y^2} \equiv |x^2 - y^2\rangle$ and $\Gamma_4 = d_{xy} \equiv |2xy\rangle$. The effective

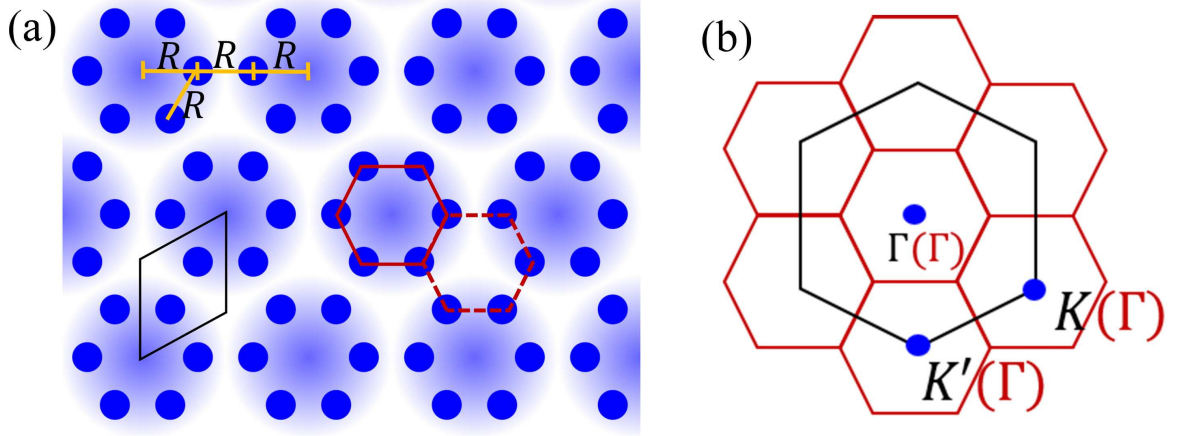


Figure 2.7: (a) Triangular lattice of hexagons with $a_0/R = 3$, which is equivalent to honeycomb lattice of individual dielectric rods. (b) K and K' points in the folded Brillouin zone for honeycomb lattice of individual cylinders overlap with the Γ point for triangular lattice of hexagons (shaded by blue). Blue dots are dielectric rods. Red hexagons and black rhomb are for unit cells of triangular and honeycomb lattices respectively.

$\mathbf{k} \cdot \mathbf{P}$ Hamiltonian is

$$\mathcal{H}(\mathbf{k}) = \mathcal{H}_0 + \mathcal{H}', \quad (2.25)$$

where

$$\mathcal{H}_0 = \begin{pmatrix} \epsilon_p^0 & & & \\ & \epsilon_p^0 & & \\ & & \epsilon_d^0 & \\ & & & \epsilon_d^0 \end{pmatrix} \quad (2.26)$$

is the Hamiltonian at Γ point on the basis $[\Gamma_1, \Gamma_2, \Gamma_3, \Gamma_4]$, with ϵ_p^0 and ϵ_d^0 eigenvalues of $\mathcal{H}(\mathbf{k} = 0)$, and \mathcal{H}' is the perturbation term. Away from Γ point, the diagonal entries become $\epsilon_\alpha(\mathbf{k}) = \epsilon_\alpha^0 + D_\alpha \mathbf{k}^2$ with $\alpha = d, p$.

The Hamiltonian \mathcal{H}' on the same basis in general is

$$\mathcal{H}' = \begin{pmatrix} \mathcal{H}_{pp} & \mathcal{H}_{pd} \\ \mathcal{H}_{pd}^\dagger & \mathcal{H}_{dd} \end{pmatrix}. \quad (2.27)$$

Matrix elements of \mathcal{H}_{pp} are given by [55]

$$\mathcal{H}_{pp}^{ij} = M_{ij} + \sum_{\alpha=3,4} \frac{M_{i\alpha} M_{\alpha j}}{E_i - E_\alpha}, \quad (2.28)$$

with $M_{\alpha\beta} = \langle \Gamma_\alpha | \mathbf{k} \cdot \mathbf{P} | \Gamma_\beta \rangle$ ($\alpha, \beta = 1, \dots, 4$), where the integration is taken over real space. Since Γ_1 and Γ_2 have the same parity, M_{ij} in equation (2.28) does not include linear order term of \mathbf{k} . When $i = j$, the

second term of equation (2.28) is

$$\begin{aligned}\mathcal{H}_{pp}^{11} &= \sum_{\alpha=3,4} \frac{\langle \Gamma_1 | k_x P_x + k_y P_y | \Gamma_\alpha \rangle \langle \Gamma_\alpha | k_x P_x + k_y P_y | \Gamma_1 \rangle}{E_1 - E_\alpha} \\ &= Gk_x^2 + Fk_y^2,\end{aligned}\quad (2.29)$$

where $F = |\langle x | P_y | 2xy \rangle|^2 / (E_1 - E_4)$, $G = |\langle x | P_x | x^2 - y^2 \rangle|^2 / (E_1 - E_3)$, $P_x = \partial / \partial x$ and $P_y = \partial / \partial y$. Similarly, we have

$$\mathcal{H}_{pp}^{22} = Fk_x^2 + Gk_y^2 \quad (2.30)$$

and

$$\mathcal{H}_{pp}^{12} = \mathcal{H}_{pp}^{21} = Nk_x k_y \quad (2.31)$$

with $N = F + G$. Therefore, the Hamiltonian \mathcal{H}_{pp} is summarized as

$$\mathcal{H}_{pp} = \begin{pmatrix} Gk_x^2 + Fk_y^2 & Nk_x k_y \\ Nk_x k_y & Fk_x^2 + Gk_y^2 \end{pmatrix}. \quad (2.32)$$

In the same way, we obtain

$$\mathcal{H}_{dd} = \begin{pmatrix} -Gk_x^2 - Fk_y^2 & -Nk_x k_y \\ -Nk_x k_y & -Fk_x^2 - Gk_y^2 \end{pmatrix}. \quad (2.33)$$

We now evaluate the off-diagonal term of \mathcal{H}' :

$$\begin{aligned}\mathcal{H}_{pd}^{13} &= \langle \Gamma_1 | k_x P_x + k_y P_y | \Gamma_3 \rangle \\ &= \langle x | P_x | x^2 - y^2 \rangle k_x = Ak_x,\end{aligned}\quad (2.34)$$

$$\mathcal{H}_{pd}^{14} = \langle x | P_y | 2xy \rangle k_y = Ak_y, \quad (2.35)$$

$$\mathcal{H}_{pd}^{23} = \langle y | P_y | x^2 - y^2 \rangle k_y = -Ak_y, \quad (2.36)$$

and

$$\mathcal{H}_{pd}^{24} = \langle y | P_x | 2xy \rangle k_x = Ak_x. \quad (2.37)$$

Therefore, the effective Hamiltonian $\mathcal{H}(\mathbf{k})$ is

$$\mathcal{H}(\mathbf{k}) = \begin{pmatrix} \epsilon_p + Gk_x^2 + Fk_y^2 & Nk_x k_y & Ak_x & Ak_y \\ Nk_x k_y & \epsilon_p + Fk_x^2 + Gk_y^2 & -Ak_y & Ak_x \\ A^* k_x & -A^* k_y & \epsilon_d - Gk_x^2 - Fk_y^2 & -Nk_x k_y \\ A^* k_y & A^* k_x & -Nk_x k_y & \epsilon_d - Fk_x^2 - Gk_y^2 \end{pmatrix}. \quad (2.38)$$

This is consistent with that obtained by tight-binding approximations [15]. Rewriting $\mathcal{H}(\mathbf{k})$ on the basis $[p_+, d_+, p_-, d_-]$, we have

$$\mathcal{H}'(\mathbf{k}) = \begin{pmatrix} H_+ & H_{+-} \\ H_{+-}^\dagger & H_- \end{pmatrix} \quad (2.39)$$

with

$$\begin{aligned} H_+ &= \begin{bmatrix} \epsilon_p + \frac{F+G}{2}(k_x^2 + k_y^2) & Ak_+ \\ A^*k_- & \epsilon_d - \frac{F+G}{2}(k_x^2 + k_y^2) \end{bmatrix}, \\ H_{+-} &= \begin{bmatrix} \frac{G-F}{2}(k_x^2 - k_y^2) - iNk_xk_y & 0 \\ 0 & \frac{F-G}{2}(k_x^2 - k_y^2) + iNk_xk_y \end{bmatrix}, \\ H_- &= \begin{bmatrix} \epsilon_p + \frac{F+G}{2}(k_x^2 + k_y^2) & Ak_- \\ A^*k_+ & \epsilon_d - \frac{F+G}{2}(k_x^2 + k_y^2) \end{bmatrix}, \end{aligned}$$

where $k_{\pm} = k_x \pm ik_y$ and $d_{\pm} = (d_{x^2-y^2} \pm id_{xy})/\sqrt{2}$.

With additional TR symmetry \mathcal{T} respected by Maxwell equations ($\mathcal{T} = \mathcal{K}$ with \mathcal{K} the complex conjugate operator), we find

$$\begin{aligned} \langle p_+ | Ak_+ | d_+ \rangle &= \langle p_+ | \mathcal{K}^\dagger \mathcal{K} (Ak_+) \mathcal{K}^\dagger \mathcal{K} | d_+ \rangle \\ &= -\langle p_- | A^*k_- | d_- \rangle, \end{aligned} \quad (2.40)$$

indicating that A is purely imaginary.

Dropping the second order off-diagonal terms $\pm iNk_xk_y$ and $\pm \frac{G-F}{2}(k_x^2 - k_y^2)$, which contribute as high-order perturbations, Hamiltonian (2.39) is in a block diagonal form. Putting the “Fermi level” in the middle of ϵ_d^0 and ϵ_p^0 and taking $D_d = -D_p = D$, we have the simplified Hamiltonian

$$\mathcal{H}'(\mathbf{k}) = \begin{pmatrix} \mathcal{H}_+ & 0 \\ 0 & \mathcal{H}_- \end{pmatrix} \quad (2.41)$$

with

$$\mathcal{H}_{\pm} = \begin{pmatrix} M + Bk^2 & Ak_{\pm} \\ A^*k_{\mp} & -M - Bk^2 \end{pmatrix}, \quad (2.42)$$

where $M = (\epsilon_p^0 - \epsilon_d^0)/2$ and $B = (F + G)/2 + D$.

Since the effective Hamiltonian $\mathcal{H}'(\mathbf{k})$ in Eq. (2.41) is in a similar form as Bernevig-Hughes-Zhang (BHZ) model for CdTe/HgTe/CdTe quantum well [10], the system then can support an optical quantum “spin” Hall effect due to the band inversion mechanism. However, we should emphasize that the underlying physics between our photonic crystal and HgTe quantum well are different since we are focusing on a system governed by Maxwell equations instead of Schrödinger equation.

2.6 Topological edge states in photonic crystals

2.6.1 Edge state in 2D systems

We consider a ribbon of photonic crystal after band inversion by cladding its two edges in terms of two photonic crystals with trivial band gap (namely before band inversion) at the same frequency window, which prevents possible edge states from leaking into free space. It should be kept in mind that, since the cluster of six cylinders is the basic block of the present design, we keep them intact for discussions of main physics. As displayed in figure 2.8(a), there appear additional states as indicated by the double degenerate red curves within the bulk gap. Checking the real-space distribution of E_z field

at typical momenta around Γ point (A and B in the enlarged vision of figure 2.8(a) with $k_x = \pm 0.04 \frac{2\pi}{a_0}$), we find that the in-gap states locate at the ribbon edges and decay exponentially into bulk as displayed in figure 2.8(b) (two other states are localized at the other ribbon edge and not shown explicitly). As shown in the right insets of figure 2.8(b), the Poynting vectors exhibit a nonzero downward/upward EM energy flow for the pseudo spin-down/-up state even averaged over time. This indicates unambiguously counter propagations of EM energy at the sample edge associated with the two pseudo spin states, the hallmark of a quantum spin Hall effect (QSHE) state [9, 11]. It is noticed that the Poynting vector describes energy flows in systems governed by Maxwell equations, and therefore the distributions shown in figure 2.8(b) can be observed in experiments. The photonic QSHE in the present system can also be confirmed by evaluating the \mathbb{Z}_2 invariant based on a $k \cdot p$ model around Γ point.

Since the pseudo TR symmetry and the pseudo spin rely on the C_6 point symmetry, deformations in the system which break the crystalline order and thus the pseudo TR symmetry would mix the two pseudo-spin channels as in other \mathbb{Z}_2 topological photonic systems [31, 33]. Actually there is a tiny gap at Γ point in figure 2.8(a) (unnoticeable in the present scale) due to the reduction of C_6 crystalline symmetry at the ribbon edge.

2.6.2 Energy propagations via topological edge states

Now we study propagation of electromagnetic (EM) wave excited by a source via the topological edge states in a finite sample. The time-dependent Maxwell equations are [58]

$$\frac{\partial \mathbf{H}}{\partial t} = -\frac{1}{\mu_0} (\vec{\nabla} \times \mathbf{E} + S_H), \quad (2.43)$$

$$\frac{\partial \mathbf{E}}{\partial t} = \frac{1}{\varepsilon(\mathbf{r})} (\vec{\nabla} \times \mathbf{H} - S_E), \quad (2.44)$$

where $\mathbf{H} = (H_x, H_y, 0)$ and $\mathbf{E} = (0, 0, E_z)$ for the TM mode, μ_0 is the magnetic permeability of vacuum, and $S_{E/H}$ is the external electric/magnetic current density provided by sources. Equations (2.44) are solved numerically by using the finite-difference time domain method [58].

First we consider a 2D rectangle sample of topological photonic crystal of size $40\vec{a}_1 \times 20(\vec{a}_1 + \vec{a}_2)$ embedded in a larger trivial photonic crystal (\vec{a}_1 and \vec{a}_2 are lattice vectors shown in figure 2.3). Parameters for trivial/topological region are the same as those in figure 2.8. We place a harmonic source $S_E = E_0 e^{i\omega t} \hat{z}$ to inject an EM wave of E_z field at the interface between topological and trivial regions, with frequency $\omega = 0.45c/a_0$ inside the topological energy gap for the given parameters. We find that the EM energy $u_{E_z}(\mathbf{r}) = \varepsilon(\mathbf{r})|E_z(\mathbf{r})|^2/2$ is distributed along the interface (see figure 2.9(a)), indicating clearly the existence of topological edge state of the system.

In order to manifest the pseudo spin specified edge states of the present \mathbb{Z}_2 topological photonic crystal, we further consider an infinite system with the lower/upper half region occupied by topological/trivial photonic crystal. When an EM wave of pseudo spin-up channel is injected from a source S_+ , we find that the excited EM wave propagates unidirectionally to the left along the interface, as shown in figure 2.9(b). Similarly, when we inject an EM wave of pseudo spin-down state by a source S_- , we find that the excited state propagates only to the right, as displayed in figure 2.9(c). These two chiral edge states specific to the pseudo spin-up and -down states manifests the \mathbb{Z}_2 invariant of the present system. In real experiments, one prepares source S_+/S_- in terms $H_0 e^{i\omega t} (\hat{x} \mp i\hat{y})$ at the center of a hexagon, which generates EM wave with in-plane magnetic field of anticlockwisely/clockwisely circular polarization,

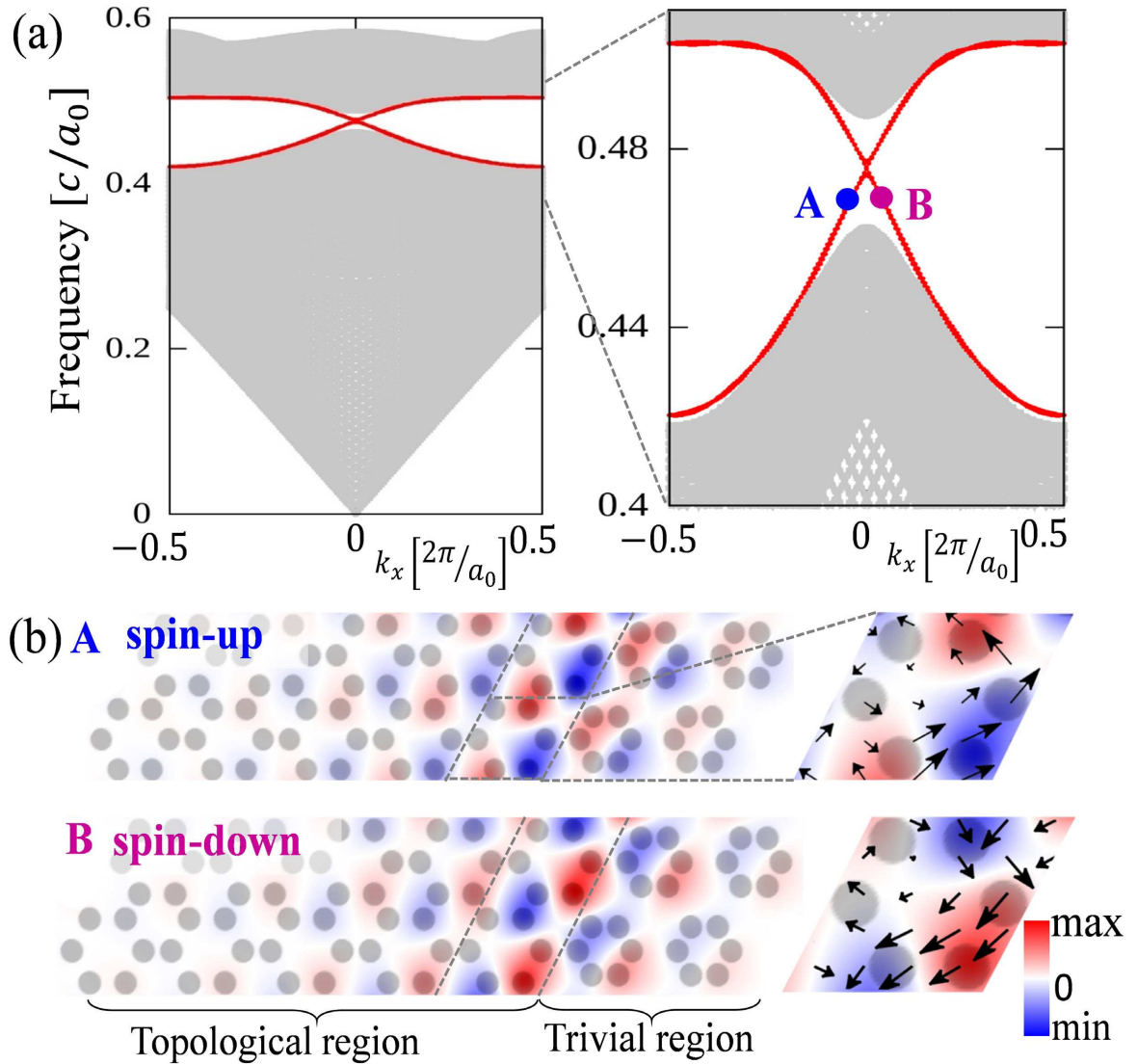


Figure 2.8: (a) Dispersion relation of a ribbon-shaped 2D topological photonic crystal, which is infinite in one direction and of 45 and 6 artificial atoms for the topological and trivial regions respectively in the other direction. Right panel: enlarged view of (a) around the band gap. Red curves are for topological edge states. (b) Real-space distributions of E_z fields at points A and B indicated in the right panel of (a). Right panels: time-averaged Poynting vectors \vec{S} over a period.

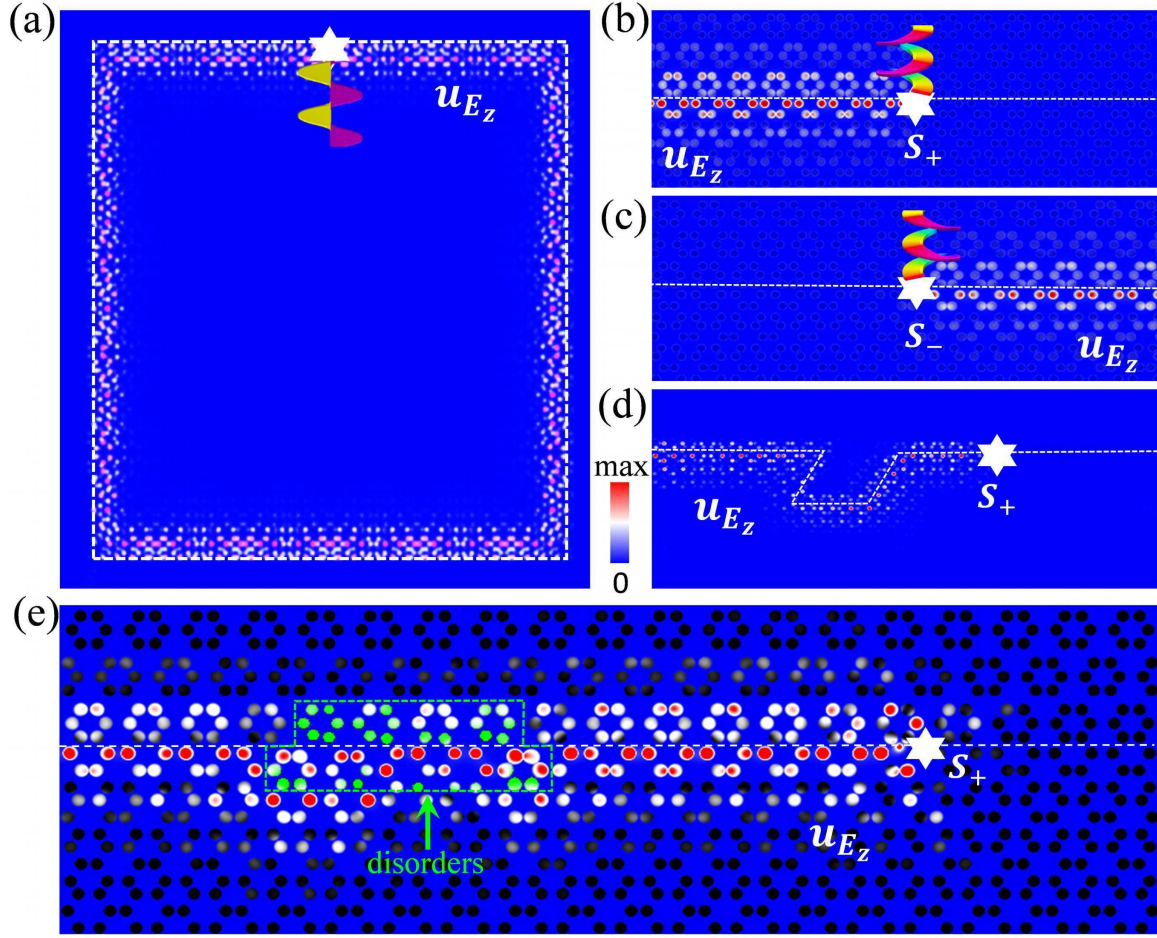


Figure 2.9: (a) Topological edge states excited by a harmonic source with linear polarization. (b) and (c) Unidirectional energy propagations excited by sources generating EM waves characterized by E_z fields with wave functions of positive and negative angular momenta. (d) and (e) Propagations of excited helical edge state along interfaces with sharp turning angles and disorders (deformed hexagons inside green dashed box). White dot lines are interfaces between topological and trivial regions, and stars are sources. Parameters are taken the same as those in Figs. 5(a) and (b) in the main text.

and thus out-of-plane electric field with wave function of positive/negative angular momentum.

An important property of topological edge states is that they are immune to various defects. In order to check robustness of the topological photonic state realized in the present scheme, one can introduce intentionally defects into the system [33]. As the first example of possible defects, we consider a sharply bent interface where the topological photonic crystal is replaced by the trivial one in a region of $3\vec{a}_1 \times 3\vec{a}_2$ (see figure 2.9(d)). A source S_+ is placed at the interface to stimulate pseudo spin-up EM wave with frequency $\omega = 0.45c/a_0$ inside topological band gap. Solving Eq. (2.44), it is found that, as displayed in figure 2.9(d), the EM wave can go ground this rhombic defect and maintain the unidirectional propagation, which confirms the robustness of topological edge states against sharply bent interfaces.

As the second example of defects, we introduce deformed artificial atoms at the interface. As shown in figure 2.9(e), inside the region indicated by the green dashed box diameters of green cylinders d and ratios a_0/R of artificial atoms are chosen from $[0.2a_0, 0.28a_0]$ and $[2.78, 3.33]$ respectively in a random

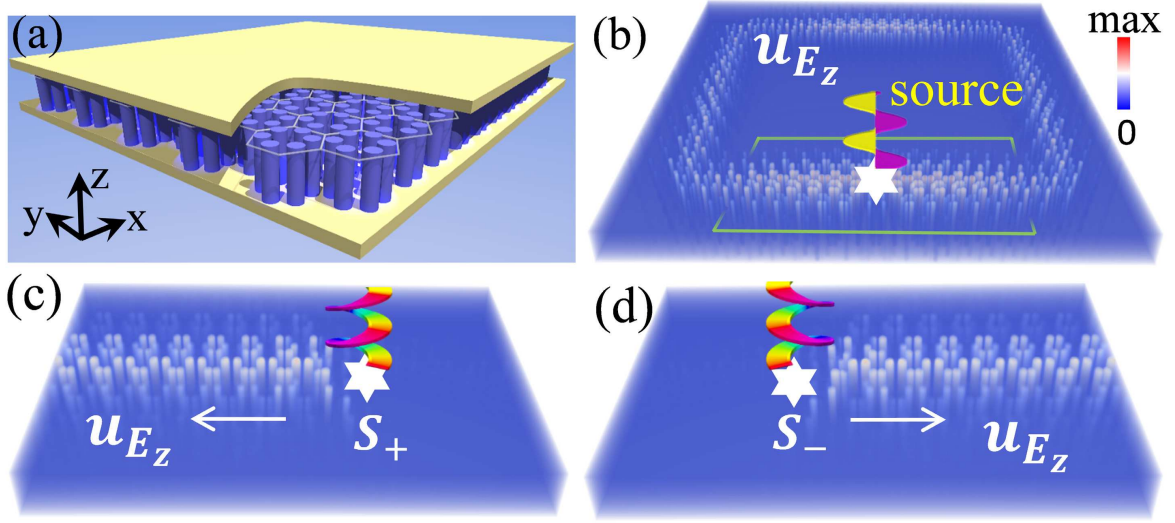


Figure 2.10: (a) 3D photonic crystal of height h with two horizontal gold plates placed at two ends symmetrically. (b) Distribution of energy-density of E_z field $u_{E_z}(\mathbf{r}) = \varepsilon(\mathbf{r})|E_z(\mathbf{r})|^2/2$ in the 3D topological photonic crystal in (a) stimulated by a linearly polarized source. (c)/(d) Leftward/rightward unidirectional energy propagation stimulated by source S_+/S_- which injects E_z field with wave function of positive/negative angular momentum in the region denoted by green solid frame in (b). The lattice constant and diameter of cylinder are kept same in the whole space $a_0 = 1\mu\text{m}$ and $d = 0.24\mu\text{m}$, while the edge length of hexagon is $R = 0.345a_0$ ($a_0/R = 2.9$) and $R = 0.32a_0$ ($a_0/R = 3.125$) in topological and trivial regions, and the frequency of all sources is $\omega = 135.6\text{THz}$ within the topological band gap. In the 3D system the height of cylinder is $h = 1\mu\text{m}$. Other parameters are same as those in figure 2.6.

way, and positions of some cylinders are shifted randomly by distances chosen from $[-0.03a_0, 0.03a_0]$. As displayed in figure 2.9(e), the excited edge state passes through the disordered region without noticeable backscattering, indicating that the topological state remains stable against these moderate disorders [59, 60]. The topology will be destroyed by strong disorders when the dispersions of edge states are pushed into bulk bands. A systematic analysis, such as those carried out in previous works [61, 62], on possible influences of disorders to the present topological photonics would become an issue of future work.

2.6.3 Experimental realizations

For experimental implementation of the present topological state, the finite height of cylinders along z direction has to be taken into account. We consider a square sample of topological photonic crystal sandwiched by two horizontal gold plates (see figure 2.10(a)) with separation h chosen to prevent photonic bands with nonzero k_z from falling into the topological band gap. Damping of EM wave in gold plates are taken into account by adopting complex reflective index for gold. The size of topological sample is $40\vec{a}_1 \times 20(\vec{a}_1 + \vec{a}_2)$ with all four edges clad by a trivial photonic crystal. A harmonic line source $\mathbf{E} = E_0 e^{i\omega t} \hat{z}$ is placed parallel to dielectric cylinders to inject EM wave at the interface with the frequency in the topological band gap. We simulate the 3D system by solving time-dependent Maxwell equations using finite difference time-domain method [58]. Since any harmonic

source preserves TR symmetry respected by Maxwell equations, the system exhibits helical topological edge states as shown in figure 2.10(b). When an EM wave characterized by E_z field with wave function of positive/negative angular momentum is injected by line source S_+/S_- , leftward/rightward unidirectional energy propagation takes place (see Figs. 2.10(c) and (d)), as expected from the bulk topology. In real experiments, one prepares source S_+/S_- in terms $H_0 e^{i\omega t} (\hat{x} \mp i\hat{y})$ with H_0 an arbitrary amplitude, ω a frequency and $\hat{x}(\hat{y})$ the unit vector along $x(y)$ direction, which generates in-plane magnetic field with anticlockwisely/clockwisely circular polarization, and thus the out-of-plane E_z field with wave function of positive/negative angular momentum.

2.7 Conclusion

We derive a two-dimensional photonic crystal with nontrivial topology purely based on conventional dielectric material, simply by deforming honeycomb lattice of cylinders. A pseudo time-reversal symmetry is constructed in terms of the time-reversal symmetry respected by Maxwell equations in general and the C_6 crystal symmetry upon design, which enables the Kramers doubling with the role of pseudo spin played by the angular momentum of wave function of the out-of-plane electric field of transverse magnetic modes. The present topological photonic crystal with simple design backed up by the symmetry consideration can be fabricated relatively easy as compared with other proposals, and is expected to leave impacts to the topological physics and related materials science.

Honeycomb Lattice with Kekulé Distortions

3.1 Honeycomb lattice

3.1.1 Tight-binding model

Honeycomb lattice is a natural platform for realizing Dirac linear dispersion [43]. Intensive interests in questing for systems with honeycomb lattice structure flourished since the discovery of graphene: a monolayer of carbon atoms [44, 63]. A minimal tight-binding Hamiltonian describing the dispersion relation of π electrons in graphene is [46]

$$H_0 = -t \sum_{\langle i,j \rangle, \sigma} (a_{i,\sigma}^\dagger b_{j,\sigma} + H.c.), \quad (3.1)$$

where $a_{i,\sigma}$ ($b_{i,\sigma}$) annihilates a π electron at site i of sublattice A (B) and spin σ , $\langle i,j \rangle$ runs over two nearest neighbors with hopping energy t (see figure 1.3). Transforming Hamiltonian (3.1) into the momentum space, we arrive at the Hamiltonian close to the K and K' points, which are the corners of the Brillouin zone (see detailed derivations in Appendix A.1)

$$H_\sigma^{NN} = -v_f \begin{pmatrix} 0 & k_x - i\nu k_y \\ k_x + i\nu k_y & 0 \end{pmatrix} = -v_f (\sigma_x k_x + \tau_z \sigma_y k_y) \quad (3.2)$$

on the basis $[a_\sigma, b_\sigma]$, where $\nu = \pm 1$ at the K and K' respectively, the Fermi velocity $v_f = \sqrt{3}a_0 t / 2$ with a_0 the lattice constant, $\sigma_{x,y,z}$ are the Pauli matrices for sublattice degree of freedom, and $\tau_{x,y,z}$ are those for valley degree of freedom. Eigenenergies of Eq. (3.2) are $E = \pm v_f |\mathbf{k}|$, forming a Dirac cone at the K and K' points, as shown in figure 1.4.

3.1.2 Topological phases in honeycomb lattice

It has been well studied that a band gap can be opened at the Dirac point by a staggered electric potential μ for two sublattices [64, 65]

$$\mathcal{H}_V = \mu \sigma_z, \quad (3.3)$$

which induces a same mass μ at the two K points, and thus the total Chern number $C = C_K + C_{K'}$ is zero according to Eq. (1.13) [see figure 3.1(a)]. Another way of generating mass terms at Dirac points was introduced by Haldane [6]. The author revealed that a QAHE can be realized when complex hopping integrals t' among next-nearest-neighboring sites of honeycomb lattice are taken into account (see figure 1.3). The effective low-energy Hamiltonian describing the complex hopping textures is

$$\mathcal{H}_{\text{Haldane}} = -3|t'| \cos \phi \sigma_0 + 3\sqrt{3}|t'| \sin \phi \tau_z \sigma_z, \quad (3.4)$$

where $t' = |t'| \exp(i\phi)$ (see details in Appendix A.1). The first term above simply shifts the Fermi level without affecting topology of the system and thus can be dropped. The mass function $3\sqrt{3}|t'| \sin \phi \tau_z$ in the second term above is opposite at the two valleys and thus results in a total Chern number 1, i.e. a QAHE is realized. Later, it was revealed that the intrinsic spin-orbit coupling (SOC) in honeycomb lattice can provide this complex hopping integrals with $\phi = \pi/2$ [7, 8]. The effective Hamiltonian for the SOC at the two valleys (the K and K' points) is

$$H_{\text{soc}} = \lambda \tau_z \sigma_z s_z \quad (3.5)$$

with s_z the Pauli matrix for spin degree of freedom, and λ the strength of spin-orbit coupling (see detailed derivations in Appendix A.1). The non-vanishing SOC in Eq. (3.5) opens a bulk band gap at the $K(K')$ points, which drives spinful electrons into a topological state with the time-reversal symmetry preserved, known as QSHE [7–11].

Possible topological phases can be identified by evaluating Berry curvatures at the two valleys, where we have a minimal band gap. The topological charges carried by Dirac fermions are given in Eq. (1.13) for a simple Dirac Hamiltonian. As shown in figure 3.1(a), for the pristine graphene, C_K and $C_{K'}$ take opposite signs at the K and K' points since they are linked by the time-reversal symmetry. With the SOC in Eq. (3.5) turned on, the intrinsic SOC introduces opposite mass terms $\lambda \sigma_z s_z$ and $-\lambda \sigma_z s_z$ at the K and K' points respectively. On the other hand, the chiralities at the two valleys are opposite. The topological charges thus are the same with an absolute value 1/2 in the same spin and the same sublattice channels according to Eq. (1.13). As displayed in figure 3.1(b) for the QSHE with topological gap opened by the intrinsic SOC, the Chern number in the spin-up channel is 1, and -1 in the spin-down channel because of the time-reversal symmetry. Similarly, we can exhaust other possible ways of alternating $C_{K(K')}$. For example, C_K can be flipped in both spin channels by introducing an anti-ferromagnetic exchange field at two sublattice sites or applying a circularly polarized light [37, 66, 67] (see figure 3.1(c)). The configuration of Berry curvatures in figure 3.1(d) can be realized by the Haldane model [6]. Further, one can reach a topological state only in one spin channel and realize a novel QAHE [see figure 3.1(e)], which will be discussed in details in the next chapter.

For most proposals of realizing topological states in honeycomb lattice, SOC is indispensable. However, it turns out that SOC for graphene is too small to open a significant topological band gap for experimental observations. Attentions then are paid to the two-dimensional (2D) group IV honeycomb lattice with stronger SOC, including Silicene [65] and fluorinated stanene [68]. The requirement for strong SOC limits number of possible platforms for realizing QSHE. In this chapter, we propose a novel way of opening topological band gap simply by detuning hopping energies among nearest-neighbor sites to form a Kekulé texture. Since the gap is purely of electric origin, it can be in the order of $\sim 0.1t_0$, where t_0 is the hopping energy between two nearest-neighbor sites.

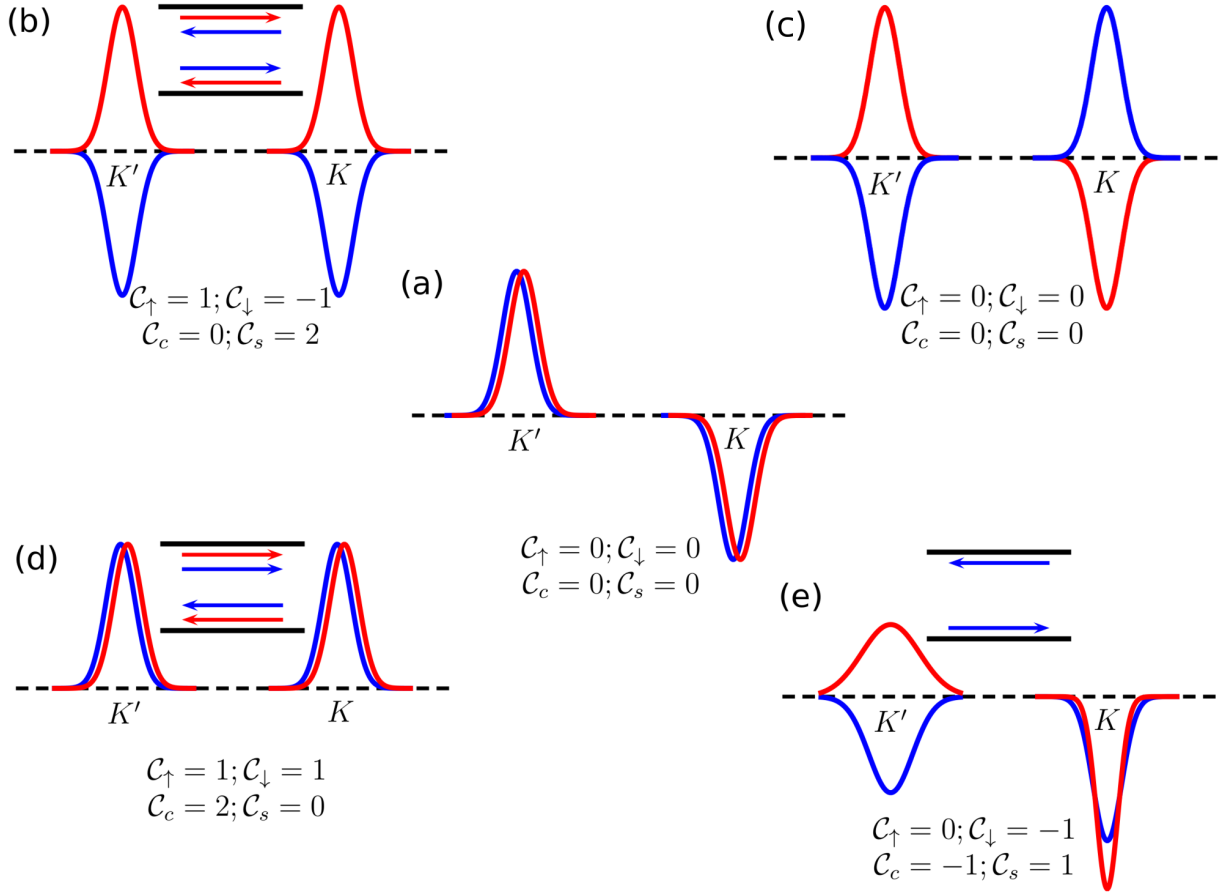


Figure 3.1: Berry curvatures at two valleys for (a) pristine graphene, (b) quantum spin Hall effect (c) trivial states with broken time-reversal symmetry (d) quantum anomalous Hall effect and (e) topological state only in one of the two spin channels. Upper insets in (b), (d) and (e) are edge currents. Red and blue curves are for spin-up and spin-down channels respectively. C_\uparrow and C_\downarrow are Chern numbers of spin-up and spin-down electrons respectively, $C_c = C_\uparrow + C_\downarrow$ and $C_s = C_\uparrow - C_\downarrow$ are charge and spin Chern numbers respectively (see figure also in Ref. [17]).

3.2 Topological properties induced by Kekulé hopping textures

3.2.1 Tight-binding model and emergent orbitals

We start from a spinless tight-binding Hamiltonian on honeycomb lattice

$$H = \varepsilon_0 \sum_i c_i^\dagger c_i + t_0 \sum_{\langle i,j \rangle} c_i^\dagger c_j + t_1 \sum_{\langle i',j' \rangle} c_{i'}^\dagger c_{j'}, \quad (3.6)$$

where c_i is the annihilation operator of electron at atomic site i with on-site energy ε_0 satisfying the anti-commutation relation, $\langle i,j \rangle$ and $\langle i',j' \rangle$ run over nearest-neighbor sites inside and between hexagonal unit cells with hopping energies t_0 and t_1 respectively [see Fig. 3.2(a)]. The orbitals are considered to be the simplest one without any internal structure, such as the π electron of graphene. Below we are going to detune the hopping energy t_1 while keeping t_0 constant, and elucidate possible changes in electronic

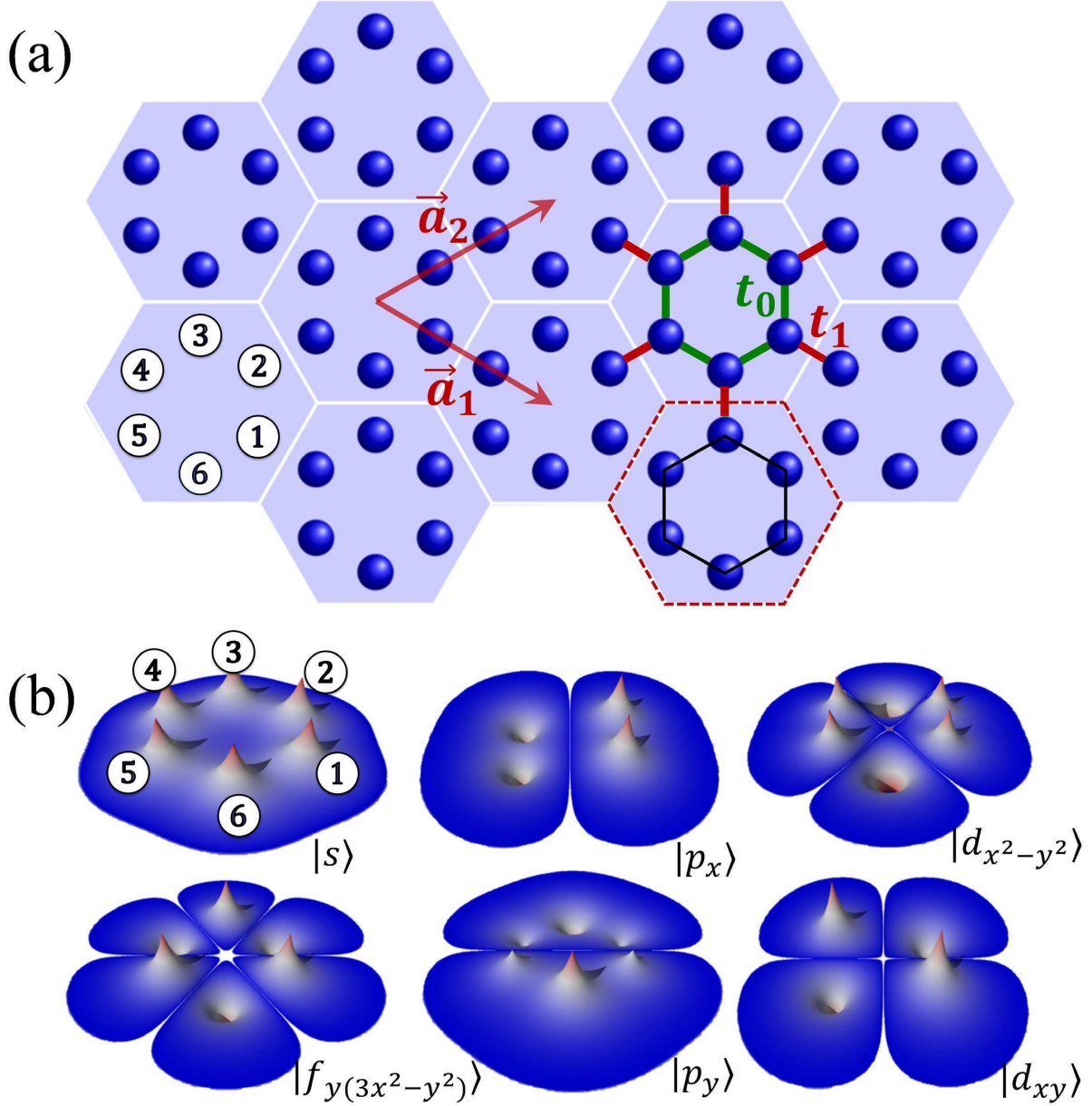


Figure 3.2: (a) Honeycomb lattice with hopping energies between nearest-neighbor sites: t_0 inside hexagons as denoted by the green bonds and t_1 between hexagons by red ones. The Red dashed hexagon is the primitive cell of triangular lattice with lattice vectors \vec{a}_1, \vec{a}_2 and lattice constant $a_0 = |\vec{a}_1| = |\vec{a}_2|$. Numbers 1, ..., 6 in circle index atomic sites within a hexagon. (b) Emergent orbitals in the hexagonal artificial atom.

states. In this case, the pristine honeycomb lattice of individual atomic sites is better to be considered as a triangular lattice of hexagons, with the latter characterized by C_6 symmetry.

Let us start with the Hamiltonian within a single hexagonal unit cell

$$H_0 = t_0 \Psi^\dagger \begin{pmatrix} 0 & 1 & 0 & 0 & 0 & 1 \\ 1 & 0 & 1 & 0 & 0 & 0 \\ 0 & 1 & 0 & 1 & 0 & 0 \\ 0 & 0 & 1 & 0 & 1 & 0 \\ 0 & 0 & 0 & 1 & 0 & 1 \\ 1 & 0 & 0 & 0 & 1 & 0 \end{pmatrix} \Psi, \quad (3.7)$$

where $\Psi = [c^1, c^2, c^3, c^4, c^5, c^6]^T$ [see Fig. 3.2(a)]. The eigenstates of Hamiltonian H_0 are given by

$$\begin{aligned} |s\rangle &= [1, 1, 1, 1, 1, 1]^T; \\ |p_x\rangle &= [1, 1, 0, -1, -1, 0]^T; \\ |p_y\rangle &= [1, -1, -2, -1, 1, 2]^T; \\ |d_{x^2-y^2}\rangle &= [1, 1, -2, 1, 1, -2]^T; \\ |d_{xy}\rangle &= [1, -1, 0, 1, -1, 0]^T; \\ |f_{y(3x^2-y^2)}\rangle &= [1, -1, 1, -1, 1, -1]^T \end{aligned} \quad (3.8)$$

with eigenenergies $2t_0, t_0, t_0, -t_0, -t_0$ and $-2t_0$ respectively, up to normalization factors. As shown in Fig. 3.2(b), the *emergent* orbitals accommodated on the hexagonal “artificial atom” take the shapes similar to the conventional s , p , d and f atomic orbitals.

3.2.2 Pseudo-time-reversal symmetry and pseudospin

Similar to the discussion in Section 2.3.3, a pseudo-TR symmetry operator can be composed in the present system with C_6 symmetry: $\mathcal{T} = \mathcal{U} \mathcal{K}$ with \mathcal{K} the complex conjugate operator and $\mathcal{U} = -i\sigma_y$, where σ_y is the Pauli matrix. It can be checked straightforwardly that \mathcal{U} corresponds to $\pi/2$ rotation for p orbitals and $\pi/4$ rotation for d orbitals given in Eq. (3.8), which yields $\mathcal{U}^2 = -1$ in the space formed by the p and d orbitals [13]. Therefore, the pseudo-TR symmetry satisfies the relation $\mathcal{T}^2 = -1$, same as that for fermionic particles even though the spin degree of freedom of electron has not been considered explicitly. This indicates that electrons acquire a new *pseudospin* degree of freedom in the present system as far as the low-energy physics is concerned. It is noticed that although the high-energy states $|s\rangle$ and $|f\rangle$ are not eigenvectors of \mathcal{T} , they do not affect topological properties of the present system.

Explicitly the wave functions carrying pseudospins are given by the emergent orbitals with eigen angular momentum

$$|p_\pm\rangle = \frac{1}{\sqrt{2}}(|p_x\rangle \pm i|p_y\rangle); \quad |d_\pm\rangle = \frac{1}{\sqrt{2}}(|d_{x^2-y^2}\rangle \pm i|d_{xy}\rangle). \quad (3.9)$$

Distinguished from the intrinsic spin, the pseudospin is directly related to the chiral current density on the hexagon. For a lattice model, the current density between two sites is given by $I_{jk} = (i/\hbar)[t_0 c_j^\dagger c_k - t_0^* c_k^\dagger c_j]$. The current distributions evaluated using wave functions in Eq. (3.9) for the pseudospin-up and

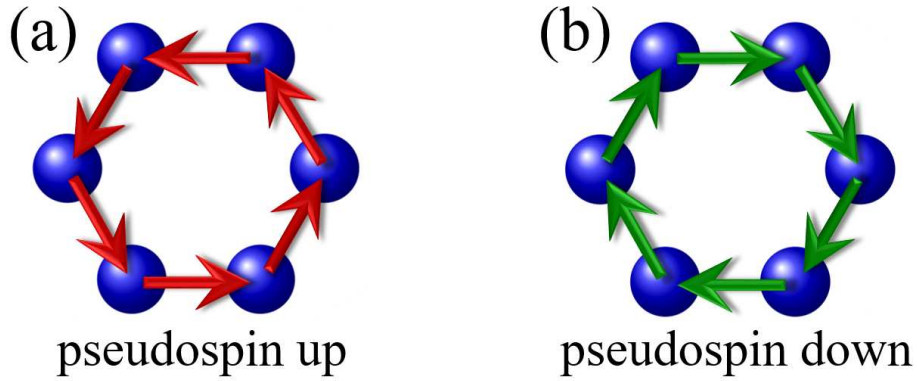


Figure 3.3: (a) and (b) Current densities in the pseudospin-up channel (p_+ or d_+) and pseudospin-down channel (p_- or d_-) respectively.

-down states are shown in Figs. 3.3(a) and (b) with anticlockwisely and clockwisely circulating currents. By considering the hexagonal artificial atoms composed by six sites in honeycomb lattice, one harvests states with angular momenta merely from simple orbitals, such as π electrons in graphene. The pseudo-TR symmetry is supported by the C_6 crystal symmetry, sharing the same underlying physics with the topological crystalline insulator [56]. However, for crystal-symmetry-protected topological insulators addressed so far, strong SOCs are required to achieve band inversions [69–71], which is different from the present approach as revealed below.

3.3 Low-energy model for \mathbb{Z}_2 topological states

We calculate the energy dispersion of Eq. (3.6) for several typical values of t_1 (hereafter the on-site energy is put as $\varepsilon_0 = 0$ without losing generality). As shown in Fig. 3.4, there are two two-fold degeneracies at the Γ point corresponding to the two irreducible representations of the C_6 point group. Projecting the wave functions for $t_1 = 0.9t_0$ onto the orbitals given in Fig. 3.2(b), it is found that the topmost two valance bands show the character of d orbitals whereas the lowest two conduction bands behave like p orbitals [see Fig. 3.4(a)], with the order in energy same as those listed in Eq. (3.8). For $t_1 = t_0$, the d and p bands become degenerate at the Γ point and double Dirac cones appear [see Fig. 3.4(b)], which are equivalent to the ones at K and K' points in the unfolded Brillouin zone of honeycomb lattice with the rhombic unit cell of two sites. When t_1 increases further from t_0 , a band gap reopens at the Γ point. As shown in Fig. 3.4(c) for $t_1 = 1.1t_0$, the valence (conduction) bands are now occupied by p (d) orbitals around the Γ point, opposite to the order away from the Γ point and to that before gap closing. Therefore, a band inversion between p and d orbitals takes place at the Γ point when the inter-hexagon hopping energy is increased across the topological transition point $t_1 = t_0$, namely the pristine honeycomb lattice.

We can characterize the topological property of the gap-opening transition shown in Fig. 3.4 by a low-energy effective Hamiltonian around the Γ point. Since the bands near the Fermi level are predominated by p and d orbitals, it is sufficient to downfold the six-dimensional Hamiltonian $H(\mathbf{k})$ associated with the tight-binding model (3.6) into the four-dimensional subspace $[p_+, d_+, p_-, d_-]$. The second

term in Eq. (3.6) is then simply given by

$$h'_0 = \begin{pmatrix} t_0 & 0 & 0 & 0 \\ 0 & -t_0 & 0 & 0 \\ 0 & 0 & t_0 & 0 \\ 0 & 0 & 0 & -t_0 \end{pmatrix}. \quad (3.10)$$

Contributions from the third term in Eq. (3.6) to the effective Hamiltonian should be evaluated perturbatively. First, we list the inter-hexagon hoppings in terms of 6×6 matrices $h_1, h_2, h_3, h_1^\dagger, h_2^\dagger$ and h_3^\dagger with

$$h_1 = \begin{pmatrix} 0 & 0 & 0 & t_1 & 0 & 0 \\ 0 & 0 & 0 & 0 & 0 & 0 \\ 0 & 0 & 0 & 0 & 0 & 0 \\ 0 & 0 & 0 & 0 & 0 & 0 \\ 0 & 0 & 0 & 0 & 0 & 0 \\ 0 & 0 & 0 & 0 & 0 & 0 \end{pmatrix}, \quad h_2 = \begin{pmatrix} 0 & 0 & 0 & 0 & 0 & 0 \\ 0 & 0 & 0 & 0 & t_1 & 0 \\ 0 & 0 & 0 & 0 & 0 & 0 \\ 0 & 0 & 0 & 0 & 0 & 0 \\ 0 & 0 & 0 & 0 & 0 & 0 \\ 0 & 0 & 0 & 0 & 0 & 0 \end{pmatrix},$$

$$h_3 = \begin{pmatrix} 0 & 0 & 0 & 0 & 0 & 0 \\ 0 & 0 & 0 & 0 & 0 & 0 \\ 0 & 0 & 0 & 0 & 0 & t_1 \\ 0 & 0 & 0 & 0 & 0 & 0 \\ 0 & 0 & 0 & 0 & 0 & 0 \\ 0 & 0 & 0 & 0 & 0 & 0 \end{pmatrix}$$

on the basis of $[c^1, c^2, c^3, c^4, c^5, c^6]$. Following the standard procedures, they can be projected to the subspace spanned by $[p_+, d_+, p_-, d_-]$

$$h'_1 = \frac{t_1}{12} \begin{pmatrix} -2 & \sqrt{3}-i & -1-\sqrt{3}i & 2i \\ -\sqrt{3}-i & 2 & -2i & -1+\sqrt{3}i \\ -1+\sqrt{3}i & -2i & -2 & \sqrt{3}+i \\ 2i & -1-\sqrt{3}i & -\sqrt{3}+i & 2 \end{pmatrix},$$

$$h'_2 = h'_1, \quad h'_3 = \frac{t_1}{6} \begin{pmatrix} -1 & i & 1 & i \\ i & 1 & -i & 1 \\ 1 & -i & -1 & -i \\ i & 1 & -i & 1 \end{pmatrix}. \quad (3.11)$$

With Fourier transformations of matrices in Eqs. (3.10) and (3.11), one obtains the effective low-energy Hamiltonian $H'(\mathbf{k})$ on the basis $[p_+, d_+, p_-, d_-]$ in the momentum space. Expanding $H'(\mathbf{k})$ around the Γ point up to the lowest-orders of \mathbf{k} , one arrives at

$$H'(\mathbf{k} \rightarrow \Gamma) = \begin{pmatrix} H_+(\mathbf{k}) & 0 \\ 0 & H_-(\mathbf{k}) \end{pmatrix} \quad (3.12)$$

with

$$H_\pm(\mathbf{k}) = \begin{pmatrix} -\delta t + \frac{1}{2}a_0^2 t_1 \mathbf{k}^2 & \frac{i}{2}a_0 t_1 k_\pm \\ -\frac{i}{2}a_0 t_1 k_\mp & \delta t - \frac{1}{2}a_0^2 t_1 \mathbf{k}^2 \end{pmatrix}, \quad (3.13)$$

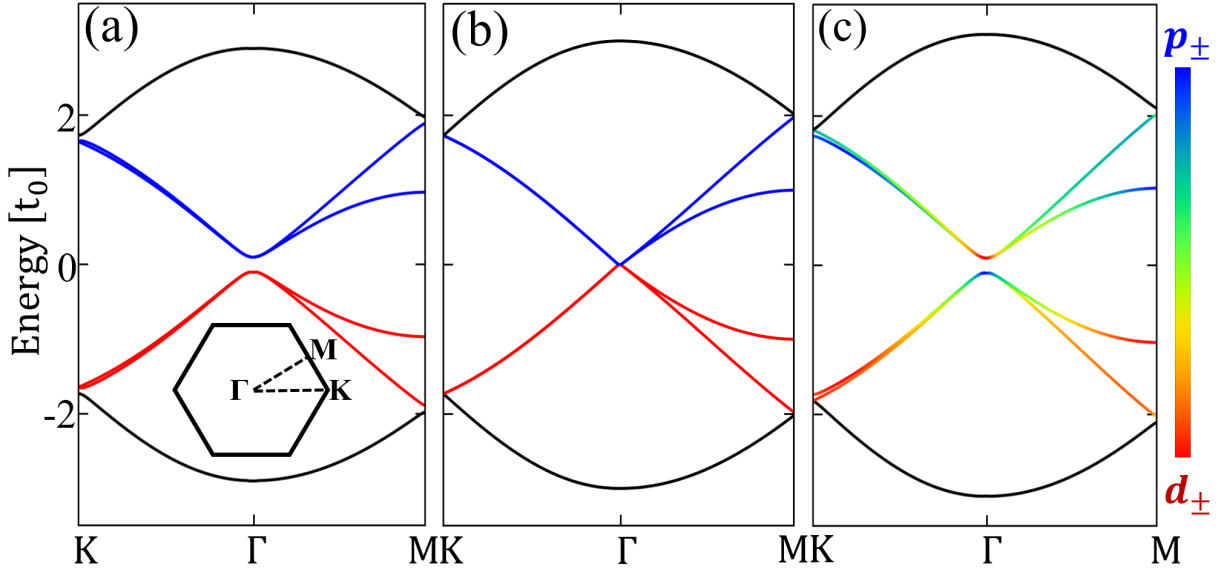


Figure 3.4: Band dispersions for the system given in Fig. 3.2: (a) $t_1 = 0.9t_0$ (Inset: Brillouin zone of the triangular lattice), (b) $t_1 = t_0$ and (c) $t_1 = 1.1t_0$. Blue and yellow are for $|p_{\pm}\rangle$ and $|d_{\pm}\rangle$ orbitals respectively, and rainbow for hybridization between them. The on-site energy is taken $\varepsilon_0 = 0$.

where $\delta t = t_1 - t_0$, $\mathbf{k} = (k_x, k_y)$, $k_{\pm} = k_x \pm ik_y$, $\mathbf{0}$ is a 2×2 zero matrix, and a_0 is the lattice constant of the triangular lattice. For $\delta t = 0$, the Hamiltonians $H_+(\mathbf{k})$ and $H_-(\mathbf{k})$ in Eq. (3.13) are the same as the well-known one for honeycomb lattice around the K and K' points [46], where the quadratic terms of momentum in the diagonal parts can be neglected.

3.4 Topological phase transitions

For $\delta t > 0$, however, the quadratic terms are crucially important since they induce a band inversion [10], resulting in the orbital hybridization in the band structures shown in Fig. 3.4(c). Associated with a skyrmion in the momentum space for the orbital distributions in the individual pseudospin channels, a topological state appears characterized by the \mathbb{Z}_2 topological invariant [7, 8, 13, 38]. It is clear that for $\delta t < 0$ there is no band inversion taking place and thus the band gap is trivial as shown in Fig. 3.4(a).

It is worthy noticing that, comparing with the Kane-Mele model for the honeycomb lattice [7, 8], the mass term $\delta t (> 0)$ in Eq. (3.13) can be considered as an effective SOC associated with the pseudospin, namely $\lambda_{\text{eSOC}} = \delta t$. For $\delta t = 0.1t_0$, a moderate texture in hopping energies, the effective SOC is approximately 3000 times larger than the *real* SOC in magnitude in graphene where $\lambda_{\text{SOC}} \simeq 0.1\text{meV}$ and $t_0 = 2.7\text{eV}$. The huge effective SOC is due to its pure electronic character as compared with the intrinsic SOC originated from the relativistic effect. This is one of the fantastic aspects of the present approach, which renders a topological gap corresponding to temperature of thousands of Kelvin.

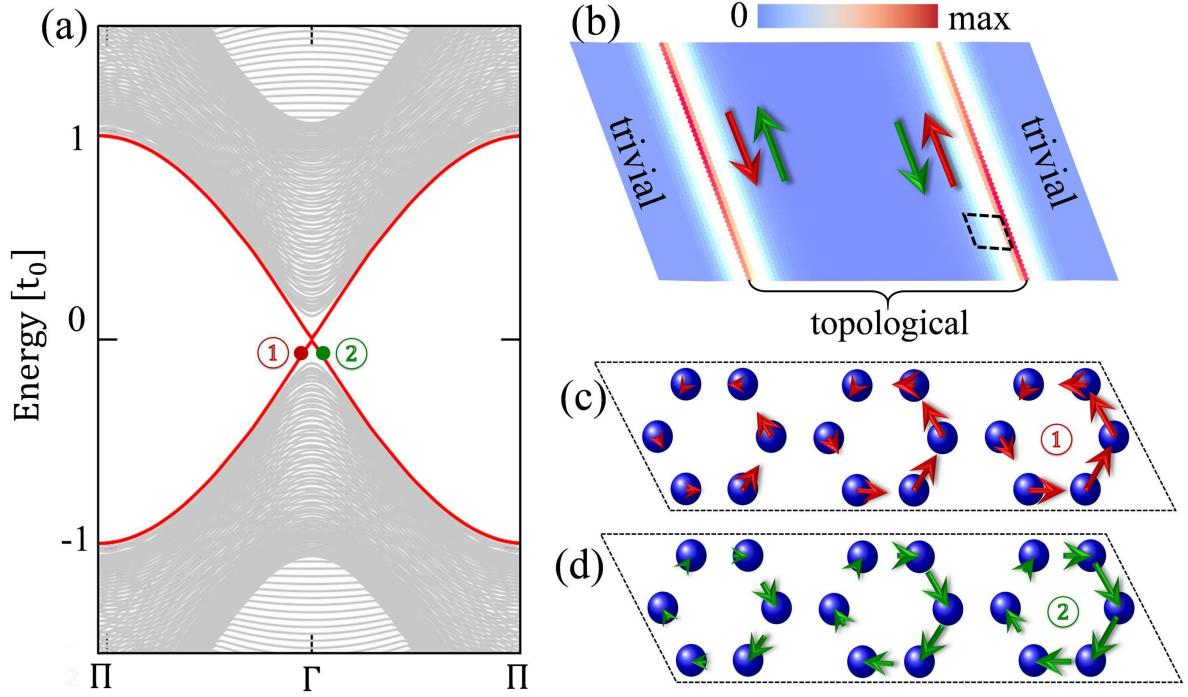


Figure 3.5: (a) Band dispersion of a ribbon system of 36 hexagons with $t_1 = 1.1t_0$ cladded from both sides by 10 hexagons with $t_1 = 0.9t_0$. (b) Real-space distribution of the in-gap states associated with the red solid dispersion curves in (a). (c) and (d) Real-space distributions of current densities in pseudospin up and down channels at the momenta indicated by the red and green dots 1 and 2 in (a) within the rhombic area sketched by dashed line in (b); the excess currents in pseudospin up and down channels are indicated by red and green arrows in (b).

3.5 Topological edge states and associated conductances

3.5.1 Helical edge states

We consider a ribbon of hexagonal unit cells of $t_1 = 1.1t_0$ with its two edges cladded by hexagonal unit cells of $t_1 = 0.9t_0$. As can be seen in Fig. 3.5(a), additional states appear in the bulk gap as indicated by the red solid curves carrying double degeneracy. Plotting the spatial distribution of the corresponding wave functions, we find that the in-gap states are localized at the two interfaces between topological and trivial regions [see Fig. 3.5(b)]. As displayed in Fig. 3.5(c) [(d)], there is an excess upward (downward) edge current in the pseudospin-up (-down) channel associated with the state indicated by the red (green) dot in Fig. 3.5(a).

3.5.2 Six-terminal Hall and longitudinal conductances

At the interface between topological and trivial regimes, the crystal symmetry is reduced from C_6 to C_2 , which breaks the pseudo-TR symmetry in contrast to the real TR symmetry. As the result, a mini gap of $\sim 0.01t_0$ [unnoticeable in the scale of Fig. 3.5(a)] opens in the edge states at the Γ point due to the coupling between two pseudospin channels. In order to quantitatively check possible backscatterings caused by this mini gap, we perform calculations on the longitudinal and Hall conductances

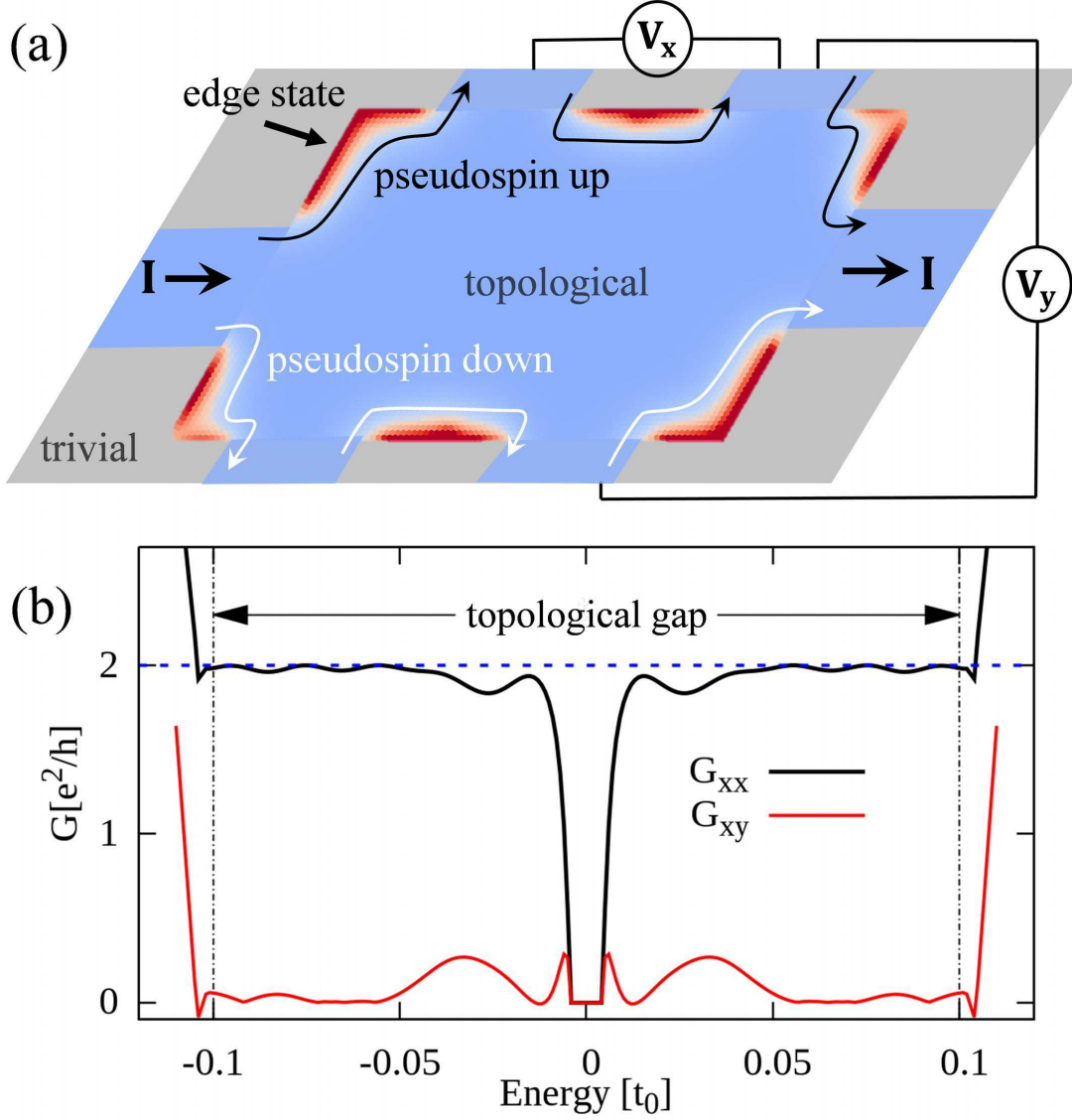


Figure 3.6: (a) Schematic configuration of a six-terminal Hall bar where a topological sample (light blue region) with $t_1 = 1.1t_0$ is embedded in a trivial environment (gray region) with $t_1 = 0.9t_0$. The size of topological scattering region is $240a_0 \times 120a_0$, and the width of each semi-infinite lead is $40a_0$. The injected current flows along the edges of topological sample as indicated by the red parts between electrodes. (b) Longitudinal and Hall conductances of the Hall bar as a function of energy of incident electrons. The on-site energy is taken $\varepsilon_0 = 0$. A rhombic topological sample is taken for ease of calculation.

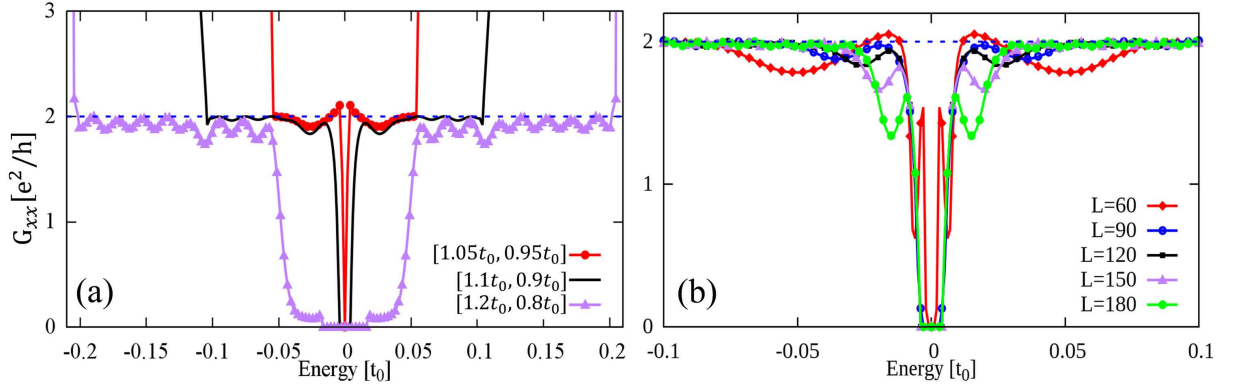


Figure 3.7: Longitudinal conductance G_{xx} of the topological sample given in Fig. 3.6 (a) as a function of the energy of injected electrons: (a) for several typical values of inter-hexagon hopping integrals $[1.05t_0, 0.95t_0]$, $[1.1t_0, 0.9t_0]$ and $[1.2t_0, 0.8t_0]$, where the first (second) inside bracket is for the topological (trivial) region; (b) with several typical system sizes $2L\vec{a}_1 \times L\vec{a}_2$, where the width of the electrodes is fixed at $40a_0$ and the inter-hexagon hopping integral is fixed at $t_1 = 1.1t_0$ and $t_1 = 0.9t_0$ for the topological and trivial regions respectively.

based on a Hall bar system as sketched in Fig. 3.6(a). It is clear that the current I injected from the left electrode divides itself into two branches according to the pseudospin states, namely pseudospin up (down) electrons can flow only in the upper (lower) edge of the Hall bar. By matching wave functions at the interfaces between the six semi-infinite electrodes and the topological scattering region [72, 73], one can evaluate the transmissions of plane waves scattered among all the six leads, and then the longitudinal and Hall conductances, $G_{xx} = \rho_{xx}/(\rho_{xx}^2 + \rho_{xy}^2)$ and $G_{xy} = \rho_{xy}/(\rho_{xx}^2 + \rho_{xy}^2)$ respectively, by the Landauer-Büttiker formalism [74], where ρ_{xx} and ρ_{xy} are the longitudinal and transverse resistances, respectively. Similar to the case of QSHE with magnetic impurities [75], the values of conductivity in the present system deviate from the quantized ones when the Fermi level falls in the mini gap of $\sim 0.01t_0$ as shown in Fig. 3.6(b). It is noticed, however, that both G_{xx} and G_{xy} heal quickly after several periods of oscillations that come from interferences between the two pseudospin channels. It is emphasized that almost perfectly quantized conductances $G_{xx} = 2e^2/h$ and $G_{xy} = 0$ [10, 26] are achieved for the Fermi level beyond $0.04t_0$ up to the bulk gap edge at $0.1t_0$, where the edge states with almost perfect linear dispersions hardly feel the existence of the mini gap and essentially no appreciable backscattering exists. On the other hand, if the inter-hexagon hopping energy is put far away from the intra-hexagon one in topological and/or trivial regimes, edge states may hardly be noticed [76].

Now we discuss the hopping-energy dependence of the longitudinal conductance. The size of scattering region is same as in Fig. 3.6(a) and fixed for all cases. As displayed in Fig. 3.7(a), G_{xx} saturates to the quantized value $2e^2/h$ as expected for a \mathbb{Z}_2 topological state for all the cases with $t_1 = 1.05t_0, 1.1t_0$ and $1.2t_0$ in the topological region (whereas $0.95t_0, 0.9t_0$ and $0.8t_0$ in the trivial region correspondingly) when the Fermi level is set away from the mini gaps, accompanied by oscillations due to interferences between the two pseudospin channels.

We then discuss the sample-size dependence of the longitudinal conductance. We fix inter-hexagon hopping integrals at $1.1t_0$ and $0.9t_0$ in the topological and trivial regions respectively. As displayed in Fig. 3.7(b), G_{xx} saturates in all cases to the quantized value $2e^2/h$ when the Fermi level is shifted away from the mini gap. The topological edge transports remain unchanged when the size of the topological

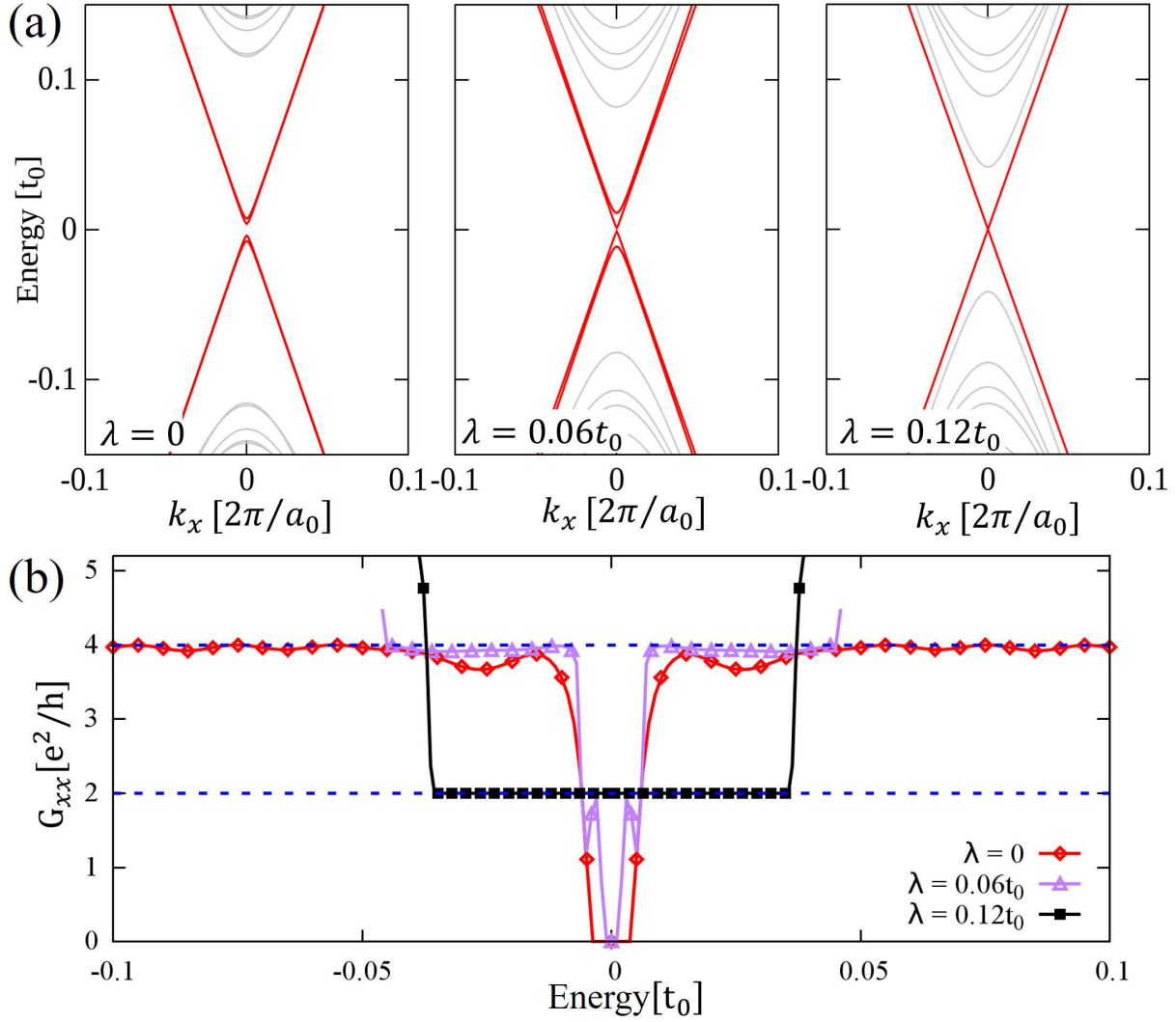


Figure 3.8: (a) Dispersion relations and (b) longitudinal conductances of the topological system same as that given in Fig. 3.6(a) except that finite SOC is included.

region becomes large.

3.6 Real spin, spin-orbit coupling and QSHE

3.6.1 Low-energy model with SOC

In addition to the pseudospin, the *real* spin degree of freedom also contributes to transport properties. In absence of the real SOC, the results presented in Fig. 3.6 remain exactly the same, with an additional double degeneracy due to the two spin channels and thus $G_{xx} = 4e^2/h$.

An intrinsic SOC is induced when next-nearest-neighbor hoppings in honeycomb lattice are taken

into account [7, 8]. The tight-binding model for the SOC is

$$\mathcal{H}_{\text{SOC}} = \frac{\lambda}{3\sqrt{3}} \sum_{\langle\langle i,j \rangle\rangle, \sigma\sigma'} v_{ij} (a_{i\sigma}^\dagger s_{\sigma\sigma'}^z a_{j\sigma'} + b_{i\sigma}^\dagger s_{\sigma\sigma'}^z b_{j\sigma'}), \quad (3.14)$$

where λ is the strength of SOC, $a_{i\sigma}$ and $b_{i\sigma}$ annihilate electrons at the lattice site i with spin σ for sublattice A and B respectively, $v_{ij} = \pm 1$ for clockwise (anti-clockwise) hopping [see figure 1.3], s^z is the Pauli matrix, $\langle\langle \cdot, \cdot \rangle\rangle$ represent next-nearest-neighbor hopping integrals. By simple Fourier transformation, the low-energy Hamiltonian around the Γ point up to the lowest order of \mathbf{k} in Eq. (3.12) is then modified to

$$\tilde{H}(\mathbf{k}) = \begin{pmatrix} \tilde{H}_+(\mathbf{k}) & 0 \\ 0 & \tilde{H}_-(\mathbf{k}) \end{pmatrix} \quad (3.15)$$

with

$$\tilde{H}_\pm(\mathbf{k}) = \begin{pmatrix} -\delta t \mp \nu\lambda + \frac{1}{2}a_0^2 t_1 \mathbf{k}^2 & \frac{i}{2}a_0 t_1 k_\pm \\ -\frac{i}{2}a_0 t_1 k_\mp & \delta t \pm \nu\lambda - \frac{1}{2}a_0^2 t_1 \mathbf{k}^2 \end{pmatrix},$$

where $\nu = 1$ and -1 stand for spin-up and -down states respectively. Therefore, in the spin-up channel SOC enhances (suppresses) the topological gap in the pseudospin-up (-down) channel presuming $\lambda > 0$ [see the left and central panels of Fig. 3.8(a)]. As far as $\lambda < \delta t$, the system remains the \mathbb{Z}_2 topological state associated with the pseudospin, where electrons with up pseudospin and down pseudospin counter propagate at edges, both carrying on up and down spins. The longitudinal conductance G_{xx} saturates to $4e^2/h$ as displayed in Fig. 3.8(b).

When SOC is increased to $\lambda = \delta t$, the pseudospin-down (-up) channel with up (down) spin is driven into a semi-metallic state with zero band gap and the Dirac dispersion appears at the Γ point. When SOC goes beyond δt , this Dirac dispersion opens a gap accompanied by a topological phase transition. The system now takes a QSHE state where at edges electrons with up spin and pseudospin propagate oppositely to electrons with down spin and pseudospin. Evaluating the longitudinal conductance, one finds that G_{xx} is quantized exactly to $2e^2/h$ [see Fig. 3.8(b)], and as shown in the right panel of Fig. 3.8(a) there is no mini gap in the edge states, as protected by *real* TR symmetry [7, 8].

3.7 Possible experimental realizations

Much effort has been devoted towards realizing the Dirac-like energy dispersion in artificial honeycomb lattices [77], ranging from optical lattices [78, 79] to 2D electron gases modulated by periodic potentials [80–82]. All these systems provide promising platforms for realizing topological properties by detuning effective hopping energy among nearest-neighbor sites either by modulating muffin-tin potentials or bond lengths periodically. To be specific, here we focus on how to achieve a topological state on the Cu [111] surface modulated by triangular gates of carbon monoxide (CO) molecules [80]. When extra CO molecules are placed at specific positions over the pristine molecular graphene, the bonds of the hexagons surrounding them are elongated since the CO clusters enhance local repulsive potentials and push electrons away from them, which reduces the corresponding electron hopping energies [82]. It is extremely interesting from the present point of view that Kekulé hopping textures have already been achieved in experiments [80]. We propose to place extra CO atoms in the pattern displayed in Fig. 3.9(a), where the intra-hexagon hopping energy t_0 (green thin bonds) surrounding the

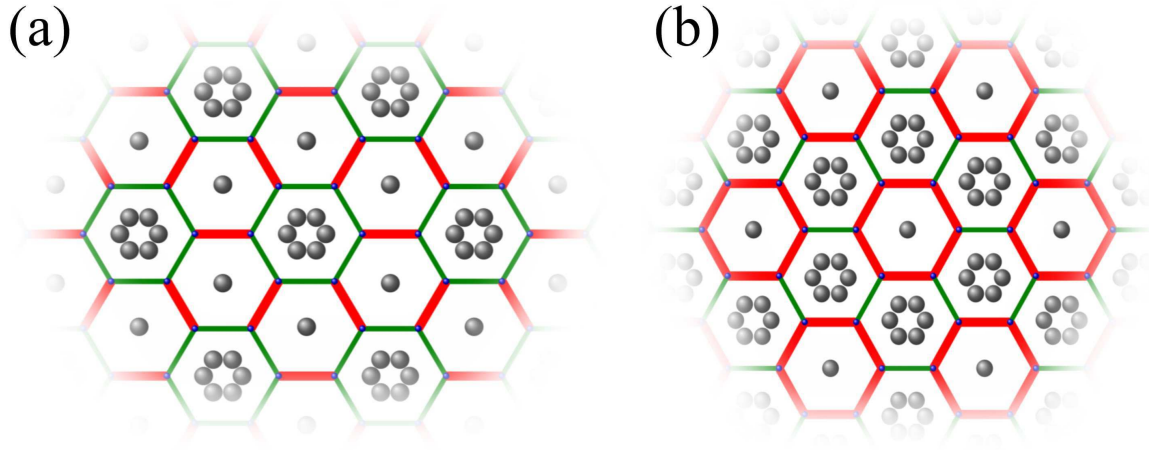


Figure 3.9: Molecular graphene realized by decorating the Cu [111] surface with a triangular lattice of CO molecules: (a) $t_1 > t_0$ generating topological state, (b) $t_1 < t_0$ for trivial state. Gray balls are CO molecules decorated by STM techniques, and red thick bonds are shorter than green thin ones which generates the Kekulé hopping textures.

CO clusters is reduced and the inter-hexagon hopping energy t_1 (red thick bonds) is enhanced relatively. According to the above discussions, the system displayed in Fig. 3.9(a) with $t_1 > t_0$ should take a topological state. The Kekulé hopping texture in Fig. 3.9(b), dual to that shown in Fig. 3.9(a), was realized in experiments [80], where the system takes a topologically trivial state because $t_1 < t_0$. Recently, it is predicted by first-principle calculations that $\text{In}_2\text{Te}_2/\text{Graphene}$ bilayers can also support Kekulé hopping textures [83], which can be another promising platform for realizing the topological state addressed in the present work.

The underlying idea of the present scheme for achieving the \mathbb{Z}_2 topological state is to create artificial orbitals carrying on opposite orbital angular momenta and parities with respect to spatial inversion symmetry, and to induce a band inversion between them by introducing a Kekulé hopping texture on honeycomb lattice. In the sense that it does not require SOC, the present state may be understood as a quantum *orbital* Hall effect. The topological properties can also be extended to photonic crystals [13], cold atoms, and even phonon systems where sound waves form band due to periodic configurations elastic materials.

Kekulé textures of hopping integrals in honeycomb lattice were discussed in a previous work where states with fractionalized charges can be realized [84]. In order to introduce vortices in honeycomb lattice, the inter-hexagon hopping integrals were put complex involving nontrivial phase factors and position dependent generally, whereas they are real constant in the present work.

3.8 Conclusion

In this chapter, we explore possible topological properties in honeycomb lattice by introducing a texture in hopping energy between nearest-neighboring sites. We take a hexagonal primitive unit cell and view the honeycomb lattice as a triangle lattice of hexagons [see the dashed red line in Fig. 3.2(a)]. When the real-valued inter-hexagon hopping t_1 is tuned to be larger than the intra-hexagon one t_0 , a topological gap is opened at the Γ point accompanied by a band inversion between orbitals with opposite

spatial parities accommodated on hexagons [see Fig. 3.2(b)]. A pseudo-TR symmetry associated with a pseudospin degree of freedom and Kramers doubling in the emergent orbitals are revealed based on the C_6 point group symmetry, which generates the \mathbb{Z}_2 topology. For experimental implementations, we discuss that, along with many other possibilities, the *molecular graphene* realized by placing carbon monoxides (CO) periodically on Cu [111] surface is a very promising platform to realize the present idea, where the hopping texture can be controlled by adding extra CO molecules.

Novel Quantum Anomalous Hall Effect in Perovskites Materials

4.1 Introduction of quantum anomalous Hall effect

Breaking the time-reversal symmetry can drive topological insulators into the quantum anomalous Hall effect (QAHE) [6]. There are two categories of QAHE classified by the spin Chern number [59, 60], which equals $C_s = C_\uparrow - C_\downarrow$ with $C_{\uparrow/\downarrow}$ the Chern numbers for the spin-up/spin-down channel respectively. One subclass of QAHE is characterized by a vanishing spin Chern number. The Cr-doped Bi_2Se_3 thin film [18, 85, 86] and heavy atom decorated graphene [65, 87] belong to this class, where the topological band gap is opened by the hybridizations between the spin-up and -down channels. In the former case, a 3D topological insulator thin film Bi_2Se_3 [39, 40] was considered, where there is a strong interaction between the top and bottom surfaces. A ferromagnetic order is induced by the doped Cr atoms. The Hamiltonian is [85]

$$H_{\text{QAHE}} = H_{\text{TI}} + H_{\text{Zeeman}} = \begin{pmatrix} M & v_f k_- & m_k & 0 \\ v_f k_+ & -M & 0 & m_k \\ m_k & 0 & M & -v_f k_- \\ 0 & m_k & -v_f k_+ & -M \end{pmatrix} \quad (4.1)$$

on the basis $[|t \uparrow\rangle, |t \downarrow\rangle, |b \uparrow\rangle, |b \downarrow\rangle]$, where $t(b)$ is the top (bottom) surface, $m_k = m_0 + B\mathbf{k}^2$ is the interaction between the top and bottom surfaces, v_f is the Fermi velocity, M is the Zeeman field, and $k_\pm = k_x \pm ik_y$. An unitary matrix transforms

$$\mathcal{U} = \frac{1}{\sqrt{2}} \begin{pmatrix} 1 & 0 & 0 & -1 \\ 0 & 1 & 1 & 0 \\ 1 & 0 & 0 & 1 \\ 0 & -1 & 1 & 0 \end{pmatrix} \quad (4.2)$$

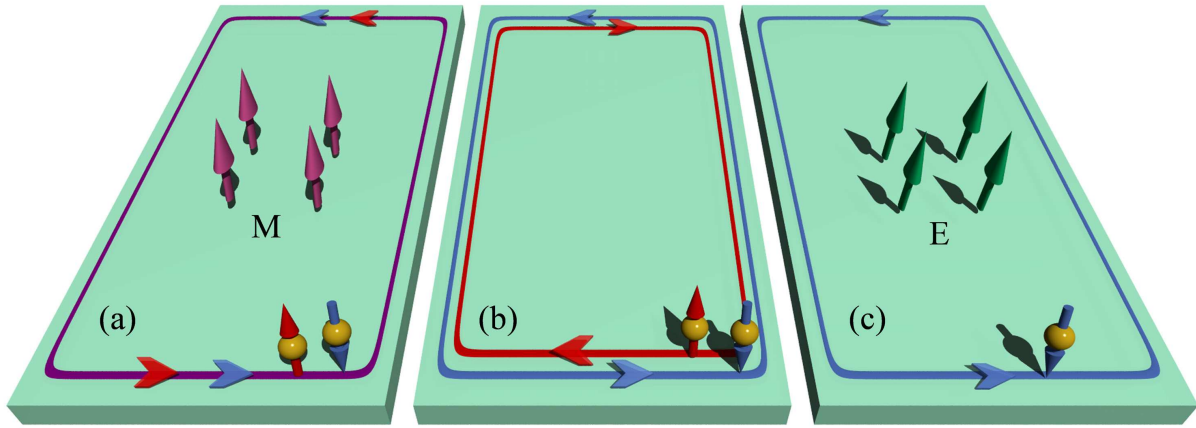


Figure 4.1: Schematic distributions of topological edge states for (a) conventional QAHE with $C_c = 1$ and $C_s = 0$; (b) QSHE with $C_c = 0$ and $C_s = 2$ and (c) novel QAHE with $C_c = 1$ and $C_s = 1$. Arrows are directions of edge current. Red and blue curves are for spin-up and -down channels respectively, M and E are ferromagnetic exchange field and electric field respectively.

the Eq. (4.1) into a block-diagonal form

$$\tilde{\mathcal{H}}_{\text{QAHE}} = \begin{pmatrix} \mathcal{H}_1 & 0 \\ 0 & \mathcal{H}_2 \end{pmatrix} \quad (4.3)$$

with

$$\begin{aligned} \mathcal{H}_1 &= \begin{pmatrix} m_0 + M + B\mathbf{k}^2 & v_f k_- \\ v_f k_+ & -m_0 - M - B\mathbf{k}^2 \end{pmatrix}, \\ \mathcal{H}_2 &= \begin{pmatrix} m_0 - M + B\mathbf{k}^2 & v_f k_+ \\ v_f k_- & -m_0 + M - B\mathbf{k}^2 \end{pmatrix} \end{aligned} \quad (4.4)$$

on the basis $\left[\frac{|t\uparrow\rangle + |b\uparrow\rangle}{\sqrt{2}}, \frac{|t\downarrow\rangle - |b\downarrow\rangle}{\sqrt{2}}, \frac{|t\downarrow\rangle + |b\downarrow\rangle}{\sqrt{2}}, \frac{|t\uparrow\rangle - |b\uparrow\rangle}{\sqrt{2}} \right]$. By tuning the Zeeman field M to satisfy

$$\begin{cases} (m_0 + M)B < 0 \\ (m_0 - M)B > 0 \end{cases},$$

the two parabolic bands in the upper diagonal part \mathcal{H}_1 can meet at two finite \mathbf{k} points if $v_f = 0$, forming two Dirac points, as shown in figure 1.5. For a nonzero v_f , the hybridizations between the first two modes open a global band gap, which generates a topological charge $C = 1$ [see figure 1.5(b)]. This is known as band inversion mechanism [10]. Since there is no band inversion in the \mathcal{H}_2 due to $(m_0 - M)B > 0$, the lower diagonal part is topologically trivial. Similarly, one can also let $(m_0 + M)B > 0$ and $(m_0 - M)B < 0$ in order to realize a QAHE only in the lower diagonal part \mathcal{H}_2 . It should be noticed that topological gaps in both the upper-diagonal or lower-diagonal parts are opened by hybridizations of the spin-up and -down channels, which eliminates the spin information of topological edge states (see figure 4.1).

The other subclass of QAHE has a nonzero spin Chern number. One representative material is the Mn-doped HgTe [88], where s -type electrons of Hg and p -type holes of Te experience opposite

g -factors when they couples with d electrons of Mn. The opposite exchange fields felt by the s and p orbitals enlarge the energy gap in one spin channel, close and then reopen the energy gap in the other spin channel, which induces the nontrivial topology in the latter spin channel due to the band inversion mechanism [10, 88], for a large enough g -factor. However, its experimental realization turns out to be difficult due to the paramagnetic state of Mn spins. Two other materials are proposed to realize the QAHE with nonzero spin Chern numbers in honeycomb lattice, a silicene sheet sandwiched by two ferromagnets with magnetization directions aligned anti-parallelly [89], and the perovskite material LaCrO_3 grown along the $[111]$ direction with Cr atoms replaced by Ag or Au in one atomic layer [17]. In both systems, in addition to the anti-ferromagnetic (AFM) exchange field and spin-orbit coupling (SOC), a strong electric field is required to break the inversion symmetry in order to realize the QAHE, as displayed in figure 4.1(c). For the former one, the weak SOC of silicon limits the novel QAHE to low temperatures, while for the latter one, growth of the perovskite material along the $[111]$ direction seems to be difficult.

In the this chapter, we propose a new material to realize the second subclass of QAHE without any extrinsic operation and easy to synthesize. It is based on LaCrO_3 grown along the $[001]$ direction, where we insert one atomic layer of an inverse-perovskite material Sr_3PbO [90, 91]. With first-principles calculations, we reveal that there is a band inversion at the Γ point between the d orbital of Cr and the p orbital of Pb in the spin-up channel induced by SOC, whereas the spin-down bands are pushed far away from the Fermi level by the AFM exchange field. Constructing the low-energy effective Hamiltonian, we explicitly show that the system is characterized by simultaneous nonzero charge and spin Chern numbers. Projecting the bands near the Fermi level onto the subspace composed of the spin-up d and p orbitals by maximally localized Wannier functions [92], we confirm that a spin-polarized and non-dissipative current flows on the edge of a finite sample. Since these two materials are stable in bulk and match each other with only small lattice distortions, the composite material is expected easy to synthesize.

4.2 Novel QAHE in square lattice

4.2.1 First-principles calculations

The parent material LaCrO_3 exhibits the perovskite structure with formula ABO_3 , where oxygen atoms form an octahedron surrounding the B atom. It is a well-known Mott insulator with a large energy gap ~ 3 eV, carrying a G-type AFM order, where the spin moment of any Cr aligns opposite to all its neighbors. On the other hand, the material Sr_3PbO shows the inverse-perovskite structure with formula A_3BO , where the A atoms form an octahedron surrounding oxygen. It was revealed recently that there is a topological band gap in bulk Sr_3PbO [93, 94]. We notice that the \vec{a} - \vec{b} plane lattice constant is 3.88\AA for LaCrO_3 , and 5.15\AA for Sr_3PbO , different from each other by a factor close to $\sqrt{2}$. Therefore, with a $\pi/4$ rotation around the common \vec{c} axis, these two materials match each other quite well [see Figs. 4.2(a) and (b)]. At the interface the oxygen of Sr_3PbO completes the CrO_6 octahedron of the perovskite structure [see Fig. 4.2(b)], which minimizes the distortion to the two materials when grown together. As shown in Fig. 4.2(b) zoom-in at the interface, there are two types of Cr atom in each CrO_2 unit cell, where Cr1 sits at the corners of the square and above the Pb atom in the \vec{c} axis, whereas Cr2 sits at the center of square and above the oxygen.

We have performed first-principles calculations by using density functional theory (DFT) imple-

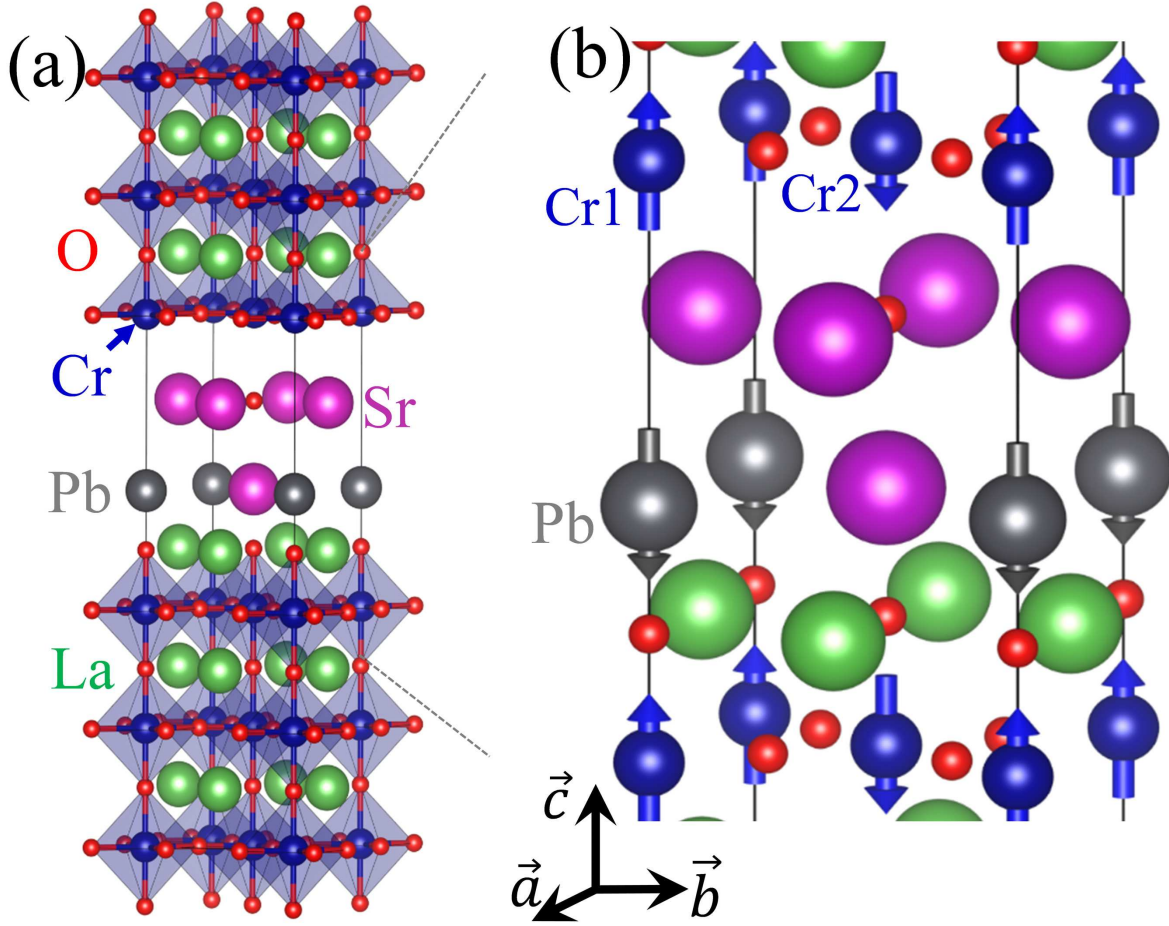


Figure 4.2: (a) Crystal structure of bulk LaCrO_3 grown along the $[001]$ direction with one atomic layer replaced by Sr_3PbO . (b) Enlarged interface between LaCrO_3 and Sr_3PbO with grey and blue arrows representing spin moments on Pb and Cr sites, respectively. \vec{a} , \vec{b} and \vec{c} are lattice vectors.

mented in Vienna *Ab-initio* Simulation Package (VASP) [95], which uses projected augmented wave (PAW) method [96, 97]. The exchange correlation potential is described by the generalized gradient approximation (GGA) of Perdew-Burke-Ernzerhof (PBE) type [98]. The cut-off energy of the plane waves is chosen to be 500 eV. The Brillouin zone is meshed into $10 \times 10 \times 1$ grids using Monkhorst-Pack method. The Hubbard-U term is included for $\text{Cr-}3d$ electrons with $U = 5.0$ eV and $J = 0.5$ eV [99] by using Dudarev's method. For the lattice structure, we take $a = b = 5.48 \text{ \AA}$ ($= \sqrt{2} \times 3.88 \text{ \AA}$) and $c_{\text{LaCrO}} = 3.88 \text{ \AA}$. The height of the inserted Sr_3PbO layer is determined by a relaxation process to achieve the minimal energy: $c_{\text{SrPbO}} = 5.46 \text{ \AA}$, the distance from the Pb atom to the Cr atom just above it (that to the Cr atom below it is c_{LaCrO}). Afterwards, the positions of atoms are determined by a second relaxation process with all lattice constants fixed. In both processes, the criterion on forces between atoms is set to below 0.01 eV/\AA .

We calculate the band structure of the hybrid material with zero SOC and find a band gap 0.18 eV. As shown in Fig. 4.3(a), the topmost valence band is occupied by the spin-up $p_{\pm}(= p_x \pm i p_y)$ orbitals of Pb , and the lowest conduction band is contributed by the spin-up d_{z^2} of Cr1 . The reason for this band

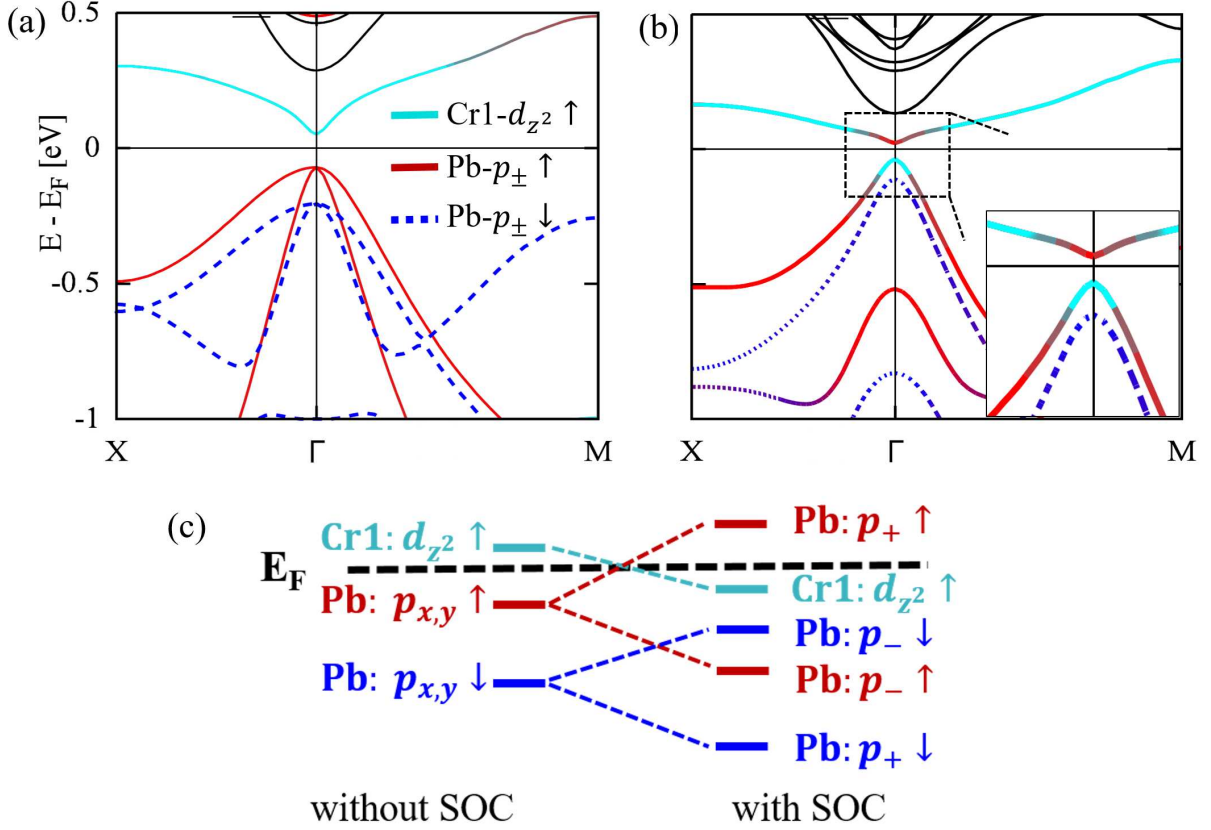


Figure 4.3: Band structure of the supercell shown in Fig. 4.2 without (a) and with (b) SOC. Green, red and blue curves are for Cr1- $d_{z^2}^{\uparrow}$, Pb- p_{\pm}^{\uparrow} and Pb- p_{\pm}^{\downarrow} orbitals, respectively. Other colors indicate their hybridizations. (c) Schematic band evolution of Pb- $p_{x,y}$ and Cr- d_{z^2} at the Γ point caused by SOC.

arrangement is that the Cr1 atom does not live in a closed octahedron due to the absence of an oxygen in the corner of Sr_2O layer as shown in Fig. 4.2(b), which weakens the crystal field splitting and lowers the energy of the unoccupied Cr1- d_{z^2} band, whereas the Cr2 shares one oxygen with Sr_3PbO , thus is closed by a complete oxygen octahedron, which keeps its d_{z^2} far away from the Fermi level. Therefore, only the spin-up Cr1- d_{z^2} band appears just above the Fermi level, in contrast to the original Mott insulator. Meanwhile, the Pb acquires a magnetic moment $0.19\mu_B$ polarized downwards [see Fig. 4.2(b)], which matches the overall AFM G-type order of LaCrO_3 and splits the spin-up and spin-down p orbitals of Pb [see Fig. 4.3(a)]. The AFM exchange field is essential for inducing the novel QAHE. As shown in figure 4.4(a), the spin-up channel is pushed towards the Fermi level while the spin-down one is driven far away from the Fermi level by the AFM exchange field. When the AFM field is strong enough, a band inversion happens at the Γ , which can possibly induce a QAHE in the spin-up channel [see figure 4.4(b)]. Similarly, the novel QAHE can also be generated from a QSHE by including strong AFM exchange field to push one spin-channel away from the Fermi level, as shown in figure 4.4(c). The total magnetic moment in the present system is compensated to zero, distinct from the Cr-doped Bi_2Se_3 [18, 85].

The band structure of the material is then calculated with SOC turned on, which lifts the degeneracy between the p_+ and p_- bands in both spin channels. Remarkably, the strong SOC of the heavy element

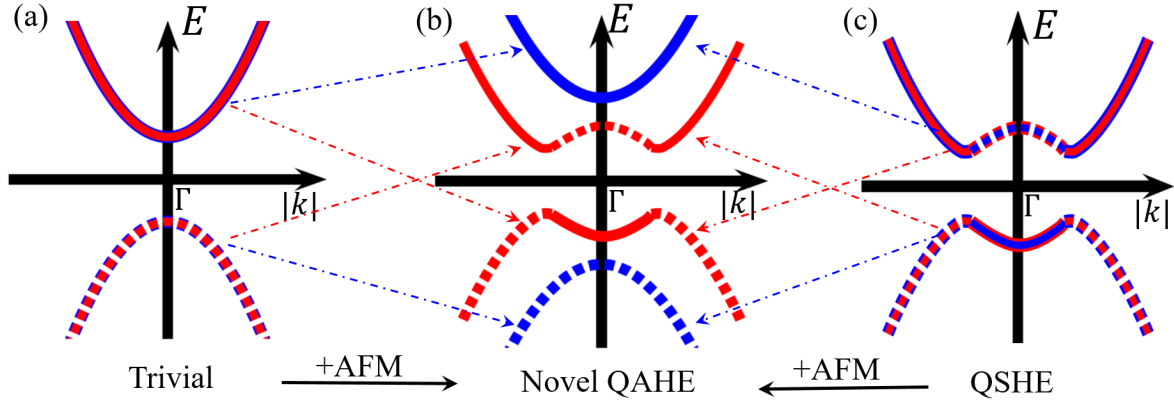


Figure 4.4: Schematic plot for realizing novel QAHE with AFM exchange field from (a) a trivial state and (c) a QSHE. (b) Novel QAHE with simultaneous charge and spin Chern numbers: only one spin channel is topological. Dashed and solid curves are for orbitals with odd and even spatial parities respectively. Red and blue curves are for spin-up and spin-down channels respectively.

Pb pushes the p_+ orbital with up spin even above the Fermi energy E_F around the Γ point as displayed in Figs. 4.3(b) and (c). The Cr1- d_{z^2} orbital with up spin then has to sink across the Fermi level partially in order to maintain the charge neutrality of the system, which causes a band inversion between the p and d orbitals around the Γ point, as shown in Fig. 4.3(b). An energy gap of 59 meV is observed according to the first-principles calculations.

4.2.2 Effective low-energy model

We now derive an effective low-energy $\mathbf{k} \cdot \mathbf{p}$ Hamiltonian which describes the topological property of the system. Noticing that the topological band gap is opened by hybridizations between the spin-up p_+ orbital of Pb and the spin-up d_{z^2} orbital of Cr1, it is reasonable to take these two bands as a basis to construct a 2×2 Hamiltonian. For simplicity, we denote the two orbitals as $\Gamma_1 = d_{z^2}^\uparrow$ and $\Gamma_2 = p_+^\uparrow$. The effective $\mathbf{k} \cdot \mathbf{p}$ Hamiltonian around the Γ point is

$$H(\mathbf{k}) = H_0 + H' \quad (4.5)$$

on the basis $[\Gamma_1, \Gamma_2]$, where

$$H_0 = \begin{pmatrix} \epsilon_1 + \gamma_1 \mathbf{k}^2 & 0 \\ 0 & \epsilon_2 + \gamma_2 \mathbf{k}^2 \end{pmatrix} \quad (4.6)$$

and $H' = \mathbf{k} \cdot \mathbf{p} = (k_- P_+ + k_+ P_-)/2$ is the perturbation term with $k_\pm = k_x \pm i k_y$ and $P_\pm = P_x \pm i P_y$ ($P_{x/y}$ is the momentum operator in the x/y direction). Since the crystal is symmetric under the C_4 rotation around the \vec{c} axis, H' must be invariant under the $C_4 = e^{-i \frac{2\pi}{4} J_z}$ transformation, where J_z is the z -component of the total angular momentum. The symmetry constraint allows us to determine nonzero entries of H' . It is easy to check that $C_4 \Gamma_1 = e^{-i \frac{\pi}{4}} \Gamma_1$ and $C_4 \Gamma_2 = e^{-i \frac{3\pi}{4}} \Gamma_2$ because $J_z = 1/2$ and

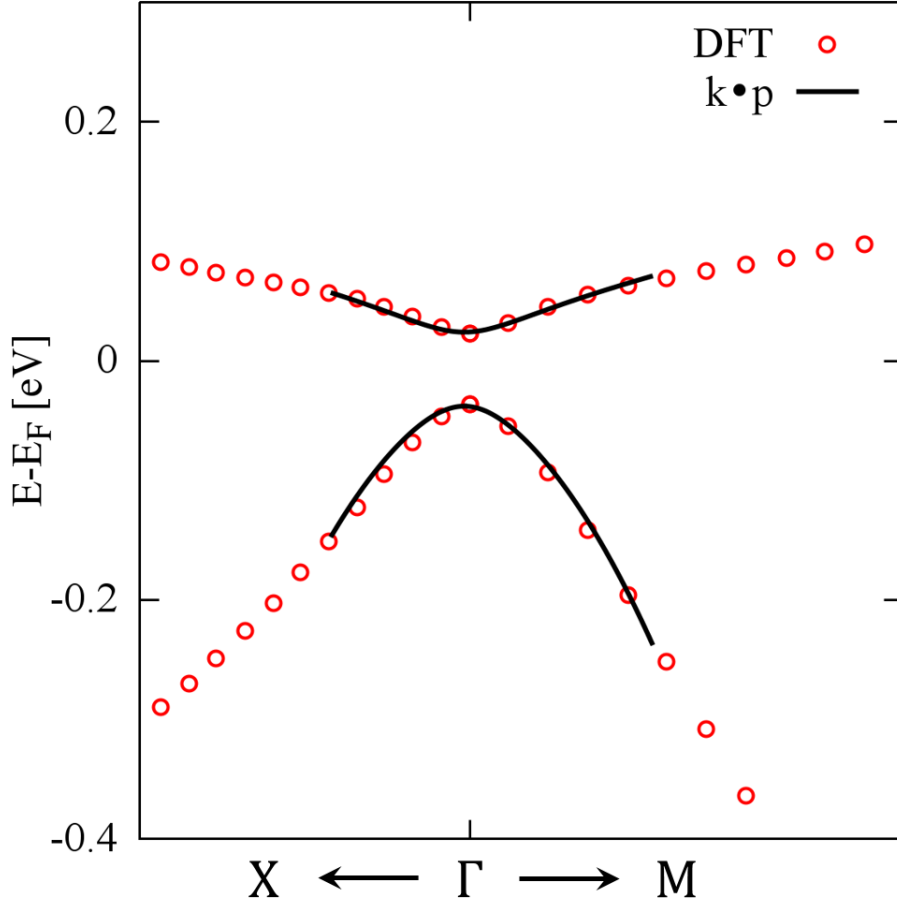


Figure 4.5: Energy dispersion around the Γ point fitted by the 2×2 $\mathbf{k} \cdot \mathbf{p}$ Hamiltonian (4.8) on the basis $[d_{z^2}^\dagger, p_+^\dagger]$. The fitted curves collapse with the DFT results within the region $|k_x| \leq 0.08 \frac{2\pi}{a}$ and $|k_y| \leq 0.08 \frac{2\pi}{b}$, where a and b are lattice constants given in text.

$3/2$ for Γ_1 and Γ_2 respectively. Since

$$\begin{aligned}
 \langle \Gamma_1 | P_+ | \Gamma_2 \rangle &= \langle \Gamma_1 | C_4^\dagger C_4 P_+ C_4^\dagger C_4 | \Gamma_2 \rangle \\
 &= \langle \Gamma_1 | e^{i\frac{\pi}{4}} e^{-i\frac{\pi}{2}} P_+ e^{-i\frac{3\pi}{4}} | \Gamma_2 \rangle \\
 &= -\langle \Gamma_1 | P_+ | \Gamma_2 \rangle,
 \end{aligned} \tag{4.7}$$

$\langle \Gamma_1 | k_- P_+ | \Gamma_2 \rangle$ must vanish. Performing similar calculations for all other terms, we arrive at the Hamiltonian respecting the crystal symmetry

$$H(\mathbf{k}) = (\epsilon_0 + \gamma_0 k^2) \mathbb{I}_{2 \times 2} + \begin{pmatrix} \epsilon + \gamma \mathbf{k}^2 & \alpha k_+ \\ \alpha^* k_- & -\epsilon - \gamma \mathbf{k}^2 \end{pmatrix} \tag{4.8}$$

up to the lowest orders of \mathbf{k} , with $\epsilon_0 = (\epsilon_1 + \epsilon_2)/2$, $\epsilon = (\epsilon_1 - \epsilon_2)/2$, $\gamma_0 = (\gamma_1 + \gamma_2)/2$ and $\gamma = (\gamma_1 - \gamma_2)/2$. By fitting the energy dispersion of the effective Hamiltonian $H(\mathbf{k})$ in Eq. (4.8) against the first-principles results given in Fig. 4.3(b), we obtain the parameters as follows: $\epsilon_0 = -0.007$ eV, $\gamma_0 = -7.8$ eVÅ²,

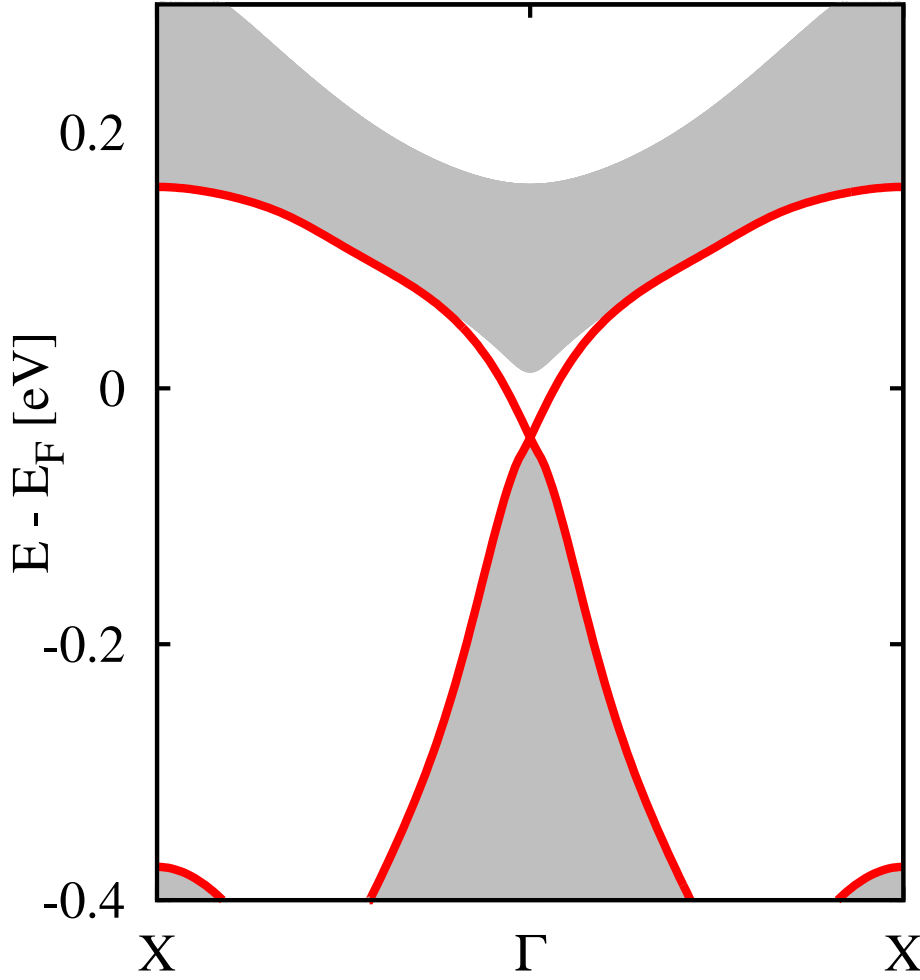


Figure 4.6: Band structure for a slab of the system shown in Fig. 4.2 based on Wannierized wavefunctions downfolded from the results of the first-principles calculations in Fig. 4.3(b). Red curves are for topological edge states in the spin-up channel, and grey ones are for bulk states.

$\epsilon = -0.031$ eV, $\gamma = 9.0$ eVÅ² and $\alpha = 1.45$ eVÅ (see Fig. 4.5). Since ϵ and γ take opposite signs, the electronic wavefunction of the spin-up channel becomes topologically nontrivial due to the band inversion mechanism with Chern number $C_{\uparrow} = 1$. Since spin-down electronic bands are kept far away from the Fermi level [see Figs. 4.3(b) and (c)], one clearly has $C_{\downarrow} = 0$. It is therefore confirmed that the system is characterized by simultaneous charge and spin Chern numbers: $C_c = C_{\uparrow} + C_{\downarrow} = 1$ and $C_s = C_{\uparrow} - C_{\downarrow} = 1$.

Liu [100] proposed a 3D spinless model for a layered square lattice with A-type AFM (intra-plane ferromagnetic and inter-plane AFM orderings). At each lattice site, there are three orbitals: s , p_x and p_y . Each layer can be driven into a QAHE in a same way as that for the Mn-doped HgTe [88]. Since every two adjacent layers have opposite magnetic moments, their chiral edge states propagate counter to each other. Therefore, the system can be viewed as a stack of quantum spin Hall insulators (see also Ref. [101]), where the combination of the time-reversal and the primitive-lattice translational symmetries is preserved. In contrast, all symmetries are broken in our system, giving rise to a Chern insulator.

4.2.3 Topological edge states

The nontrivial topology gives rise to gapless edge states in a finite sample. To illustrate this feature, we calculate the dispersion relation for a slab of the topological material with $100a$ along the \vec{a} axis and infinite along the \vec{b} axis (see Fig. 4.2). Since the bands close to the Fermi level are mainly contributed by the Pb- p_x , Pb- p_y and Cr1- d_{z^2} orbitals, it is reasonable to downfold the wavefunctions obtained by the first-principles calculations in Fig. 4.3(b) onto these three orbitals. Employing the maximally-localized Wannier functions [92], we obtain the hopping integrals within the six-dimensional subspace including the spin degree of freedom. It is then straightforward to calculate the band structure of the slab system. As shown in Fig. 4.6, a gapless edge state with up spin appears inside the bulk gap, manifesting the nontrivial topology of the present system.

4.3 Novel QAHE in honeycomb lattice

4.3.1 Tight-binding model

It has been demonstrated that intrinsic spin-orbit couplings can drive the system into a topologically nontrivial state, characterized by the Z_2 invariants [7, 8], known as quantum spin Hall effect (QSHE). We have shown that the QSHE can be driven into a novel quantum anomalous Hall effect (QAHE), characterized by simultaneous charge and spin Chern numbers, by considering an antiferromagnetic exchange field, intrinsic spin-orbit coupling and a uniform electric field perpendicular to the two-dimensional (2D) plane [17, 18]. The tight-binding Hamiltonian describing the system is

$$\begin{aligned} \mathcal{H} = & t_0 \sum_{\langle i,j \rangle, \sigma} (a_{i\sigma}^\dagger b_{j\sigma} + b_{j\sigma}^\dagger a_{i\sigma}) + \frac{\lambda}{3\sqrt{3}} \sum_{\langle\langle i,j \rangle\rangle, \sigma\sigma'} v_{ij} (a_{i\sigma}^\dagger s_{\sigma\sigma'}^z a_{j\sigma'} + b_{i\sigma}^\dagger s_{\sigma\sigma'}^z b_{j\sigma'}) \\ & + V \sum_{i\sigma} (a_{i\sigma}^\dagger a_{i\sigma} - b_{i\sigma}^\dagger b_{i\sigma}) + M \sum_{i\sigma\sigma'} (a_{i\sigma}^\dagger s_{\sigma\sigma'}^z a_{i\sigma} - b_{i\sigma}^\dagger s_{\sigma\sigma'}^z b_{i\sigma}), \end{aligned} \quad (4.9)$$

where t_0 is the nearest-neighbor hopping energy, $a_{i\sigma}$ and $b_{i\sigma}$ annihilate electrons at the lattice site i with spin σ for sublattice A and B respectively, $v_{ij} = \pm 1$ for clockwise (anti-clockwise) hopping, s^z is the Pauli matrix. λ , V and M are magnitudes of intrinsic spin-orbit coupling, staggered potential at two sublattices induced by external electric fields and AFM exchange fields. The first is for the nearest-neighbor hopping in a pristine graphene (see detailed derivations in Appendix A.1; the second term describes the intrinsic SOC with a positive coupling coefficient $\lambda > 0$ by definition [see figure 4.7(a)], which can be large for heavy elements; the third term is induced by a uniform electric potential on the buckled structure [see figure 4.7(b)], and the last term is the AFM exchange field [see figure 4.7(c)]. The chemical potential is set to zero, and all energies are measured in units of the nearest-neighbor hopping integral t_0 .

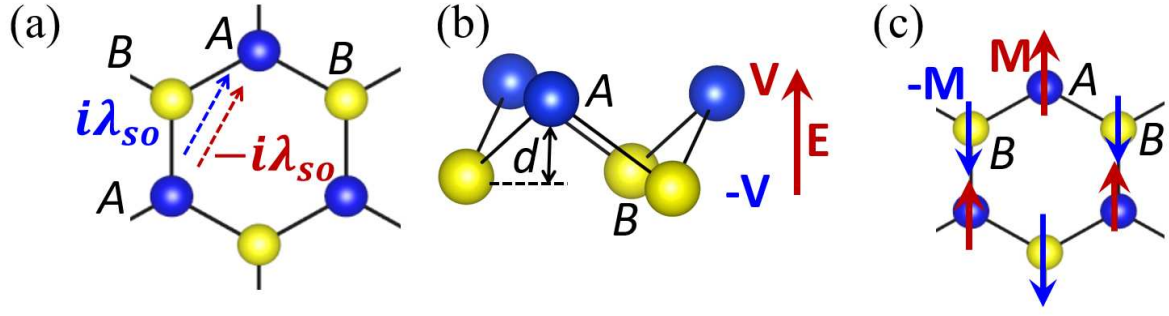


Figure 4.7: (a) Intrinsic spin-orbit coupling in honeycomb lattice. (b) Staggered potential at two sublattices induced by external electric fields perpendicular to the 2D thin film. (c) AFM exchange fields at two sublattice sites.

4.3.2 Topological phases

By straightforward Fourier transformations, we obtain the Hamiltonian (4.9) around the $K(K')$ points in the momentum space

$$\mathcal{H}(\mathbf{k}) = \begin{pmatrix} \mathcal{H}_{\uparrow} & 0 \\ 0 & \mathcal{H}_{\downarrow} \end{pmatrix} \quad (4.10)$$

with

$$\mathcal{H}_{\uparrow} = \begin{bmatrix} v\lambda + V + M & -v_f(k_x - ivk_y) \\ -v_f(k_x + ivk_y) & -v\lambda - V - M \end{bmatrix}, \quad (4.11a)$$

$$\mathcal{H}_{\downarrow} = \begin{bmatrix} -v\lambda + V - M & -v_f(k_x - ivk_y) \\ -v_f(k_x + ivk_y) & v\lambda - V + M \end{bmatrix} \quad (4.11b)$$

on the basis $[a_{\uparrow}, b_{\uparrow}, a_{\downarrow}, b_{\downarrow}]$ up to the lowest order of \mathbf{k} , where $v = \pm 1$ for the K and K' respectively, $k_{\pm} = k_x \pm ik_y$, $v_f = \sqrt{3}a_0t_0/2$ with the lattice constant $a_0 = |\vec{a}_1|$ shown in figure 1.3. We first check the \mathcal{H}_{\uparrow} . As we have shown in the chapter 1, the topological charges the K and K' points are $-\frac{1}{2}\text{sign}(\lambda + V + M)$ and $\frac{1}{2}\text{sign}(-\lambda + V + M)$ respectively. Similarly, the topological charges for the spin-down channel at the K and K' points are $-\frac{1}{2}\text{sign}(-\lambda + V - M)$ and $\frac{1}{2}\text{sign}(\lambda + V - M)$ respectively, as summarized in Table 4.1. Without lossing generality, we assume V and M are both positive. It is easy to see that when λ , V and M form a triangular relation, the Chern number for the spin-up and -down channels are

$$C_{\uparrow} = -\frac{1}{2} + \frac{1}{2} = 0, \quad C_{\downarrow} = \frac{1}{2} + \frac{1}{2} = 1,$$

indicating that we have a nonzero charge Chern number $C_c = C_{\uparrow} + C_{\downarrow} = 1$ and a nonzero spin Chern number $C_s = C_{\uparrow} - C_{\downarrow} = -1$, which can support a spin-polarized and non-dissipative edge current in a finite sample. Based on the above analysis a full phase diagram for arbitrary V and M is displayed in figure 4.8. One interesting notice from the phase diagram is that the spin polarization of the novel QAHE can be controlled by reversing the direction of external field.

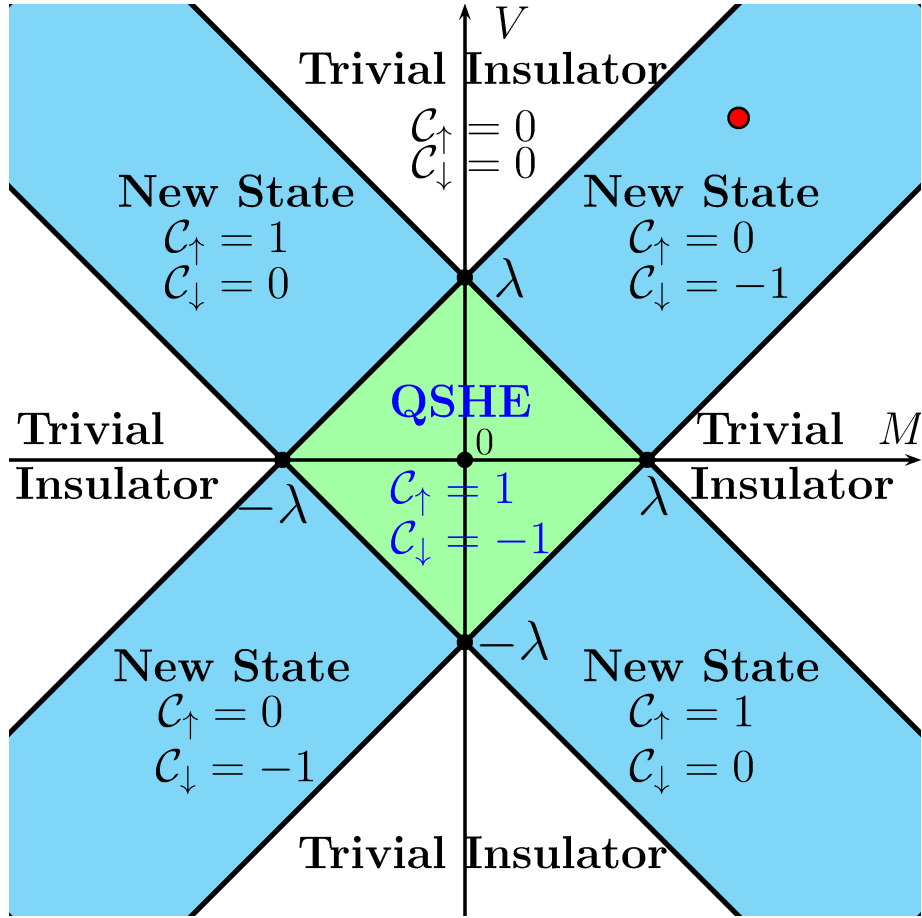


Figure 4.8: Phase diagram against staggered potential V and AFM exchange field M with a positive spin-orbit coupling λ (see figure also in Ref. [17]).

4.3.3 Spin-polarized edge state

To demonstrate the topological properties of the QAHE discussed above, we consider a Zigzag ribbon of the buckled honeycomb lattice. With a vanishing staggered electric potential $V = 0$, the spin-up and -down channels are degenerated even when a nonzero AFM is included. The reason for this degeneracy is that the net magnetic moment within a unit cell is zero. By increasing the staggered electric potential V from 0, we observe that the energy gap at the spin-up (spin-down) channel decreases (increases) at the K point, as shown in figures 4.9(a) and (b). When $V + M = \lambda$, i.e. the three fields just form a triangular relation, the band gap at the spin-up channel is completely closed [see figure 4.9(b)].

	spin up	spin down
C_K	$-\frac{1}{2}\text{sign}(\lambda + V + M)$	$-\frac{1}{2}\text{sign}(-\lambda + V - M)$
$C_{K'}$	$\frac{1}{2}\text{sign}(-\lambda + V + M)$	$\frac{1}{2}\text{sign}(\lambda + V - M)$

Table 4.1: Topological charges C at the K and K' points for the spin-up and -down channels.

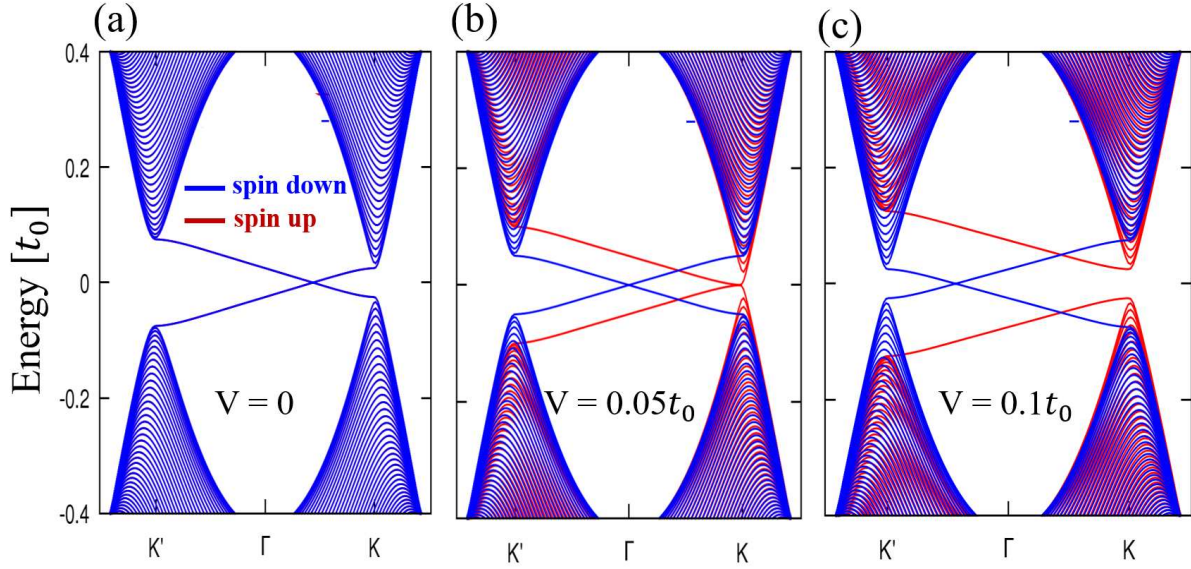


Figure 4.9: Dispersion relations for the honeycomb lattice with $\lambda = 0.1t_0$, $M = 0.05t_0$ and (a) $V = 0$, (b) $V = 0.05t_0$ and (c) $V = 0.1t_0$.

Further increasing the V field, the spin-up channel is driven into a trivial state, however, the spin-down channel remains topologically nontrivial, manifesting the novel QAHE we propose. In a finite sample, we have a non-dissipative and spin-polarized edge current.

One possible platform to host the novel QAHE is the G-type AFM Mott insulator LaCrO_3 grown along the $[111]$ direction, which forms a buckled honeycomb lattice [17, 102], as displayed in figure 4.10(a). By replacing one layer of Cr atoms with heavy Au atoms which feel the AFM exchange field established in the parent material [see figure 4.10(b)], a strong intrinsic SOC is then included. With external electric field perpendicular to the Au layer, the system can be driven into the novel QAHE with suitable staggered potential V given in Table 4.1.

4.3.4 Robustness of the novel QAHE against Rashba-type SOC

The spin \hat{s}_z conservation in QSHE can be destroyed by the Rashba-type SOC, which is inevitably aroused by inversion symmetry broken terms: interaction, disorder, asymmetric quantum confinements in experiments. It is thus meaningful to understand the effect of Rashba-type SOC on the stability of topological states, which can be identified by topological invariants of systems. Kane *et al.* [7] and Fu *et al.* [38] stated that Z_2 invariants can well characterize the QSH system with Rashba-type SOC, while spin-Chern number relating with quantized spin-Hall conductivity loses its meaning due to the non-conservation of spin quantum number \hat{s}_z . It has been suggested that one can divide the valence states into two spin subspaces \tilde{s}_\pm by using the operator $\tilde{s}_\pm = P^\dagger \hat{s}_z P$ with P the projection operator defined in the valence space, and the spin-Chern number is then the difference between the Chern numbers of the two newly defined spin subspaces \tilde{s}_\pm [59, 60].

We start with the tight-binding Hamiltonian for a buckled honeycomb lattice with an AFM ex-

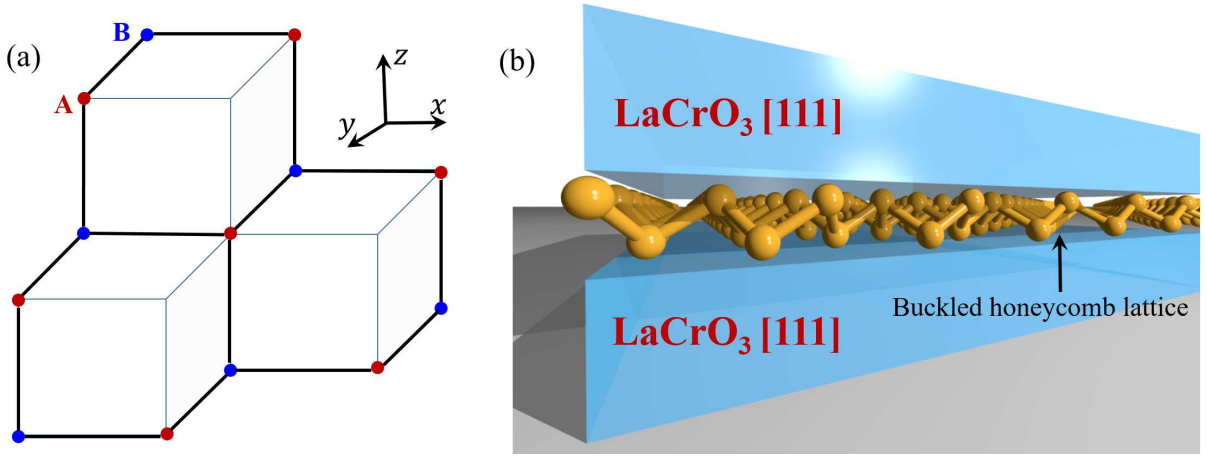


Figure 4.10: (a) Perovskite LaCrO_3 grown along the $[111]$ direction with Cr atoms forming a buckled honeycomb lattice. (b) Schematic plot for replacing one atomic layer of Cr atoms by Au atoms. Gold balls are Au atoms. Two blue slabs are the LaCrO_3 grown along the $[111]$ direction.

change field and a staggered electric potential (see figure 4.7)

$$\tilde{\mathcal{H}} = \left[\mathcal{H} + i\lambda_R \sum_{\langle i,j \rangle \alpha \beta} a_{i\alpha}^\dagger \hat{\mathbf{z}} \cdot (\vec{s}_{\alpha\beta} \times \hat{d}_{ij}) b_{j\beta} \right] + H.c. \quad (4.12)$$

where the first term in the bracket is given in Eq. (4.9); and the second term is for the Rashba-type spin-orbit coupling with λ_R the strength of Rash-type SOC [65], $\hat{\mathbf{z}}$ is the unit vector along the z direction, $\vec{s}_{\alpha\beta}$ are the Pauli matrices in the real spin space with α and β representing the spin degree of freedom, \hat{d}_{ij} is a unit vector pointing from the site i to the site j .

The valence bands cannot be decomposed into two subspaces simply by their spins due to the off diagonal Rashba-type SOC term that mixes two spin channels. An alternative way of separating the valence space into two closed subspaces is needed. It has been suggested that one can project the electron spin operator

$$s_z = \text{diag}(1, -1) \otimes \text{diag}(1, 1)$$

onto the subspace spanned by the eigenstates of occupied bands Ψ_1 and Ψ_2 . Diagonalizing of the newly defined \tilde{s}_z matrix gives us two separated spin space [59]. The matrix form of \tilde{s}_z is

$$\tilde{s}_z(\mathbf{k}) = \begin{bmatrix} \langle \Psi_1(\mathbf{k}) | \hat{s}_z | \Psi_1(\mathbf{k}) \rangle & \langle \Psi_1(\mathbf{k}) | \hat{s}_z | \Psi_2(\mathbf{k}) \rangle \\ \langle \Psi_2(\mathbf{k}) | \hat{s}_z | \Psi_1(\mathbf{k}) \rangle & \langle \Psi_2(\mathbf{k}) | \hat{s}_z | \Psi_2(\mathbf{k}) \rangle \end{bmatrix}. \quad (4.13)$$

By diagonalizing Eq. (4.13), we have two eigenvalues of s_\pm with corresponding eigensolutions $\psi_\pm = (\psi_\pm^1, \psi_\pm^2)$, which can be used to redefine new spin-up and -down states through linear combination: the tilted spin-up and spin-down channel are

$$\Phi_\pm = \psi_\pm^1 \Psi_1(\mathbf{k}) + \psi_\pm^2 \Psi_2(\mathbf{k}).$$

In this way, one can split the valence space into two well closed subspaces. The separation of the two

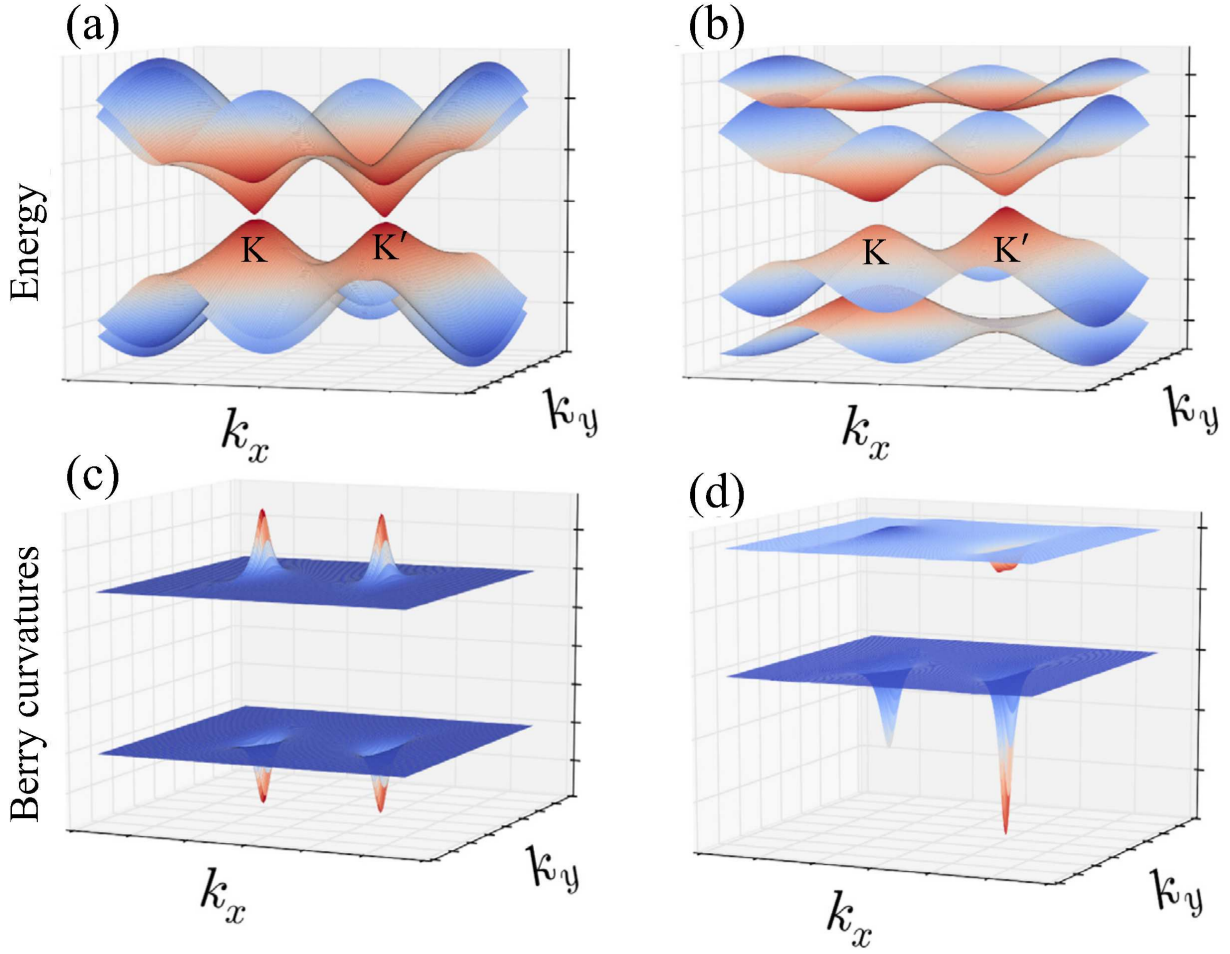


Figure 4.11: (a) Energy dispersions for a buckled honeycomb lattice with $V = 0, M = 0, \lambda = 0.2t_0$ and $\lambda_R = 0.1t_0$ and corresponding (c) Berry curvatures. (b) Energy dispersions for a buckled honeycomb lattice with $V = t_0, M = 1.1t_0, \lambda = 0.2t_0$ and $\lambda_R = 0.3t_0$.

subspaces is guaranteed as long as there is a well defined gap between dispersions of $s_+(\mathbf{k})$ and $s_-(\mathbf{k})$. One then can define the Chern numbers C_\pm for each subspace with eigenfunctions Φ_\pm .

To reveal the stability of the QSHE against Rashba-type SOC, we first turn off the staggered potential and the AFM exchange field by letting $V = 0$ and $M = 0$. The four eigenenergies near the $K' = (0, \frac{4\pi}{3a_0})$ point are

$$E(\mathbf{k}) = \pm \sqrt{v_f^2 \mathbf{k}^2 + \left(\lambda + \frac{3\lambda_R}{2} \right)^2} + \frac{3\lambda_R}{2},$$

$$\pm \sqrt{v_f^2 \mathbf{k}^2 - \left(\lambda + \frac{3\lambda_R}{2} \right)^2} - \frac{3\lambda_R}{2}, \quad (4.14)$$

where \mathbf{k} is measured from the K' point, v_f is the Fermi velocity. Similarly, the energy dispersion near

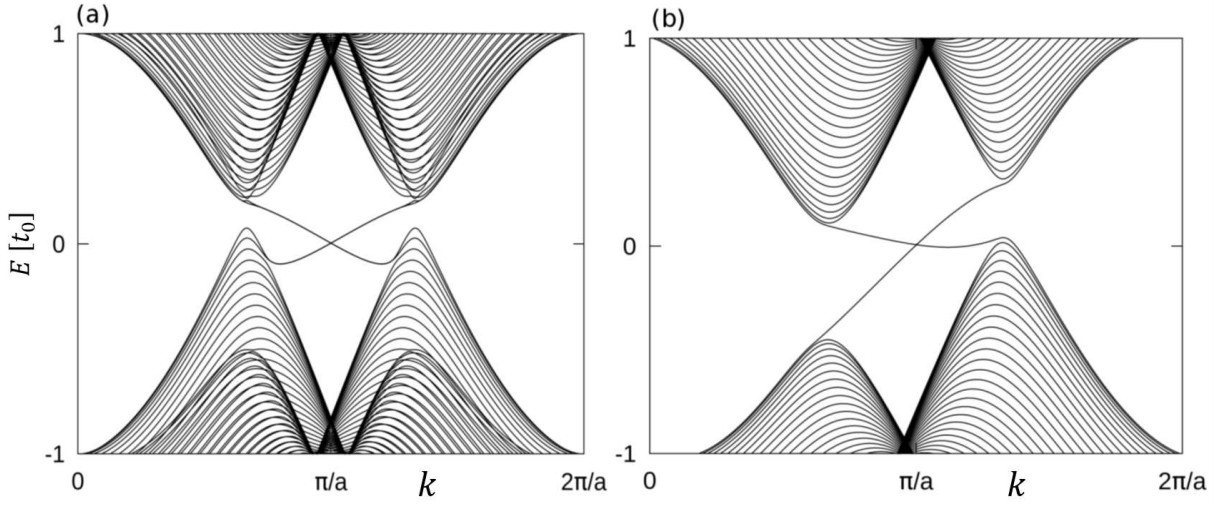


Figure 4.12: (a) and (b) Topological edge states for a 100-unit-cell-width Zigzag nanoribbon of honeycomb lattice with same parameters as figure 4.11(a) and figure 4.11(b) respectively.

the $K = (0, \frac{4\pi}{3a_0})$ is found exactly the same as that given in Eq. (4.14). The energy gap at the K' point is

$$\Delta_{K'} = 2\lambda - 3\lambda_R, \quad (4.15)$$

indicating that the QAHE can be destroyed by the Rashba-type SOC when it is larger than the critical value $\lambda_R^c = 2\lambda/3$ [7, 8, 60].

We now examine the robustness of QSHE by evaluating the newly defined Chern number C_{\pm} . The bulk dispersion for QSHE with $\lambda_{so} = 0.2t_0$ and $\lambda_R = 0.1t_0$ ($V = M = 0$) is displayed in figure 4.11(a), where there is a finite energy gap at the K' and K from left to right. The corresponding Berry curvatures $\vec{\Omega}_{\pm}$ for the two newly defined spin subspaces Φ_{\pm} are displayed in 4.11(c) [the upper (lower) part is for $\vec{\Omega}_{+}$ ($\vec{\Omega}_{-}$)]. The spin-Chern number is then $C_s = [1 - (-1)]/2 = 1$, manifesting a nontrivial QSHE with weak Rashba-type SOC.

The band structure for a 100-unit-cell-wide Zigzag ribbon of honeycomb lattice with same parameters as figure 4.11(a) is calculated. As shown in figure 4.12(a), with nonzero Rashba-type SOC, the QSHE still supports two degenerated gapless edge states with opposite spins.

It is well known that the gapless edge states of QSHE are fragile against the time-reversal symmetry breaking, i.e., a weak magnetic impurity can destroy the QSHE. However, for a QSHE with large topological band gap, it is easy to imagine that an extremely weak magnetic impurity must not be able to close bulk gaps, which means that the Hamiltonian in this case can still be continuously deform into the one preserving time-reversal symmetry, i.e., the two system are topologically equivalent. A conventional \mathbb{Z}_2 index [7, 8] is not defined for the time-reversal symmetry broken case, we then employ the Chern numbers C_{\pm} defined above. The bulk energy gap is an indirect one between the K' and K points with magnitude

$$\Delta = 2\lambda + V - \sqrt{V^2 + 9\lambda_R^2}, \quad (4.16)$$

indicating a critical Rashba-type SOC $\lambda_R^c = 2\sqrt{\lambda(\lambda + V)}$ for closing the topological band gap, which can be much larger than $\lambda_R^c = 2\lambda/3$ for a large staggered potential V . A typical energy dispersion of

the novel QAHE is shown in figure 4.11(b) with $\lambda = 0.2t_0$, $\lambda_R = 0.3t_0$, $V = t_0$ and $M = 1.1t_0$. The Chern numbers for the two spin subspaces are $C_+ = 0$, $C_- = -1$ with the Berry curvatures displayed in figure 4.11(d). The edge state with same parameters is displayed in figure 4.12(b). The novel QAHE is then concluded to be robust against the Rashba-type SOC compared to the QSHE.

4.4 Conclusion

We propose a novel topological material composed of LaCrO_3 of perovskite structure grown along the $[001]$ direction with one atomic layer replaced by the inverse-perovskite material Sr_3PbO . Based on first-principles calculations and low-energy effective Hamiltonian, we demonstrate that the topological state is characterized by simultaneous nonzero charge and spin Chern numbers, which can support spin-polarized dissipationless edge current in a finite sample. Supported by the anti-ferromagnetic exchange field and spin-orbit coupling inherent in the compounds, no extrinsic operation is required for achieving the topological state. Importantly, these two materials are stable in bulk and match each other with only small lattice distortions, which makes the composite material easy to synthesize.

Majorana Fermions in Topological Superconductors

5.1 Introduction

5.1.1 Majorana states

Majorana fermions (MFs) are particles equivalent to their own anti-particles [103]. It has been revealed that MFs can be hosted in solid state materials, such as chiral p -wave superconductor [22, 104] and one-dimensional Kitaev chain [105]. It is well known that quasiparticle excitations in superconductors are superpositions of electrons and holes [106], which makes superconductors a natural platform for realizing MFs [103]. In a spinless superconductor, the wavefunction of quasiparticle excitations is $\gamma = u c^\dagger + v c$ with c the annihilation (creation) operator for an electron (hole) and $|u|^2 + |v|^2 = 1$. The corresponding wavefunction for the charge conjugated excitations is $\gamma^\dagger = v^* c^\dagger + u^* c$. For MFs, we must have $\gamma = \gamma^\dagger$, indicating $|u|^2 = |v|^2 = 1/2$. Distinct from fermions that obey $\{c, c\} = 0$, $\{c^\dagger, c^\dagger\} = 0$ and $\{c^\dagger, c\} = 1$, MFs satisfy

$$\gamma^2 = \gamma^\dagger \gamma = (v^* c^\dagger + u^* c)(u c^\dagger + v c) = |u|^2 c^\dagger c + |v|^2 c c^\dagger = \frac{1}{2}, \quad (5.1a)$$

$$\{\gamma_i, \gamma_j\} = \delta_{ij}, \quad (5.1b)$$

where δ_{ij} is the delta function that equals 1 when $i = j$ and 0 otherwise.

It should be noted that any complex fermion can be decomposed into real and imaginary parts, each part is a MF

$$f = \frac{1}{\sqrt{2}}(\gamma_1 + i\gamma_2), \quad f^\dagger = \frac{1}{\sqrt{2}}(\gamma_1 - i\gamma_2). \quad (5.2)$$

The particle number n is then

$$n = f^\dagger f = \frac{1}{2}(\gamma_1^2 + \gamma_2^2 + i\gamma_2\gamma_1 - i\gamma_1\gamma_2) = 1 + i\gamma_2\gamma_1. \quad (5.3)$$

Reorganizing above equation and multiplying both sides by ε , we have

$$i\varepsilon\gamma_2\gamma_1 = \varepsilon(n-1). \quad (5.4)$$

By Pauli exclusion principle, n can only be 0 or 1, indicating that coupling between two MFs ε results in a two-level system: empty state with energy $-\varepsilon$ and occupied state with energy 0. For $\varepsilon \rightarrow 0$, we have degenerated empty and occupied states, which is useful for non-Abelian statistics, as we will show.

5.1.2 Realizations of Majorana fermions

Great research effort has been devoted to searching for MFs in condensed matter systems in the last decade since the particles can be used for constructing topological qubits and robust quantum computation [107–109]. Systems that can realize MFs include Pfaffian $\nu = 5/2$ fractional quantum Hall state [110], chiral p -wave superconductors (SCs) [104], one-dimensional (1D) spinless SCs [105] and superfluidity of cold atoms [111, 112]. Recently, two heterostructure systems are suggested as possible MF hosts, one is the \mathbb{Z}_2 topological insulator in proximity to s -wave SC and ferromagnetic insulator (FMI), the other is the spin-orbit coupled semiconductor (SM) sandwiched by s -wave SC and FMI (SC/SM/FMI) [9, 11, 20, 113–116]. Both systems are effective two-dimensional (2D) $p + ip$ topological superconductors, characterized by nonzero Chern numbers [4, 117]. 1D semiconductor nanowires with spin-orbit coupling in proximity to s -wave SC under magnetic field has also been investigated both theoretically and experimentally for realizing MFs [118–125]. Lately, a promising signal of MFs has been captured in the device of InSb nanowire/ s -wave SC [125]. In these heterostructure systems, the rare p -wave pairing are superseded by the interplay between proximity-induced s -wave superconductivity and strong spin-orbit coupling.

It was revealed that MFs appear inside vortex cores in topological p -wave SCs [104], and that non-Abelian statistics can be achieved by exchanging positions of vortices hosting MFs [22]. However, it is difficult to manipulate vortices in experiments, which may hinder the realization of this genius idea. To circumvent this problem, MFs at sample edges of topological SCs have been considered [21]. Making use of their topological properties, edge MFs can be braided with desired non-Abelian statistics by tuning point-like gate voltages on links among topological SC samples. In order to make the edge MFs stable, one needs to embed the device into a good insulator. The size of topological SCs should also be chosen carefully since the wave-functions of edge MFs become too dilute for large samples, which makes edge MFs fragile due to excited states with small energy gap.

In this chapter we concentrate on MFs grabbed at vortex cores. We demonstrate that the core MFs can be liberated from vortex cores, transported and braided by applications of local gate voltages. The scheme takes full advantages of SC/SM/FMI heterostructure [see figure 3(a)] in the way shown schematically in figure 5.1: four holes are punched in the SM layer, and three electrodes are placed above the small regions between holes; gate voltages can be applied via the electrodes, and the ones at a high voltage state (pink rectangular prisms in figure 5.1) connect holes by killing electron hoppings locally; one vortex is induced and pinned right beneath each hole in the common superconductor substrate. The key observation is that the geometric topology of the SM layer can be controlled by local gate voltages, and that when even number of holes are connected, core MFs fuse into quasi-particle states with finite energies, while one core MF exists when odd number of holes are connected. Core MFs can then be liberated from and transported among vortices with a sequence of turning on and off gate voltages at the electrodes. By solving the time-dependent Bogoliubov-de Gennes (TDBdG) equation upon adi-

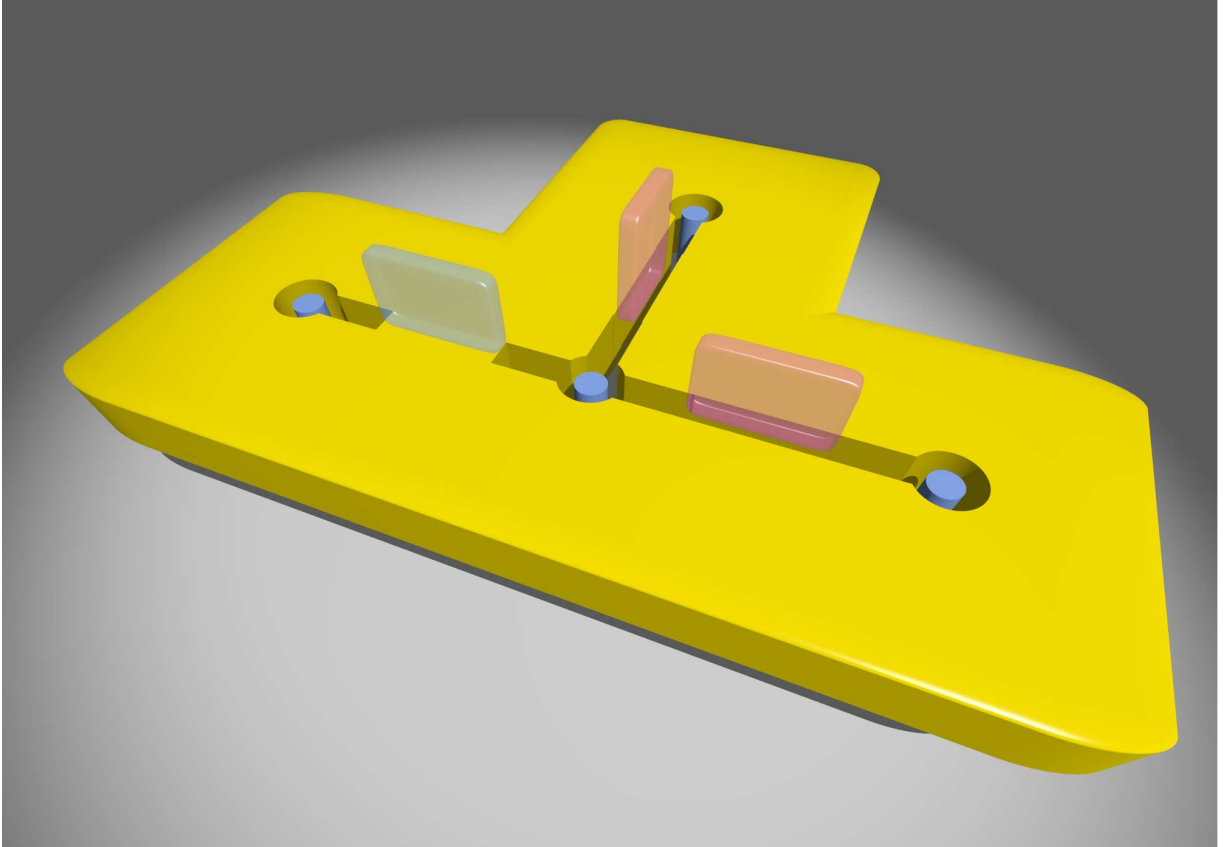


Figure 5.1: Schematic device setup for braiding MFs at vortex cores. There are four holes in SM layer (yellow platform) with one superconducting vortex (blue cylinder) pinned right beneath each of them. The electrodes at high-voltage states (pink rectangular prisms) prohibit electron hoppings in the regions below them, and thus connect effectively the holes; the blue rectangular prism denotes an electrode at zero-voltage state.

abatic tunings of gate voltages, we simulate the time evolution of MF wave-functions and confirm that the braiding of core MFs obeys non-Abelian statistics. Finally, we compare briefly our scheme of manipulating MFs with other proposals in both topological 2D $p + ip$ superconductors and 1D nanowire networks and show advantages of our scheme.

5.2 Topological superconductivity

We start from a tight-binding Hamiltonian on square lattice for a semiconductor with Rashba-type spin-orbit coupling in proximity to a ferromagnetic insulator [21, 122, 126, 127]

$$H_0 = - \sum_{i,j,\sigma} t_{ij} \hat{c}_{i\sigma}^\dagger \hat{c}_{j\sigma} - \mu \sum_{i,\sigma} \hat{c}_{i\sigma}^\dagger \hat{c}_{i\sigma} + \sum_i V_z \left(\hat{c}_{i\uparrow}^\dagger \hat{c}_{i\uparrow} - \hat{c}_{i\downarrow}^\dagger \hat{c}_{i\downarrow} \right) + \sum_{i,\sigma,\sigma'} \left\{ i t_{\alpha i} \left[\hat{c}_{(i+\mathbf{x})\sigma}^\dagger \hat{s}_y^{\sigma\sigma'} \hat{c}_{i\sigma'} - \hat{c}_{(i+\mathbf{y})\sigma}^\dagger \hat{s}_x^{\sigma\sigma'} \hat{c}_{i\sigma'} \right] + h.c. \right\}, \quad (5.5)$$

where t_{ij} and $t_{\alpha i}$ are the nearest-neighbor hopping rates of electrons with reserved and flipped spin directions respectively; μ and V_z are chemical potential and strength of Zeeman field respectively; $c_{i\sigma}^\dagger$ creates one electron with spin σ at lattice site i ; $\vec{s} = (\hat{s}_x, \hat{s}_y, \hat{s}_z)$ are the Pauli matrices for spin.

The proximity-induced superconductivity in SM is described by

$$H_{sc} = \sum_i \left(\Delta_i \hat{c}_{i\uparrow}^\dagger \hat{c}_{i\downarrow}^\dagger + h.c. \right), \quad (5.6)$$

where Δ_i is the pairing potential at site i . The Bogoliubov-de Gennes (BdG) equation of total Hamiltonian $H = H_0 + H_{sc}$ is given by

$$\begin{pmatrix} H_0 & \Delta \\ \Delta^\dagger & -\hat{\sigma}_y H_0^* \hat{\sigma}_y \end{pmatrix} \Psi(\vec{r}) = E \Psi(\vec{r}) \quad (5.7)$$

where $\Psi(\vec{r}) = [u_\uparrow(\vec{r}), u_\downarrow(\vec{r}), v_\uparrow(\vec{r}), -v_\downarrow(\vec{r})]^T$ is the Nambu spinor, and the quasi-particle operator is $\gamma^\dagger = \int d\vec{r} \sum_\sigma u_\sigma(\vec{r}) \hat{c}_\sigma^\dagger(\vec{r}) + v_\sigma(\vec{r}) \hat{c}_\sigma(\vec{r})$. For a typical square sample with 200×200 sites, the Hamiltonian matrix in (5.7) has a dimension of $10^5 \times 10^5$.

5.2.1 Hamiltonian in momentum space and Chern number

Before solving the BdG equation in a finite sample, we reveal the condition for achieving topological superconducting state in an infinite system. We transform Hamiltonian (5.5) into momentum space by expanding the annihilation operator as

$$\hat{c}_{i\sigma} = \frac{1}{\sqrt{N}} \sum_{\mathbf{k}} c_{\mathbf{k}\sigma} e^{i\mathbf{k} \cdot \mathbf{i}}, \quad (5.8)$$

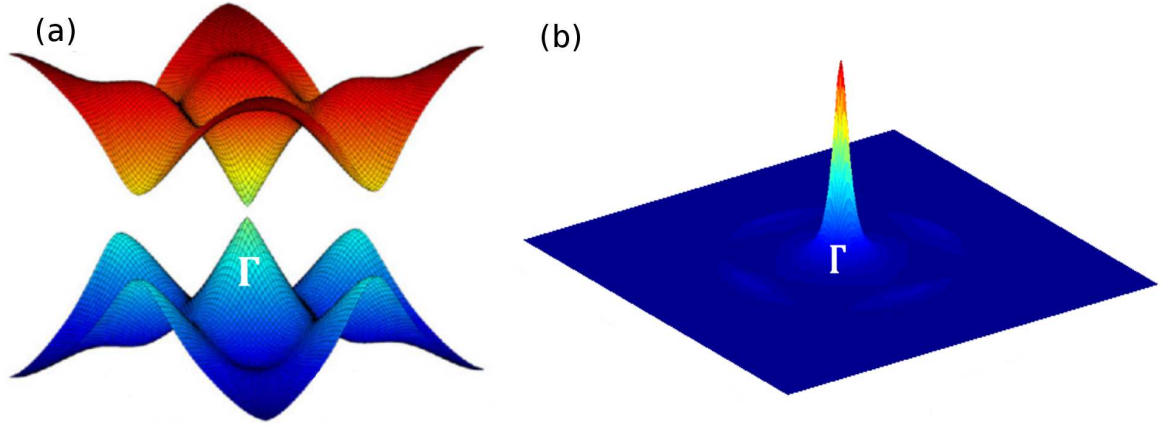


Figure 5.2: (a) Dispersions of two bands close to Fermi level. (b) Berry curvature $\nabla \times \mathcal{A}$ of occupied bands in the first Brillouin zone.

where N is the total number of lattice sites, \mathbf{k} is the crystal momentum. We then obtain the momentum space Hamiltonian on the basis $[c_{\mathbf{k}\uparrow}, c_{\mathbf{k}\downarrow}, c_{-\mathbf{k}\uparrow}^\dagger, c_{-\mathbf{k}\downarrow}^\dagger]^T$

$$H(\mathbf{k}) = \begin{pmatrix} \varepsilon(\mathbf{k}) + V_z \hat{\sigma}_z + \vec{R}(\mathbf{k}) \cdot \vec{\sigma} & i\Delta(\mathbf{k}) \hat{\sigma}_y \\ -i\Delta^*(\mathbf{k}) \hat{\sigma}_y & -\varepsilon(\mathbf{k}) - V_z \hat{\sigma}_z + \vec{R}(\mathbf{k}) \cdot \vec{\sigma}^* \end{pmatrix}, \quad (5.9)$$

where $\varepsilon(\mathbf{k}) = -2t_0(\cos k_x + \cos k_y) - \mu$ and $\vec{R}(\mathbf{k}) = (-2t_\alpha \sin k_y, 2t_\alpha \sin k_x)$.

Diagonalising Hamiltonian (5.9), we obtain the energy dispersion (see figure 5.2(a))

$$E(\mathbf{k}) = \pm \sqrt{\varepsilon^2 + |R|^2 + V_z^2 + |\Delta|^2 \pm 2\sqrt{V_z^2 |\Delta|^2 + \varepsilon^2 (V_z^2 + |R|^2)}}, \quad (5.10)$$

with gap closed at

$$\varepsilon^2 + |R|^2 + V_z^2 + |\Delta|^2 = 2\sqrt{V_z^2 |\Delta|^2 + \varepsilon^2 (V_z^2 + |R|^2)}. \quad (5.11)$$

By squaring both sides of (5.11), we find that the conditions to close the bulk energy gap are

$$|\Delta| \cdot |R| = 0, \quad (5.12a)$$

$$\varepsilon^2 + |\Delta|^2 = V_z^2 + |R|^2. \quad (5.12b)$$

Equation (5.12a) can be fulfilled only when $|R| = 0$ (since $|\Delta| > 0$). The \mathbf{k} -points with $|R| = 0$ are $(k_x, k_y) = (0, 0), (0, -\pi), (-\pi, 0)$ or $(-\pi, -\pi)$ in the first Brillouin zone $T^2 = [-\pi, \pi) \otimes [-\pi, \pi)$. Combining the two conditions in Eq. (5.12a), we arrive at the critical V_z to close the bulk energy gap at \mathbf{k} -points where $|R(\mathbf{k})| = 0$

$$V_z^2 = [2t_0(\cos k_x + \cos k_y) + \mu]^2 + |\Delta|^2. \quad (5.13)$$

To investigate whether the system is topologically nontrivial when the bulk gap closes and reopens

while tuning the Zeeman field V_z , we evaluate the Chern number [4, 117]

$$c = \frac{1}{2\pi i} \int_{T^2} d^2\mathbf{k} \cdot (\vec{\nabla} \times \vec{\mathcal{A}}) \quad (5.14)$$

with Berry connection defined as $\mathcal{A}_\mu = \sum_{n; E_n(\mathbf{k}) < 0} \langle \Phi_n(\mathbf{k}) | \partial_{k_\mu} \Phi_n(\mathbf{k}) \rangle$ ($\mu = x, y$), where summation is taken for all occupied bands $E_n(\mathbf{k}) < 0$, and $\Phi_n(\mathbf{k})$ is the wave-function of band n at momentum \mathbf{k} . Integrating the Berry curvature $\vec{\nabla} \times \vec{\mathcal{A}}$ shown in figure 5.2(b) over the Brillouin zone [36], we find that $c = 1$ for $\sqrt{(\mu + 4t_0)^2 + \Delta^2} < V_z < \sqrt{\mu^2 + \Delta^2}$ with $\mu \leq -2t_0$. The nonzero Chern number is attributed to the topologically nontrivial energy gap at Γ point $(k_x, k_y) = (0, 0)$ while those at $(0, -\pi)$, $(-\pi, 0)$ and $(-\pi, -\pi)$ remain trivial [112, 118, 128]. The nonzero Chern number indicates that the system is topological and thus may support MFs.

5.3 Manipulations of core Majorana fermions

5.3.1 Core Majorana fermions

Now we study a finite sample with two separated holes in the SM and two vortices of positive vorticity pinned right beneath them [see top panel of figure 5.3(a)]. The typical size of a sample is $600 \times 300 \text{ nm}^2$, which is divided into 400×200 square grids, corresponding to Hamiltonian matrix of dimension $10^5 \times 10^5$ in Eq. (5.7). By solving the BdG equation for this case, we obtain the energy spectra of excitations and eigen-functions. Two zero-energy states are found at the holes, whereas no such state at the edge, as shown in figure 5.3(b). We examine the four spinor components of the zero-energy states, and find $u_\uparrow = v_\uparrow^*$ and $u_\downarrow = v_\downarrow^*$ [displayed explicitly in figure 5.3(c) for the right hole], which results in $\gamma^\dagger = \gamma$, indicating that the two zero-energy states are Majorana states.

It should be noticed that the excitation energy gap at vortices is about four times larger than that at the edge [see inset of figure 5.3(b)], which makes the core MFs more stable than edge MFs [21]. On the other hand, because the minigap associated with Andreev bound states at superconducting vortex core proximity-induced in SM is roughly $\Delta^2 / \sqrt{\Delta^2 + \mu^2} \sim \Delta$ with a small Fermi energy $\mu \sim \Delta$ [126], the influence from Andreev bound states to the core MFs can be neglected. It is in contrast to the case of SC exposed to vacuum where $\mu \gg \Delta$ and thus the minigap is small in order of Δ^2 / μ .

Next, we impose a point-like gate voltage on the region between the two holes to prohibit direct hopping of electrons by lifting the on-site energy there as in the bottom panel of figure 5.3(a) (see also figure 5.1). This merges effectively the two isolated holes into a unified one. Solving the BdG equation for this case, there is no zero-energy quasi-particle, since the combined hole includes two vortices [111].

5.3.2 Transportation of Majorana fermions

Based on the above result that two MFs can fuse into finite energy excitations by connecting two holes, we can design a way of liberating and transporting a MF from one vortex to another. Initially, the top and middle holes are connected together while the leftmost one is isolated and hosts a MF (see figure 5.4(a) with $t = 0$). We then combine these three holes by applying gate voltages on the region between the left and middle ones, which causes the MF to spread itself over the unified hole including three vortices (see figure 5.4(a) with $t = T$). Finally, the MF is moved totally to the top by disconnecting

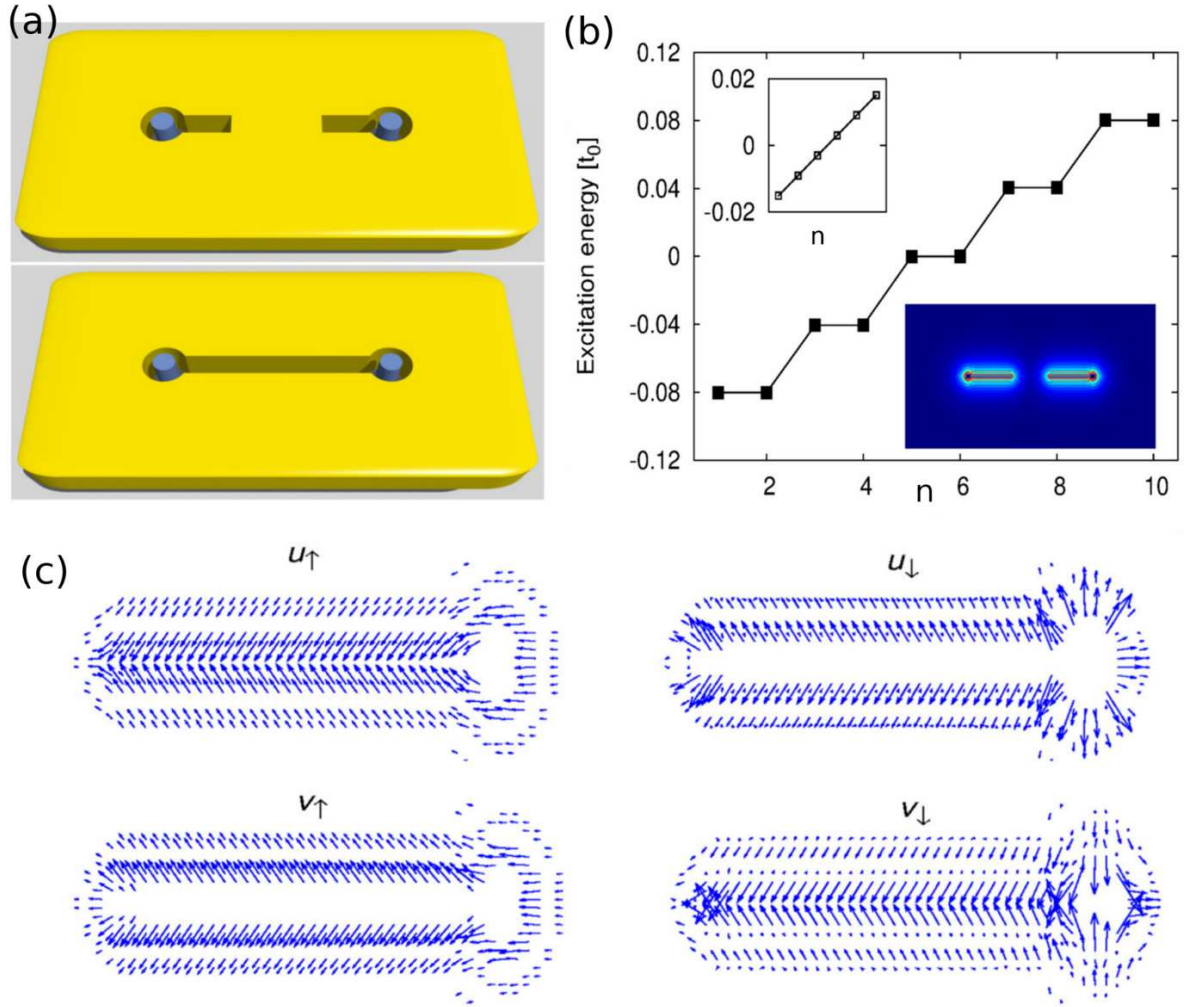


Figure 5.3: (a) System of two holes and two vortices of positive vorticity with holes isolated (top panel) and connected (bottom panel). (b) Energy spectrum of several low-energy excitations at vortex cores when the holes are isolated with n the serial number of eigenstates with energies close to zero. Upper inset: energy spectrum of excitations at the sample edge. Lower inset: distributions of zero-energy quasiparticles. Results are for $\Delta = 0.5t_0$, $V_z = 0.8t_0$, $\mu = -4t_0$ and $t_\alpha = 0.9t_0$ with a sample of 400×200 sites. (c) Four spinor components of zero-energy states at the right hole, with the length and azimuth angle of vectors denoting the amplitude and phase of spinor fields respectively.

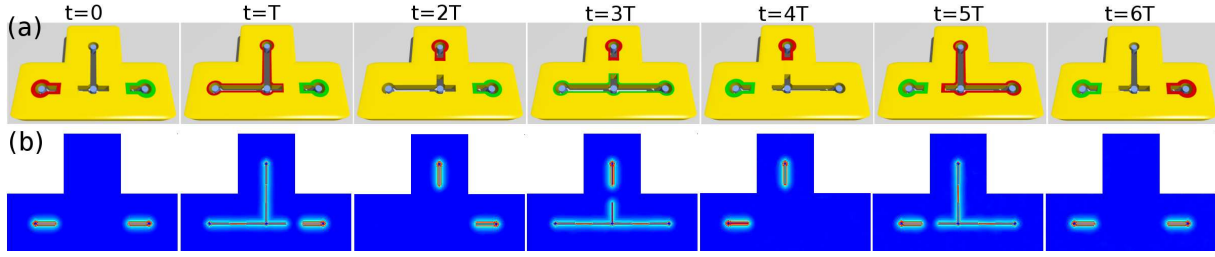


Figure 5.4: (a) Schematic diagram for braiding the two MFs at the left and right holes, colored by red and green respectively. (b) Distributions of the wave-functions of MFs obtained by solving TDBdG.

the top hole from others (see figure 5.4(a) with $t = 2T$). It is noticed that the collapsing of MF wave-function on the top hole is a topological property, and is impossible for electrons and photons. The energy gap remains finite during the whole processes, which guarantees topological protections on the MF state.

5.3.3 Braiding of Majorana fermions

Being able to transport one MF from one hole to another, we extend the scheme to interchange positions of two core MFs in the system shown in figures 5.1 and 5.4. Following the above transportation procedures, we further move the green MF from the right hole to the left one during $t = 2T \sim 4T$ in the same way as above. At last, the red MF stored temporarily at the top hole is transported to the right one in the period $t = 4T \sim 6T$. After the sequence of switching processes, the system comes back to the original state with the red and green MFs exchanged.

In order to keep the topological protection, we need to manipulate the gate voltage in an adiabatic way. The reason is that the MF states have certain probabilities to be excited to higher energy states for non-adiabatic processes, which results in the collapsing of the whole braiding scheme. Given reasonable material parameters, the typical time for a single round of braiding is estimated to be within several nano seconds, which is sufficiently short time for practical applications.

5.3.4 Time-dependent Bogoliubov-de Gennes equation

In order to investigate the impact of position exchanging to MF states, we monitor the time evolution of MF wave-function $|\Psi(t)\rangle$ by solving the TDBdG equation numerically

$$i\hbar \frac{d}{dt} |\Psi(t)\rangle = H(t) |\Psi(t)\rangle, \quad (5.15)$$

where $H(t)$ is given in (5.7) and depends on time via the hopping rates t_{ij} and $t_{\alpha i}$ at the regions between holes, which are tuned adiabatically by the local gate voltages [21].

Even with the powerful computation resources available in these days, it is still hopeless to tackle this problem by directly diagonalising the Hamiltonian $H(t)$ of dimension $10^6 \times 10^6$ for each time instant. Fortunately, it has been revealed that when the exponential operator is expanded by the Chebyshev polynomial

$$\exp[-iH(t)\delta t/\hbar] = \sum_n c_n(\delta t) T_n(H), \quad (5.16)$$

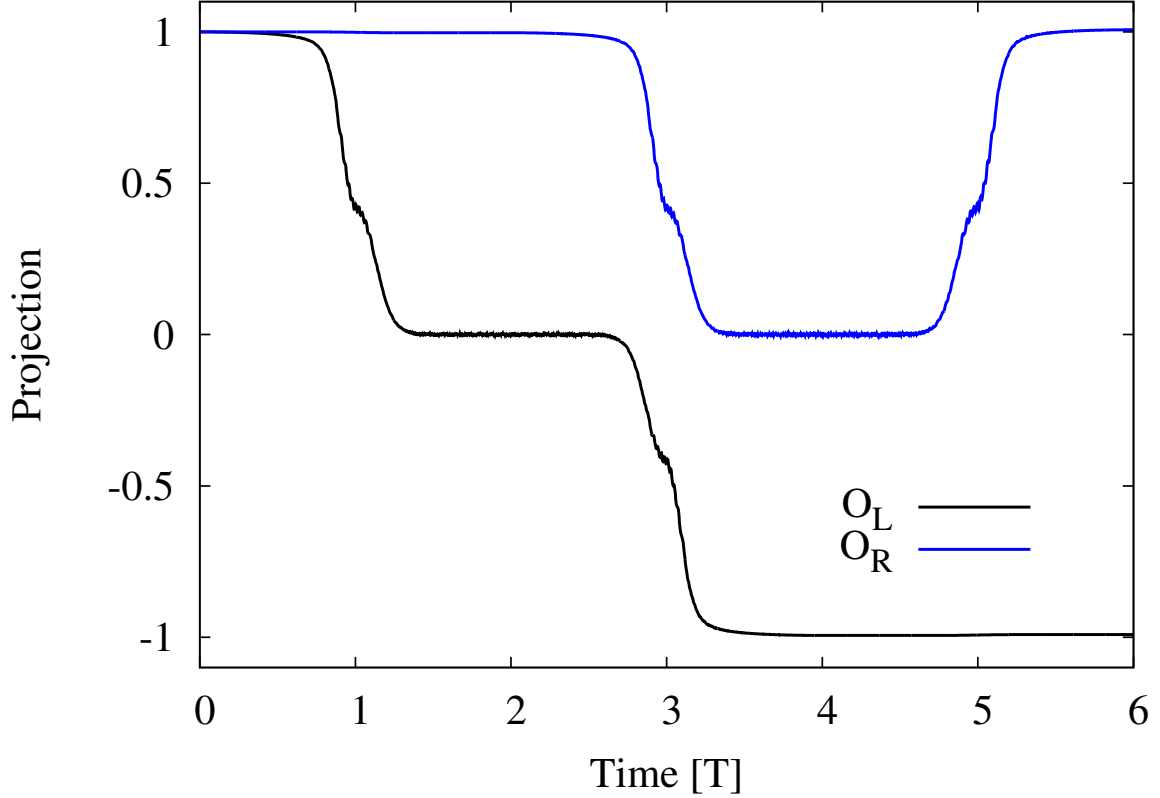


Figure 5.5: Projections of the MF wave-function $|\Psi(t)\rangle$ obtained by TDBdG onto the initial states $O_L = \langle \Psi_L(0) | \Psi(t) \rangle$ and $O_R = \langle \Psi_R(0) | \Psi(t) \rangle$.

the coefficient $c_n(\delta t)$ decreases with n exponentially fast for small δt [129]. Therefore, only several leading terms c_n are necessary for a sufficiently accurate estimate of the time-evolution operator $\exp[-iH(t)\delta t/\hbar]$. Moreover, the Chebyshev polynomials can be constructed based on the recursive relation $T_n(H) = 2HT_{n-1}(H) - T_{n-2}(H)$, which reduces the computation cost further. In this way, the time-dependent wave-function of the MFs can be obtained efficiently with sufficient accuracy in an iterative fashion $|\Psi(t + \delta t)\rangle \simeq \exp[-iH(t)\delta t/\hbar]|\Psi(t)\rangle$.

The wave function at time $t = 0$ is defined as $|\Psi(t=0)\rangle = |\Psi_L(0)\rangle + |\Psi_R(0)\rangle$ with $|\Psi_L(0)\rangle$ and $|\Psi_R(0)\rangle$ the zero-energy states at left and right holes, respectively, as shown in figure 5.4(a) and (b). We evaluate the projections of $|\Psi(t)\rangle$ onto the initial states $O_L = \langle \Psi_L(0) | \Psi(t) \rangle$ and $O_R = \langle \Psi_R(0) | \Psi(t) \rangle$ during adiabatic braiding processes and display them in figure 5.5 for $0 \leq t \leq 6T$. Since four spinor components of MF satisfy $u_\uparrow = v_\uparrow^*$ and $u_\downarrow = v_\downarrow^*$ (see figure 5.3(c)), MF state is simplified to $\Psi(\vec{r}) = [u_\uparrow(\vec{r}), u_\downarrow(\vec{r}), u_\uparrow^*(\vec{r}), -u_\downarrow^*(\vec{r})]^T$. The projections O_L and O_R then must be real numbers. The two MFs pick up opposite signs after exchanging their positions, which can be summarized by

$$\gamma_L \rightarrow \gamma_R, \quad \gamma_R \rightarrow -\gamma_L. \quad (5.17)$$

(5.17) can be written as $\gamma_{L/R} \rightarrow U^{-1}\gamma_{L/R}U$ with the unitary matrix $U = \exp(\pi\gamma_R\gamma_L/4)$. This indicates that the braiding of MFs satisfies non-Abelian statistics [21, 122, 123, 128, 130, 131], as will be shown

explicitly below.

5.4 Comparisons with other proposals for braiding Majorana fermions

5.4.1 Braiding Majorana fermions in two-dimensional p -wave superconductors

We begin by reviewing Ivanov's model for realizing non-Abelian statistics, which describes low-energy excitations bound to vortices in spinless p -wave superconductors [22]. The Hamiltonian is [22, 132, 133]

$$H = \int d^2\mathbf{r} \left[c^\dagger \left(-\frac{\nabla^2}{2m} - \varepsilon_F \right) c + c^\dagger \left[e^{i\theta} |\Delta(\mathbf{r})| (k_x + i k_y) \right] c^\dagger + H.c. \right], \quad (5.18)$$

where the first term describes kinetic energy and chemical potential $-\varepsilon_F$, c^\dagger is electron creation operator, and the second term gives pairing function $\Delta(\mathbf{r})$ with superconducting phase θ , k_x and k_y are electron momenta along x - and y -axis respectively. The Bogoliubov quasi-particle operator is $\gamma^\dagger = u c^\dagger + v c$, which satisfies BdG equation

$$[H, \gamma^\dagger] = E \gamma^\dagger \quad (5.19)$$

with E the eigenenergy of quasi-particle. By taking Hermitian conjugation \dagger at both sides of (5.19), we have

$$[H, \gamma] = -E \gamma, \quad (5.20)$$

indicating the particle-hole symmetry of BdG equation, i.e. $\gamma^\dagger(E) = \gamma(-E)$. Thus, the zero energy states must be double-degenerate, satisfying self-adjoint condition $\gamma^\dagger(E=0) = \gamma(E=0)$, which are MFs.

We first consider how MFs evolve under $U(1)$ gauge transformation by shifting superconducting phase θ to $\theta + \delta\theta$. Since θ can be absorbed into fermionic creation and annihilation operators: $\tilde{c}^\dagger = e^{i\theta/2} c^\dagger$ and $\tilde{c} = e^{-i\theta/2} c$, the new Bogoliubov quasi-particle operator is

$$\tilde{\gamma}^\dagger = u e^{i\theta/2} c^\dagger + v e^{-i\theta/2} c, \quad (5.21)$$

which can diagonalize the gauge-invariant Hamiltonian

$$\tilde{H} = \int d^2\mathbf{r} \left[\tilde{c}^\dagger \left(-\nabla^2/2m - \varepsilon_F \right) \tilde{c} + \tilde{c}^\dagger \left[|\Delta(\mathbf{r})| (k_x + i k_y) \right] \tilde{c}^\dagger + H.c. \right].$$

In the case of 2π phase changing $\theta \rightarrow \theta + 2\pi$, we have $\tilde{\gamma}^\dagger = -\gamma^\dagger$, which is an important result that can be employed to achieve non-Abelian statistics.

In a 2D spinless $p + ip$ superconductor with many vortices, superconducting phase θ around each vortex can be single-valued apart from a cut (dashed black line in figure 5.6), where θ jumps by 2π . It is then easy to see that Majorana wave-function bound to a vortex core picks up a sign $\gamma \rightarrow -\gamma$ after crossing the cut. By interchanging positions of vortices i and $i+1$ (see red arrows in figure 5.6), one observes that MF γ_i passes through the cut of vortex $i+1$ and picks up 2π phase (see figure 5.6), which gives

$$\gamma_i \rightarrow -\gamma_{i+1}. \quad (5.22)$$

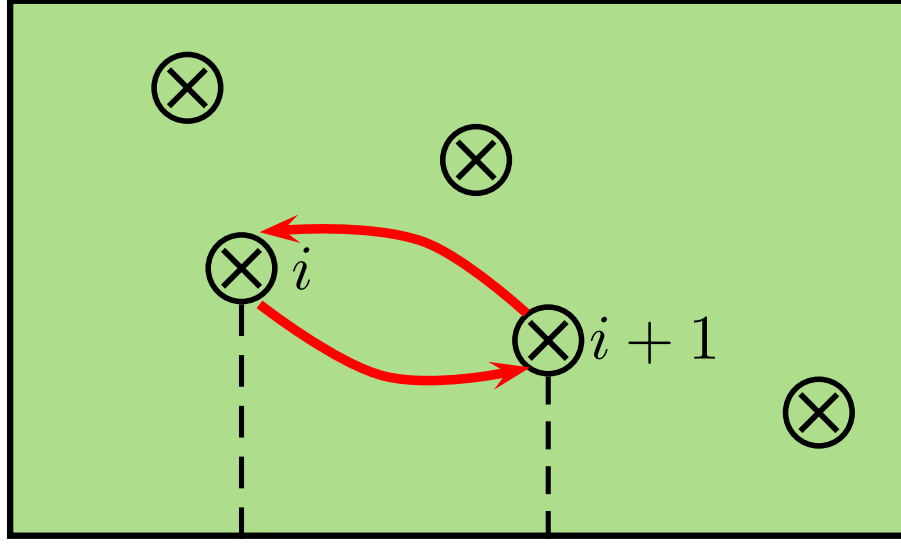


Figure 5.6: Braiding of vortex i and vortex $i + 1$ in a 2D spinless p -wave superconductor. Dashed black lines connecting to bottom boundary are cuts for superconducting vortices [22]. Red arrows are braiding loops.

The other Majorana state at vortex $i + 1$ does not cross the cut of vortex i , thus there is no sign change of MF wave-function

$$\gamma_{i+1} \rightarrow \gamma_i. \quad (5.23)$$

Therefore, we obtain the following rules for MFs evolution after exchanging positions of vortices hosting them

$$T_i : \begin{cases} \gamma_i \rightarrow -\gamma_{i+1}, \\ \gamma_{i+1} \rightarrow \gamma_i \end{cases} \quad (5.24)$$

with T_i the braiding operation, consistent with our results of braiding MFs (5.17).

The unitary operator $\tau(T_i)$ obeying $T_i \gamma_i = \tau(T_i)^{-1} \gamma_i \tau(T_i)$ with T_i defined in (5.24) is given by [22]

$$\tau(T_i) = \frac{1}{\sqrt{2}} (1 + \gamma_{i+1} \gamma_i), \quad (5.25)$$

implying non-Abelian statistics. To demonstrate this, we consider four vortices hosting four MFs $\gamma_1, \gamma_2, \gamma_3$ and γ_4 , which combine into two complex fermions $\Psi_1 = (\gamma_1 + i\gamma_2)/2$ and $\Psi_2 = (\gamma_3 + i\gamma_4)/2$. The unitary operators describing two ways of braiding MFs on basis $[|0\rangle, \Psi_1^\dagger |0\rangle, \Psi_2^\dagger |0\rangle, \Psi_1^\dagger \Psi_2^\dagger |0\rangle]$ ($|0\rangle$)

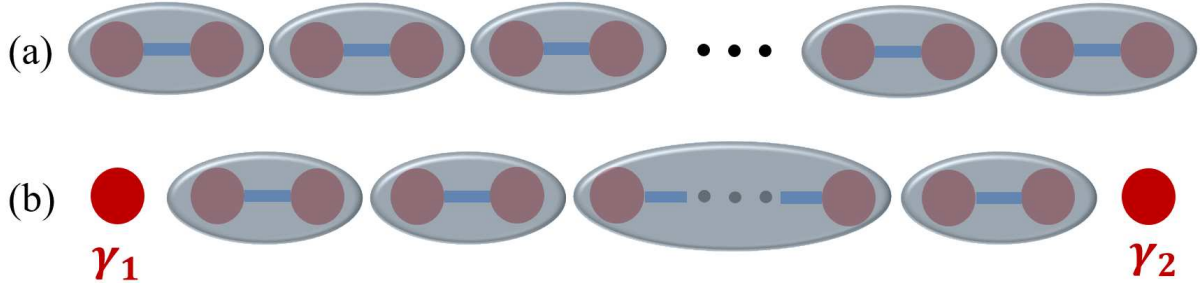


Figure 5.7: (a) Trivial phase with MFs bounded in pair at the same site covered by gray ellipse. (b) Topological phase with dominated couplings between nearest-neighbors, resulting in two isolated MFs γ_1 and γ_2 at the two ends of the Kitaev chain [105].

is the empty state) are [22]

$$\begin{aligned}\tau(T_1) &= \frac{1}{\sqrt{2}}(1 + \gamma_2\gamma_1) = \frac{1}{\sqrt{2}}[1 + i(\Psi_1^\dagger - \Psi_1)(\Psi_1^\dagger + \Psi_1)] \\ &= e^{-i\pi/4} \begin{pmatrix} 1 & 0 & 0 & 0 \\ 0 & i & 0 & 0 \\ 0 & 0 & 1 & 0 \\ 0 & 0 & 0 & i \end{pmatrix},\end{aligned}\tag{5.26}$$

$$\begin{aligned}\tau(T_2) &= \frac{1}{\sqrt{2}}(1 + \gamma_3\gamma_2) = \frac{1}{\sqrt{2}}[1 + i(\Psi_2^\dagger + \Psi_2)(\Psi_1^\dagger - \Psi_1)] \\ &= \frac{1}{\sqrt{2}} \begin{pmatrix} 1 & 0 & 0 & -i \\ 0 & 1 & -i & 0 \\ 0 & -i & 1 & 0 \\ -i & 0 & 0 & 1 \end{pmatrix}.\end{aligned}\tag{5.27}$$

The non-Abelian statistics is then verified by the noncommutative relation of unitary operators $\tau(T_1)\tau(T_2) \neq \tau(T_2)\tau(T_1)$ [108].

Direct manipulations of vortices might be done by using a STM tip, but suffer great difficulties. This is not only because that large effective masses of vortices make transportations of themselves hard and time-consuming, but also it is almost impossible to return vortices to exact positions in order to form a closed braiding loop, which would cause systematic errors in topological quantum computations. On the contrary, in our scheme of braiding MFs, vortices stay pinned at their original positions and thus no motion of vortices is necessary. What we do is tuning gate voltages at small regions connecting holes during braiding processes (see figure 5.3(a) and figure 5.4). It is guaranteed that MFs exchange their positions exactly after braiding.

5.4.2 Braiding Majorana fermions in nanowire networks

A toy model for realizing MFs in a N -site one-dimensional (1D) spinless p -wave superconductor was proposed by Kitaev [105]

$$H_{\text{Kitaev}} = -\mu \sum_{i=1}^N c_i^\dagger c_i - \sum_{i=1}^{N-1} \left[t c_i^\dagger c_{i+1} + |\Delta| e^{i\theta} c_i c_{i+1} + H.c. \right], \quad (5.28)$$

with μ the chemical potential, t nearest neighbor hopping rate, Δ superconducting gap function with phase θ . The system is in a topologically nontrivial state when $|\mu| < 2t$ characterized by winding number $\nu = 1$, otherwise it is topologically trivial (see detailed derivations in Appendix B), as shown in figure 5.7.

In the special case $\mu = 0$ and $t = |\Delta|$, Hamiltonian (5.28) reduces to [105]

$$H = -it \sum_{i=1}^{N-1} \gamma_{B,i} \gamma_{A,i+1} \quad (5.29)$$

with

$$\gamma_{A,i} = -ie^{-i\theta/2} c_i^\dagger + ie^{i\theta/2} c_i, \quad \gamma_{B,i} = e^{-i\theta/2} c_i^\dagger + e^{i\theta/2} c_i, \quad (5.30)$$

which are Majorana operators satisfying self-adjoint condition $\gamma_{\alpha,i}^\dagger = \gamma_{\alpha,i}$, $i = 1, \dots, N$ is lattice site index of the 1D system. Observing that the two terms $\gamma_{A,1}$ and $\gamma_{B,N}$ do not appear in the Hamiltonian (5.29), it can be concluded that the system can support two zero-energy quasi-particle states localized at two ends of the 1D superconductor (site 1 and N), while quasi-particles at other sites bind into complex fermions with finite energies. The two end states are just MFs, which appear in the topological phase for $|\mu| < 2t$ and disappear in the non-topological phase with $|\mu| > 2t$ [105, 115].

In 2D spinless $p+ip$ superconductors, MFs bound to vortex cores catch nonzero Berry phases while moving around other vortices, which give rise to non-Abelian statistics by exchanging vortices [22]. At the first glance, it seemed impossible to realize non-Abelian statistics by exchanging Majorana states in 1D systems since vortices are absent, and two MFs collide with each other and fuse into finite energy states while exchanging them. Alicea *et al.* proposed to interchange MFs in a T-junction nanowire network (see figure 5.8) and proved that the exchanging of MFs follows non-Abelian statistics [128]. They realize Kitaev's toy model by putting a semiconductor nanowire with strong spin-orbit coupling on top of an s -wave superconductor [115, 118, 119, 125]. For simplicity, we adopt the Kitaev model to demonstrate braiding processes in the following.

The authors consider two segments of 1D nanowires forming a T-junction [128], as shown in figure 5.8. Nanowire in the topological phase (green line) can be tuned into non-topological (light green line) region by adjusting local chemical potential μ using local gate voltage. To exchange positions of MFs in the T junction (see figure 5.8), the authors first initialize the horizontal nanowire into topological state [128], hosting MFs $\gamma_{A,1}$ and $\gamma_{B,N}$ at the two ends (see figure 5.8(a)). The vertical nanowire is in the non-topological phase. By driving left part of horizontal nanowire into non-topological state and then vertical one into topological state, $\gamma_{A,1}$ is transported to the bottom of vertical nanowire (see figure 5.8(b)). Next, $\gamma_{B,N}$ at right end is moved to left end of horizontal nanowire (see figure 5.8(c)). Finally, $\gamma_{A,1}$ is moved to right end of horizontal nanowire (see figure 5.8(d)), which finishes interchanging of MFs. To track how $\gamma_{A,1}$ and $\gamma_{B,N}$ evolve after braiding, one can evaluate Berry phases acquired by

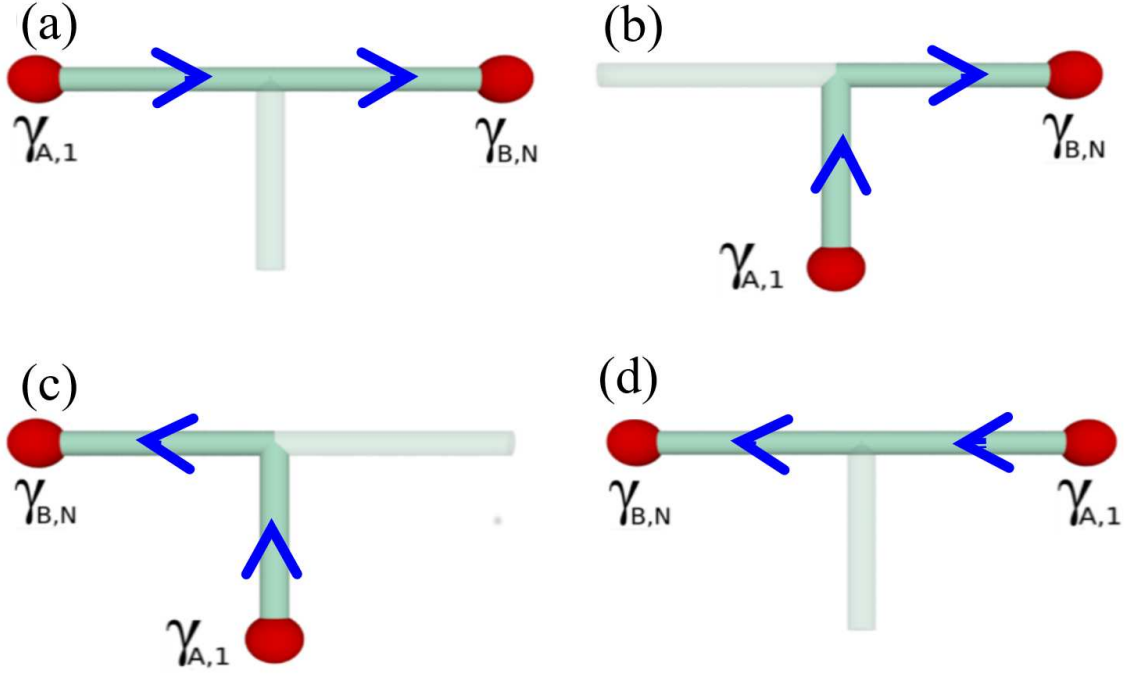


Figure 5.8: Schematic diagram for braiding MFs $\gamma_{A,1}$ and $\gamma_{B,N}$ in a T-junction nanowire network [115]. Green lines are nanowires in the topological phase and can support MFs (red balls). Light green lines are in the non-topological phase. Rightward/upward blue arrows indicate superconducting phase $\theta = 0$, whereas leftward/downward arrows stand for $\theta = \pi$.

groundstate wave-function in principle. Here we adopt an alternative way to understand the statistics followed by interchanging MFs.

The topological energy gap of the 1D system remains nonzero while manipulating two MFs, which gives us the freedom to perform unitary transformations for Hamiltonian (5.28). For simplicity, we put Hamiltonian (5.28) to purely real while manipulating $\gamma_{A,1}$ and $\gamma_{B,N}$, which is only possible when superconducting phase θ is either 0 or π . The phase of pairing function depends on the direction of site index i assignment since $|\Delta|e^{i\theta}c_ic_{i+1} = |\Delta|e^{i(\theta+\pi)}c_{i+1}c_i$. We denote $\theta = 0$ by rightward/upward arrows, $\theta = \pi$ must be represented by leftward/downward arrows (see figure 5.8). After exchanging two MFs, we end up with reversed arrows along the topological nanowire $\theta \rightarrow \theta + \pi$, indicating the sign flipping of uniform superconducting pairing Δ . To restore Hamiltonian back to its original form, we multiply a phase factor $e^{i\pi/2}$ to fermionic creation operator $f^\dagger = (\gamma_{A,1} - i\gamma_{B,N})/2$ where θ is absorbed into

$$f^\dagger = (\gamma_{A,1} - i\gamma_{B,N})/2 \rightarrow e^{i\pi/2}f^\dagger = (\gamma_{B,N} + i\gamma_{A,1})/2. \quad (5.31)$$

The above transformation gives

$$\gamma_{A,1} \rightarrow \gamma_{B,N}, \quad \gamma_{B,N} \rightarrow -\gamma_{A,1}, \quad (5.32)$$

which generates the non-Abelian statistics same as braiding of vortices in 2D spinless $p + ip$ superconductors as discussed above [22].

There are other possible schemes for realizing non-Abelian statistics in 1D nanowire system [122,

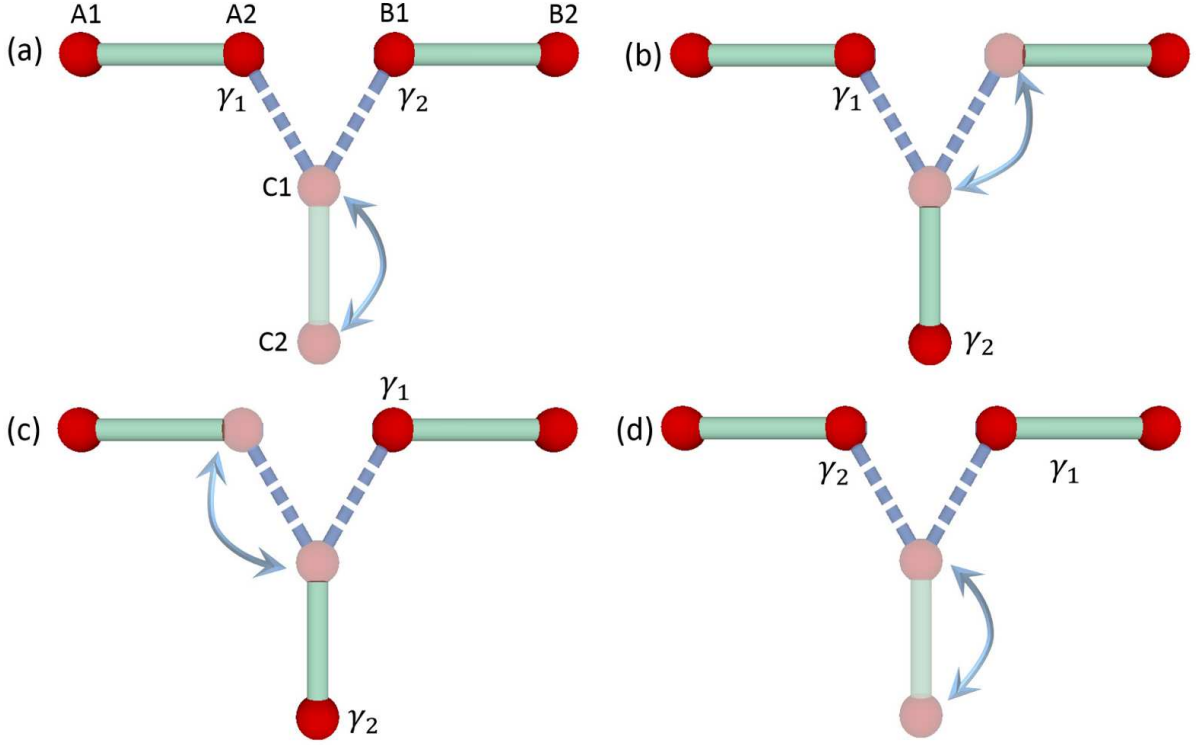


Figure 5.9: Schematic diagram for braiding MFs γ_1 and γ_2 (red balls) at positions A2 and B1 respectively [122]. Light blue arrows indicate finite couplings between MFs. Dashed blue lines are topological trivial segments.

[124, 130, 131]. Sau *et al.* [122] proposed to transport MFs by tuning couplings between MFs, instead of driving MFs all the way along the T junction by tuning chemical potential largely [128]. The Hamiltonian describes couplings between two MFs is

$$H_c = i\epsilon\gamma_1\gamma_2, \quad (5.33)$$

which can form a complex fermion $f^\dagger = (\gamma_1 - i\gamma_2)/2$ with finite energy. The number operator of fermion $n = f^\dagger f$ has double-degenerated groundstates $|0\rangle$ and $|1\rangle$ for $\epsilon \rightarrow 0$. An energy gap ϵ is created between eigenstates $|0\rangle$ and $|1\rangle$ for finite ϵ . In order to exchange MFs, three nanowires are put close to each other, and MFs at positions C1 and C2 are allowed to couple together, forming a complex fermion with finite energy (see figure 5.9(a)). To transport MF γ_2 , the authors adiabatically reduce the coupling between MFs at C1 and C2, and then increase that between B1 and C1. At zero coupling between C1 and C2, γ_2 is moved to position C2 (see figure 5.9(b)). Next, γ_1 at A2 is transported to B1 (see figure 5.9(c)). Finally, γ_2 is moved to position A2 to complete the interchanging of MFs (see figure 5.9(d)). The trajectories followed by γ_1 and γ_2 are

$$\begin{aligned} \gamma_1 &: A2 \rightarrow C1 \rightarrow B1, \\ \gamma_2 &: B1 \rightarrow C1 \rightarrow C2 \rightarrow C1 \rightarrow A2. \end{aligned} \quad (5.34)$$

It is proven that interchanging of γ_1 and γ_2 in this way follows non-Abelian statistics since either γ_1 or

γ_2 acquires a minus sign after exchanging positions [122].

In order to realize the above two braiding methods in nanowire networks [122, 128], some difficulties need to be overcome. In the proposal by Alicea *et al.* [128], manipulations of MFs by using gate voltages become quite difficult in 1D system since one has to adjust a number of local gate voltages precisely in the whole network. Failing to exert correct gate voltage at a single lattice site may break down the whole braiding process. Besides, transportations of MFs through T-junctions depend on details of the junction, which may be difficult to control [122, 134]. As for the scheme by Sau *et al.*, the coupling ϵ between MFs is oscillatory in space in topological superconductors as well as upon changing chemical potentials [135], which is not easy to be controlled accurately in any macroscopic way, meaning that transportations of MFs can hardly be carried out in designed ways. On the contrary, our proposal for manipulating MFs only requires tuning of local gate voltages at very small regions connecting two holes (see figure 5.3) and does not involve microscopic control on the couplings between MFs, which makes our scheme of braiding MFs robust.

5.5 Conclusion

We show that the Majorana fermions hosted by vortex cores in topological superconductors can be liberated from pinned vortices, transported and braided over the prepared tracks, taking advantages of the heterostructure of *s*-wave superconductor and spin-orbit coupled semiconductor. By solving the time-dependent Bogoliubov-de Gennes equation numerically, we monitor the time evolutions of Majorana fermion wave-functions and demonstrate the non-Abelian statistics of adiabatic braidings of Majorana fermions. The present scheme only requires local applications of gate voltages, and minimizes possible disturbances to the Majorana fermions, which might be a challenging issue in other proposals based on end Majorana fermions in one-dimensional superconductors where gate voltages are necessary along the whole system. Instead of exchanging positions of vortices hosting Majorana fermions, our scheme of braiding operation is much easier and faster for experimental realizations of non-Abelian statistics. As compared with the edge Majorana fermions in two-dimensional topological superconductors, the core Majorana fermions are protected by a larger energy gap, which relaxes the limitation on operating temperatures. Therefore, the present scheme provides a more feasible way for manipulating Majorana fermions.

Conclusion and Outlook

We propose a two-dimensional photonic crystal made of pure dielectric materials to realize a topologically nontrivial state characterized by the \mathbb{Z}_2 invariants in chapter 2. Each unit cell of the system consists of six infinitely long cylinders along the z axis. By detuning the lattice constants of the system, we demonstrate that the system is driven into a topological state protected by a pseudo-time-reversal symmetry, which is composed of the six-fold rotation symmetry C_6 and the conventional time-reversal symmetry respected by the Maxwell equations. The corresponding pseudospins are the angular momentum of wave function of the out-of-plane electric field of transverse magnetic modes. We confirm the nontrivial topology by demonstrating the helical edge states with opposite Poynting vector rotations and pseudospin-resolved Chern numbers. The present topological photonics with simple design backed up by the symmetry consideration can be fabricated relatively easy as compared with other proposals, and expected to leave impacts in the optics field.

The above idea of realizing topological photonic crystals by symmetry considerations can be extended to two-dimensional electronic systems. In chapter 3, we derive a pseudo-time-reversal-symmetry-protected topological state in honeycomb lattice. By taking a hexagonal unit cell that consists of six atomic sites, we arrive at the \mathbb{Z}_2 topological state simply by detuning the inter-hexagonal hopping integrals over the intra-hexagonal ones. A topological gap is opened at the Γ point accompanied by a band inversion between orbitals of opposite spatial parities. Similar to the case of photonic crystals, a pseudo-time-reversal symmetry associated with a pseudospin degree of freedom and Kramers doubling in the emergent orbitals are revealed based on the C_6 point group symmetry, which generates the \mathbb{Z}_2 topology. The nontriviality of the system is confirmed by the presences of topological edge states. For experimental implementations, we discuss that, along with many other possibilities, the molecular graphene realized by placing carbon monoxides (CO) periodically on Cu [111] surface is a promising platform to realize the present idea, where the hopping texture can be controlled by adding extra CO molecules. The size of topological gap is proportional to the difference between the inter and intra hopping energies, which can be larger than typical spin-orbit couplings by orders of magnitudes and potentially renders topological electronic transports available at high temperatures.

By breaking the time-reversal and inversion symmetries, we discuss a novel quantum anomalous Hall effect characterized by simultaneous charge and spin Chern numbers in chapter 4. We study a Mott insulator LaCrO_3 of perovskite structure with an inherent G-type antiferromagnetic ordering grown along the [001] direction. Inserting an atomic layer of inverse-perovskite material Sr_3PbO , the

Pb experiences the antiferromagnetic exchange field established by Cr atoms in the parent material. Based on first-principles calculations we confirm that the system reaches the novel topological state when the spin-orbit coupling of Pb is taken into considerations. We demonstrate that the novel quantum anomalous Hall effect by the spin-polarized edge current in a finite sample as well as an effective low-energy model. Supported by the antiferromagnetic exchange field and spin-orbit coupling in the compounds, no extrinsic operation is required for achieving the topological state as compared to our previous study for the electrically tunable one [17]. Importantly, both LaCrO_3 and Sr_3PbO are stable in bulk and match each other with only small lattice distortions, which makes the composite material easy to synthesize and promising for future applications in spintronics.

In the last chapter, we study topological superconductivities in a heterostructure composed of an s -wave superconductor with vortices, a ferromagnetic insulator and a semiconductor with strong Rashba-type spin-orbit coupling. We show that the Majorana fermions hosted by pinned vortex cores in the system can be liberated, transported and braided over the prepared tracks. By solving the time-dependent Bogoliubov-de Gennes equation numerically, we monitor the time evolutions of Majorana fermion wavefunctions and demonstrate the non-Abelian statistics of adiabatic braidings of Majorana fermions. The present scheme only requires local applications of gate voltages, and minimizes possible disturbances to the Majorana fermions, which might be a challenging issue in other proposals based on end Majorana fermions in one-dimensional superconductors where gate voltages are necessary along the whole system. Instead of exchanging positions of vortices hosting Majorana fermions, our scheme of braiding operation is much easier and faster for experimental realizations of non-Abelian statistics. As compared with the edge Majorana fermions in two-dimensional topological superconductors, the core Majorana fermions are protected by a larger energy gap, which relaxes the limitation on operating temperatures. Therefore, the present scheme provides a more feasible way for manipulating Majorana fermions, the first step for realizing topological quantum computing.

Acknowledgments

This thesis can not be accomplished without helps from dozens of people I have encountered during my stay at University of Tsukuba and National Institute for Materials Science. I would like to acknowledge them here.

First and foremost I wish to thank my advisor Prof. Xiao Hu who not only kindly provides me research assistantships during the whole period of study, but also encourages and inspires me to pursue new and interesting physics. He is one of the smartest people I know and can always make invaluable suggestions.

My gratitude extends to Prof. Kazuaki Sakoda, Prof. Yasuhiro Hatsugai and Prof. Takahide Yamaguchi for spending their precious time in reviewing my thesis. Prof. Sakoda is one of the pioneers who have developed theories of Dirac cones in photonic crystal. Without his enlightening seminars, I am afraid that I can not publish one of the most important papers to me. Prof. Hatsugai plays essential roles in the early developments of topological theories, and I have acquired a lot from his masterworks about topology. I would also like to take this opportunity to convey my sincere thanks to our group member Dr. Qi-Feng Liang who has spent numerous hours with me discussing new ideas and offered me many invaluable suggestions. I benefit a lot from his enthusiasm and insightful senses about physics.

I enjoy working and living in Japan as a graduate student, and would like express my sincere gratitudes to our group members Dr. Takuto Kawakami and Dr. Yuki Takahashi for their helps when I was troubled by Japanese language and also kindness for introducing interesting Japanese cultures to me. Meanwhile, I wish to thank secretaries of our group Ms. Makiko Shimada, Ms. Risa Okazawa, Ms. Nobue Kobayashi and Ms. Akemi Tateno for their kind and constant supports. I am grateful for the all group members: Dr. Madhav Ghimire, Dr. Bin Xi, Dr. Xue-yuan Hu, Dr. Rui Yu, Dr. Zhi Wang, Dr. Munehisa Matsumoto, Dr. Shi-Zhen Lin, Dr. Feng Liu as well as Mr. Zhao Huang for being helpful and friendly.

Lastly, I especially thank my dad, mom and my girl friend for being so supportive and providing their unconditional love when I have a hard and stressful time. I would not have made it this far without them. Having them in my life is the best thing ever happen to me.

ACKNOWLEDGMENTS

Bibliography

- [1] K. v. Klitzing, G. Dorda, and M. Pepper, “New method for high-accuracy determination of the fine-structure constant based on quantized Hall resistance,” *Phys. Rev. Lett.* **45**, 494 (1980).
- [2] R. B. Laughlin, “Quantized Hall conductivity in two dimensions,” *Phys. Rev. B* **23**, 5632 (1981).
- [3] B. I. Halperin, “Quantized Hall conductance, current-carrying edge states, and the existence of extended states in a two-dimensional disordered potential,” *Phys. Rev. B* **25**, 2185 (1982).
- [4] D. J. Thouless, M. Kohmoto, M. P. Nightingale, and M. den Nijs, “Quantized Hall conductance in a two-dimensional periodic potential,” *Phys. Rev. Lett.* **49**, 405 (1982).
- [5] Y. Hatsugai, “Chern number and edge states in the integer quantum Hall effect,” *Phys. Rev. Lett.* **71**, 3697 (1993).
- [6] F. D. M. Haldane, “Model for a quantum Hall effect without landau levels: Condensed-matter realization of the "parity anomaly",” *Phys. Rev. Lett.* **61**, 2015 (1988).
- [7] C. L. Kane and E. J. Mele, “Quantum spin Hall effect in graphene,” *Phys. Rev. Lett.* **95**, 226801 (2005).
- [8] C. L. Kane and E. J. Mele, “ Z_2 topological order and the quantum spin Hall effect,” *Phys. Rev. Lett.* **95**, 146802 (2005).
- [9] M. Hasan and C. Kane, “Colloquium: Topological insulators,” *Rev. Mod. Phys.* **82**, 3045 (2010).
- [10] B. A. Bernevig, T. L. Hughes, and S.-C. Zhang, “Quantum spin Hall effect and topological phase transition in HgTe quantum wells,” *Science* **314**, 1757 (2006).
- [11] X.-L. Qi and S.-C. Zhang, “Topological insulators and superconductors,” *Rev. Mod. Phys.* **83**, 1057 (2011).
- [12] F. Haldane and S. Raghu, “Possible Realization of Directional Optical Waveguides in Photonic Crystals with Broken Time-Reversal Symmetry,” *Phys. Rev. Lett.* **100**, 013904 (2008).
- [13] L.-H. Wu and X. Hu, “Scheme for Achieving a Topological Photonic Crystal by Using Dielectric Material,” *Phys. Rev. Lett.* **114**, 223901 (2015).
- [14] K. Sakoda, “Proof of the universality of mode symmetries in creating photonic Dirac cones.” *Opt. Express* **20**, 25181 (2012).

- [15] K. Sakoda, “Double Dirac cones in triangular-lattice metamaterials,” *Opt. Express* **20**, 9925 (2012).
- [16] L.-H. Wu and X. Hu, “Topological properties of electrons in honeycomb lattice with detuned hopping energy,” (2015), *submitted to Sci. Rep.*, arXiv:1509.00919 .
- [17] Q.-F. Liang, L.-H. Wu, and X. Hu, “Electrically tunable topological state in [111] perovskite materials with an antiferromagnetic exchange field,” *New J. Phys.* **15**, 063031 (2013).
- [18] H.-M. Weng, R. Yu, X. Hu, X. Dai, and Z. Fang, “Quantum anomalous Hall effect and related topological electronic states,” *Adv. Phys.* **64**, 227 (2015).
- [19] L.-H. Wu, Q.-F. Liang, and X. Hu, “Quantum anomalous Hall effect in a perovskite and inverse-perovskite sandwiched structure,” *J. Phys. Soc. Jpn.* **85**, 014706 (2015).
- [20] J. D. Sau, R. M. Lutchyn, S. Tewari, and S. Das Sarma, “Generic New Platform for Topological Quantum Computation Using Semiconductor Heterostructures,” *Phys. Rev. Lett.* **104**, 040502 (2010).
- [21] Q.-F. Liang, Z. Wang, and X. Hu, “Manipulation of majorana fermions by point-like gate voltage in the vortex state of a topological superconductor,” *Europhys. Lett.* **99**, 50004 (2012).
- [22] D. A. Ivanov, “Non-Abelian Statistics of Half-Quantum Vortices in p-Wave Superconductors,” *Phys. Rev. Lett.* **86**, 268 (2001).
- [23] L.-H. Wu, Q.-F. Liang, and X. Hu, “New scheme for braiding majorana fermions,” *Sci. Tech. Adv. Mater.* **15**, 064402 (2014).
- [24] A. Kitaev, “Periodic table for topological insulators and superconductors,” *AIP Conference Proceedings* **1134**, 22 (2009).
- [25] A. P. Schnyder, S. Ryu, A. Furusaki, and A. W. W. Ludwig, “Classification of topological insulators and superconductors in three spatial dimensions,” *Phys. Rev. B* **78**, 195125 (2008).
- [26] M. König, S. Wiedmann, C. Brüne, A. Roth, H. Buhmann, L. W. Molenkamp, X.-L. Qi, and S.-C. Zhang, “Quantum spin Hall insulator state in HgTe quantum wells,” *Science* **318**, 766 (2007).
- [27] Z. Wang, Y. Chong, J. Joannopoulos, and M. Soljačić, “Reflection-Free One-Way Edge Modes in a Gyromagnetic Photonic Crystal,” *Phys. Rev. Lett.* **100**, 013905 (2008).
- [28] Z. Wang, Y. Chong, J. D. Joannopoulos, and M. Soljačić, “Observation of unidirectional backscattering-immune topological electromagnetic states,” *Nature* **461**, 772 (2009).
- [29] K. Fang, Z. Yu, and S. Fan, “Realizing effective magnetic field for photons by controlling the phase of dynamic modulation,” *Nature Photon.* **6**, 782 (2012).
- [30] M. C. Rechtsman, J. M. Zeuner, Y. Plotnik, Y. Lumer, D. Podolsky, F. Dreisow, S. Nolte, M. Segev, and A. Szameit, “Photonic Floquet topological insulators,” *Nature* **496**, 196 (2013).
- [31] M. Hafezi, E. a. Demler, M. D. Lukin, and J. M. Taylor, “Robust optical delay lines with topological protection,” *Nature Phys.* **7**, 907 (2011).
- [32] M. Hafezi, S. Mittal, J. Fan, a. Migdall, and J. M. Taylor, “Imaging topological edge states in silicon photonics,” *Nature Photon.* **7**, 1001 (2013).

-
- [33] A. B. Khanikaev, S. H. Mousavi, W.-K. Tse, M. Kargarian, A. H. MacDonald, and G. Shvets, "Photonic topological insulators." *Nature Mater.* **12**, 233 (2013).
 - [34] Y. Hatsugai, "Explicit gauge fixing for degenerate multiplets: A generic setup for topological orders," *J. Phys. Soc. Jpn.* **73**, 2604 (2004).
 - [35] Y. Hatsugai, "Characterization of topological insulators: Chern numbers for ground state multiplet," *J. Phys. Soc. Jpn.* **74**, 1374 (2005).
 - [36] T. Fukui, Y. Hatsugai, and H. Suzuki, "Chern numbers in discretized Brillouin zone: Efficient method of computing (spin) Hall conductances," *J. Phys. Soc. Jpn.* **74**, 1674 (2005).
 - [37] D. Xiao, M.-C. Chang, and Q. Niu, "Berry phase effects on electronic properties," *Rev. Mod. Phys.* **82**, 1959 (2010).
 - [38] L. Fu and C. L. Kane, "Topological insulators with inversion symmetry," *Phys. Rev. B* **76**, 045302 (2007).
 - [39] D. Hsieh, D. Qian, L. Wray, Y. Xia, Y. S. Hor, R. Cava, and M. Z. Hasan, "A topological Dirac insulator in a quantum spin Hall phase," *Nature* **452**, 970 (2008).
 - [40] H. Zhang, C.-X. Liu, X.-L. Qi, X. Dai, Z. Fang, and S.-C. Zhang, "Topological insulators in Bi_2Se_3 , Bi_2Te_3 and Sb_2Te_3 with a single Dirac cone on the surface," *Nature Phys.* **5**, 438 (2009).
 - [41] R. Jackiw and C. Rebbi, "Solitons with fermion number $1/2$," *Phys. Rev. D* **13**, 3398 (1976).
 - [42] J. D. Joannopoulos, S. G. Johnson, J. N. Winn, and R. D. Meade, *Photonic Crystals: Molding the Flow of Light* (Princeton university press, 2011).
 - [43] P. R. Wallace, "The band theory of graphite," *Phys. Rev.* **71**, 622 (1947).
 - [44] K. S. Novoselov, A. K. Geim, S. V. Morozov, D. Jiang, Y. Zhang, S. V. Dubonos, I. V. Grigorieva, and A. A. Firsov, "Electric field effect in atomically thin carbon films," *Science* **306**, 666 (2004).
 - [45] K. S. Novoselov, A. K. Geim, S. V. Morozov, D. Jiang, M. I. Katsnelson, I. V. Grigorieva, S. V. Dubonos, and A. A. Firsov, "Two-dimensional gas of massless Dirac fermions in graphene," *Nature* **438**, 197 (2005).
 - [46] A. H. Castro Neto, F. Guinea, N. M. R. Peres, K. S. Novoselov, and A. K. Geim, "The electronic properties of graphene," *Rev. Mod. Phys.* **81**, 109 (2009).
 - [47] K. Sakoda and H. Zhou, "Role of structural electromagnetic resonances in a steerable left-handed antenna." *Optics express* **18**, 27371 (2010).
 - [48] X. Huang, Y. Lai, Z. H. Hang, H. Zheng, and C. T. Chan, "Dirac cones induced by accidental degeneracy in photonic crystals and zero-refractive-index materials." *Nature Mater.* **10**, 582 (2011).
 - [49] K. Sakoda, "Dirac cone in two- and three-dimensional metamaterials." *Opt. Express* **20**, 3898 (2012).
 - [50] K. Sakoda, "Photonic Dirac Cones Realized By Accidental Degeneracy on the Brillouin-Zone Boundary," *Int. J. Mod. Phys. B* **28**, 1441008 (2014).
 - [51] T. Ma, A. B. Khanikaev, S. H. Mousavi, and G. Shvets, "Guiding Electromagnetic Waves around

- Sharp Corners: Topologically Protected Photonic Transport in Metawaveguides,” *Phys. Rev. Lett.* **114**, 127401 (2015).
- [52] L.-G. Wang, Z.-G. Wang, J.-X. Zhang, and S.-Y. Zhu, “Realization of dirac point with double cones in optics,” *Opt. Lett.* **34**, 1510 (2009).
- [53] K. Sakoda, *Optical properties of photonic crystals* (Springer-Verlag, Berlin, 2004).
- [54] C. Kittel, *Introduction to solid state physics* (Wiley, 2005).
- [55] M. S. Dresselhaus, G. Dresselhaus, and A. Jorio, *Group theory: application to the physics of condensed matter* (Springer Science & Business Media, 2007).
- [56] L. Fu, “Topological crystalline insulators,” *Phys. Rev. Lett.* **106**, 106802 (2011).
- [57] T. Ochiai, “Photonic realization of the (2+1)-dimensional parity anomaly,” *Phys. Rev. B* **86**, 075152 (2012).
- [58] A. Taflove and S. C. Hagness, *Computational Electrodynamics: The Finite-Difference Time-Domain Method* (Artech House, 3rd edition, 2005).
- [59] E. Prodan, “Robustness of the spin- Chern number,” *Phys. Rev. B* **80**, 125327 (2009).
- [60] Y. Yang, Z. Xu, L. Sheng, B. Wang, D. Y. Xing, and D. N. Sheng, “Time-reversal-symmetry-broken quantum spin Hall effect,” *Phys. Rev. Lett.* **107**, 066602 (2011).
- [61] S. Hughes, L. Ramunno, J. F. Young, and J. E. Sipe, “Extrinsic optical scattering loss in photonic crystal waveguides: Role of fabrication disorder and photon group velocity,” *Phys. Rev. Lett.* **94**, 033903 (2005).
- [62] S. Mazoyer, J. P. Hugonin, and P. Lalanne, “Disorder-induced multiple scattering in photonic-crystal waveguides,” *Phys. Rev. Lett.* **103**, 063903 (2009).
- [63] A. K. Geim, “Graphene: Status and prospects,” *Science* **324**, 1530 (2009).
- [64] M. Ezawa, “A topological insulator and helical zero mode in silicene under an inhomogeneous electric field,” *New Journal of Physics* **14**, 033003 (2012).
- [65] M. Ezawa, “Valley-polarized metals and quantum anomalous Hall effect in silicene,” *Phys. Rev. Lett.* **109**, 055502 (2012).
- [66] K. F. Mak, K. He, J. Shan, and T. F. Heinz, “Control of valley polarization in monolayer MoS₂ by optical helicity,” *Nature Nanotech.* **7**, 494 (2012).
- [67] M. Ezawa, “Photoinduced topological phase transition and a single dirac-cone state in silicene,” *Phys. Rev. Lett.* **110**, 026603 (2013).
- [68] Y. Xu, B. Yan, H.-J. Zhang, J. Wang, G. Xu, P. Tang, W. Duan, and S.-C. Zhang, “Large-gap quantum spin Hall insulators in tin films,” *Phys. Rev. Lett.* **111**, 136804 (2013).
- [69] T. H. Hsieh, H. Lin, J. Liu, W. Duan, A. Bansil, and L. Fu, “Topological crystalline insulators in the snite material class,” *Nature Commun.* (2012), 10.1038/ncomms1969.
- [70] P. Dziawa, B. Kowalski, K. Dybko, R. Buczko, A. Szczerbakow, M. Szot, E. Łusakowska, T. Balasubramanian, B. M. Wojek, M. Berntsen, *et al.*, “Topological crystalline insulator states in Pb_{1-x}Sn_xSe,” *Nature Mater.* **11**, 1023 (2012).

-
- [71] S.-Y. Xu, C. Liu, N. Alidoust, M. Neupane, D. Qian, I. Belopolski, J. Denlinger, Y. Wang, H. Lin, L. Wray, *et al.*, “Observation of a topological crystalline insulator phase and topological phase transition in $\text{Pb}_{1-x}\text{Sn}_x\text{Te}$,” *Nature Commun.* **3**, 1192 (2012).
 - [72] T. Ando, “Quantum point contacts in magnetic fields,” *Phys. Rev. B* **44**, 8017 (1991).
 - [73] C. W. Groth, M. Wimmer, A. R. Akhmerov, and X. Waintal, “Kwant: a software package for quantum transport,” *New J. Phys.* **16**, 063065 (2014).
 - [74] Y. Imry and R. Landauer, “Conductance viewed as transmission,” *Rev. Mod. Phys.* **71**, S306 (1999).
 - [75] G. Tkachov and E. M. Hankiewicz, “Ballistic Quantum Spin Hall State and Enhanced Edge Backscattering in Strong Magnetic Fields,” *Phys. Rev. Lett.* **104**, 166803 (2010).
 - [76] W. Wu, S. Rachel, W.-M. Liu, and K. Le Hur, “Quantum spin Hall insulators with interactions and lattice anisotropy,” *Phys. Rev. B* **85**, 205102 (2012).
 - [77] M. Polini, F. Guinea, M. Lewenstein, H. C. Manoharan, and V. Pellegrini, “Artificial honeycomb lattices for electrons, atoms and photons,” *Nature Nanotech.* **8**, 625 (2013).
 - [78] L. Tarruell, D. Greif, T. Uehlinger, G. Jotzu, and T. Esslinger, “Creating, moving and merging Dirac points with a Fermi gas in a tunable honeycomb lattice,” *Nature* **483**, 302 (2012).
 - [79] B. Wunsch, F. Guinea, and F. Sols, “Dirac-point engineering and topological phase transitions in honeycomb optical lattices,” *New J. Phys.* **10**, 103027 (2008).
 - [80] K. K. Gomes, W. Mar, W. Ko, F. Guinea, and H. C. Manoharan, “Designer Dirac fermions and topological phases in molecular graphene,” *Nature* **483**, 306 (2012).
 - [81] M. Gibertini, A. Singha, V. Pellegrini, M. Polini, G. Vignale, A. Pinczuk, L. N. Pfeiffer, and K. W. West, “Engineering artificial graphene in a two-dimensional electron gas,” *Phys. Rev. B* , 8 (2009).
 - [82] S. G. Louie and C. H. Park, “Making massless dirac fermions from a patterned two-dimensional electron gas,” *Nano Lett.* **9**, 1793 (2009).
 - [83] G. Giovannetti, M. Capone, J. van den Brink, and C. Ortix, “Kekulé textures, pseudospin-one dirac cones, and quadratic band crossings in a graphene-hexagonal indium chalcogenide bilayer,” *Phys. Rev. B* **91**, 121417 (2015).
 - [84] C.-Y. Hou, C. Chamon, and C. Mudry, “Electron Fractionalization in Two-Dimensional Graphenelike Structures,” *Phys. Rev. Lett.* **98**, 186809 (2007).
 - [85] R. Yu, W. Zhang, H.-J. Zhang, S.-C. Zhang, X. Dai, and Z. Fang, “Quantized anomalous Hall effect in magnetic topological insulators,” *Science* **329**, 61 (2010).
 - [86] C.-Z. Chang, J. Zhang, X. Feng, J. Shen, Z. Zhang, M. Guo, K. Li, Y. Ou, P. Wei, L.-L. Wang, Z.-Q. Ji, Y. Feng, S. Ji, X. Chen, J. Jia, X. Dai, Z. Fang, S.-C. Zhang, K. He, Y. Wang, L. Lu, X.-C. Ma, and Q.-K. Xue, “Experimental observation of the quantum anomalous Hall effect in a magnetic topological insulator,” *Science* **340**, 167 (2013).
 - [87] Z. Qiao, S. A. Yang, W. Feng, W.-K. Tse, J. Ding, Y. Yao, J. Wang, and Q. Niu, “Quantum

- anomalous Hall effect in graphene from Rashba and exchange effects,” *Phys. Rev. B* **82**, 161414 (2010).
- [88] C. Liu, T. L. Hughes, X.-L. Qi, K. Wang, and S.-C. Zhang, “Quantum Spin Hall Effect in Inverted Type-II Semiconductors,” *Phys. Rev. Lett.* **100**, 236601 (2008).
- [89] M. Ezawa, “Spin valleytronics in silicene: Quantum spin hall–quantum anomalous Hall insulators and single-valley semimetals,” *Phys. Rev. B* **87**, 155415 (2013).
- [90] A. Widera and H. Schäfer, “Übergangsformen zwischen zintlphasen und echten salzen: Die verbindungen A_3BO (mit $A = Ca, Sr, Ba$ und $B = Sn, Pb$),” *Materials Research Bulletin* **15**, 1805 (1980).
- [91] T. Kariyado and M. Ogata, “Low-energy effective hamiltonian and the surface states of Ca_3PbO ,” *J. Phys. Soc. Jpn.* **81**, 064701 (2012).
- [92] A. A. Mostofi, J. R. Yates, Y.-S. Lee, I. Souza, D. Vanderbilt, and N. Marzari, “wannier90: A tool for obtaining maximally-localised Wannier functions,” *Comp. Phys. Commun.* **178**, 685 (2008).
- [93] M. Klintonberg, “The search for strong topological insulators,” (2010), arXiv:1007.4838 .
- [94] T. H. Hsieh, J. Liu, and L. Fu, “Topological crystalline insulators and dirac octets in antiperovskites,” *Phys. Rev. B* **90**, 081112 (2014).
- [95] G. Kresse and J. Furthmüller, “Efficient iterative schemes for *ab initio* total-energy calculations using a plane-wave basis set,” *Phys. Rev. B* **54**, 11169 (1996).
- [96] P. E. Blöchl, “Projector augmented-wave method,” *Phys. Rev. B* **50**, 17953 (1994).
- [97] G. Kresse and D. Joubert, “From ultrasoft pseudopotentials to the projector augmented-wave method,” *Phys. Rev. B* **59**, 1758 (1999).
- [98] J. P. Perdew, K. Burke, and M. Ernzerhof, “Generalized gradient approximation made simple,” *Phys. Rev. Lett.* **77**, 3865 (1996).
- [99] Z. Yang, Z. Huang, L. Ye, and X. Xie, “Influence of parameters U and J in the LSDA+ U method on electronic structure of the perovskites $LaMO_3$ ($M = Cr, Mn, Fe, Co, Ni$),” *Phys. Rev. B* **60**, 15674 (1999).
- [100] C.-X. Liu, “Anti-ferromagnetic crystalline topological insulators,” (2013), arXiv:1304.6455 .
- [101] R. S. K. Mong, A. M. Essin, and J. E. Moore, “Antiferromagnetic topological insulators,” *Phys. Rev. B* **81**, 245209 (2010).
- [102] D. Xiao, W. Zhu, Y. Ran, N. Nagaosa, and S. Okamoto, “Interface engineering of quantum Hall effects in digital transition metal oxide heterostructures,” *Nature Commun.* **2**, 596 (2011).
- [103] F. Wilczek, “Majorana returns,” *Nature Phys.* **5**, 614 (2009).
- [104] N. Read and D. Green, “Paired states of fermions in two dimensions with breaking of parity and time-reversal symmetries and the fractional quantum Hall effect,” *Phys. Rev. B* **61**, 267 (2000).
- [105] A. Y. Kitaev, “Unpaired majorana fermions in quantum wires,” *Physics-Uspekhi* **44**, 131 (2001).
- [106] M. Tinkham, *Introduction to Superconductivity* (Dover Publications, 2004).
- [107] A. Kitaev, “Fault-tolerant quantum computation by anyons,” *Annals of Physics* **303**, 2 (2003).

-
- [108] C. Nayak, S. H. Simon, A. Stern, M. Freedman, and S. D. Sarma, “Non-Abelian Anyons and Topological Quantum Computation,” *Rev. Mod. Phys.* **80**, 1083 (2007).
 - [109] C. Beenakker, “Search for Majorana Fermions in Superconductors,” *Annu. Rev. Condens. Matter Phys.* **4**, 113 (2013).
 - [110] G. Moore and N. Read, “Nonabelions in the fractional quantum hall effect,” *Nucl. Phys. B* **360**, 362 (1991).
 - [111] S. Tewari, S. Das Sarma, C. Nayak, C. Zhang, and P. Zoller, “Quantum Computation using Vortices and Majorana Zero Modes of a $p_x + i p_y$ Superfluid of Fermionic Cold Atoms,” *Phys. Rev. Lett.* **98**, 010506 (2007).
 - [112] M. Sato, Y. Takahashi, and S. Fujimoto, “Non-Abelian Topological Order in s-Wave Superfluids of Ultracold Fermionic Atoms,” *Phys. Rev. Lett.* **103**, 020401 (2009).
 - [113] L. Fu and C. Kane, “Superconducting Proximity Effect and Majorana Fermions at the Surface of a Topological Insulator,” *Phys. Rev. Lett.* **100**, 096407 (2008).
 - [114] A. Akhmerov, J. Nilsson, and C. Beenakker, “Electrically Detected Interferometry of Majorana Fermions in a Topological Insulator,” *Phys. Rev. Lett.* **102**, 216404 (2009).
 - [115] J. Alicea, “New directions in the pursuit of majorana fermions in solid state systems,” *Reports on Progress in Physics* **75**, 076501 (2012).
 - [116] J. Linder, Y. Tanaka, T. Yokoyama, A. Sudbø, and N. Nagaosa, “Unconventional Superconductivity on a Topological Insulator,” *Phys. Rev. Lett.* **104**, 067001 (2010).
 - [117] Q. Niu, D. J. Thouless, and Y.-S. Wu, “Quantized Hall conductance as a topological invariant,” *Phys. Rev. B* **31**, 3372 (1985).
 - [118] R. Lutchyn, J. Sau, and S. Das Sarma, “Majorana Fermions and a Topological Phase Transition in Semiconductor-Superconductor Heterostructures,” *Phys. Rev. Lett.* **105**, 077001 (2010).
 - [119] Y. Oreg, G. Refael, and F. von Oppen, “Helical Liquids and Majorana Bound States in Quantum Wires,” *Phys. Rev. Lett.* **105**, 177002 (2010).
 - [120] F. Hassler, A. R. Akhmerov, C.-Y. Hou, and C. W. J. Beenakker, “Anyonic interferometry without anyons: how a flux qubit can read out a topological qubit,” *New J. Phys.* **12**, 125002 (2010).
 - [121] A. C. Potter and P. A. Lee, “Multichannel generalization of kitaev’s majorana end states and a practical route to realize them in thin films,” *Phys. Rev. Lett.* **105**, 227003 (2010).
 - [122] J. D. Sau, D. J. Clarke, and S. Tewari, “Controlling non-Abelian statistics of Majorana fermions in semiconductor nanowires,” *Phys. Rev. B* **84**, 094505 (2011).
 - [123] B. van Heck, A. R. Akhmerov, F. Hassler, M. Burrello, and C. W. J. Beenakker, “Coulomb-assisted braiding of majorana fermions in a josephson junction array,” *New J. Phys.* **14**, 035019 (2012).
 - [124] T. Hyart, B. van Heck, I. C. Fulga, M. Burrello, A. R. Akhmerov, and C. W. J. Beenakker, “Flux-controlled quantum computation with majorana fermions,” *Phys. Rev. B* **88**, 035121 (2013).
 - [125] V. Mourik, K. Zuo, S. M. Frolov, S. R. Plissard, E. P. A. M. Bakkers, and L. P. Kouwenhoven,

- “Signatures of majorana fermions in hybrid superconductor-semiconductor nanowire devices,” *Science* **336**, 1003 (2012).
- [126] J. D. Sau, R. M. Lutchyn, S. Tewari, and S. D. Sarma, “Robustness of Majorana fermions in proximity-induced superconductors,” *Phys. Rev. B* **82**, 094522 (2010).
- [127] L.-H. Wu, Q.-F. Liang, Z. Wang, and X. Hu, “Chiral majorana fermion edge states in a heterostructure of superconductor and semiconductor with spin-orbit coupling,” *J. Phys.: Conf. Ser.* **393**, 012018 (2012).
- [128] J. Alicea, Y. Oreg, G. Refael, F. von Oppen, and M. P. a. Fisher, “Non-Abelian statistics and topological quantum information processing in 1D wire networks,” *Nature Phys.* **7**, 412 (2011).
- [129] Y. L. Loh, S. N. Taraskin, and S. R. Elliott, “Fast Time-Evolution Method for Dynamical Systems,” *Phys. Rev. Lett.* **84**, 2290 (2000).
- [130] M. Burrello, B. van Heck, and A. R. Akhmerov, “Braiding of non-abelian anyons using pairwise interactions,” *Phys. Rev. A* **87**, 022343 (2013).
- [131] P. Bonderson, M. Freedman, and C. Nayak, “Measurement-only topological quantum computation,” *Phys. Rev. Lett.* **101**, 010501 (2008).
- [132] M. Stone and S.-B. Chung, “Fusion rules and vortices in $p_x + i p_y$ superconductors,” *Phys. Rev. B* **73**, 014505 (2006).
- [133] G. Volovik, “Fermion zero modes on vortices in chiral superconductors,” *J. Exp. Theor. Phys. Lett.* **70**, 609 (1999).
- [134] D. Clarke, J. Sau, and S. Tewari, “Majorana fermion exchange in quasi-one-dimensional networks,” *Phys. Rev. B* **84**, 035120 (2011).
- [135] M. Cheng, R. M. Lutchyn, V. Galitski, and S. Das Sarma, “Tunneling of anyonic majorana excitations in topological superconductors,” *Phys. Rev. B* **82**, 094504 (2010).
- [136] Y. Hatsugai, T. Fukui, and H. Aoki, “Topological aspects of graphene,” *Eur. Phys. J. Spec. Top.* **148**, 133 (2007).

List of Publications

1. Long-Hua Wu and Xiao Hu, “*Scheme for Achieving a Topological Photonic Crystal by Using Dielectric Material*”, Physical Review Letters, **114**, 223901 (2015).
2. Long-Hua Wu, Qi-Feng Liang, and Xiao Hu, “*Quantum Anomalous Hall Effect in a Perovskite and Inverse-Perovskite Sandwich Structure*”, Journal of the Physical Society of Japan, **85**, 014706 (2016).
3. Long-Hua Wu, Qi-Feng Liang, and Xiao Hu, “*New Scheme for Braiding Majorana Fermions*”, Science and Technology of Advanced Materials, **15**, 064402 (2014).
4. Long-Hua Wu, Qi-Feng Liang, Zhi Wang, and X. Hu, “*Chiral Majorana Fermion Edge States in a Heterostructure of Superconductor and Semiconductor with Spin-Orbit Coupling*”, Journal of Physics: Conference Series, **393**, 012018(2012).
5. Long-Hua Wu, “*Topological Properties of Electrons in Honeycomb Lattice with Detuned Hopping Energy*”, submitted to Scientific Reports (preprint arXiv:1509.00919).
6. Madhav P. Ghimire, Long-Hua Wu, and Xiao Hu, “*Half Metallic Ferrimagnetism in Hole-doped Lanthanide Iradates*”, Journal of Superconductivity and Novel Magnetism, **28**, 917 (2015).
7. Qi-Feng Liang, Long-Hua Wu, and Xiao Hu, “*Electrically Tunable Topological State in [111] Perovskite Materials with an Antiferromagnetic Exchange Field*”, New Journal of Physics, **15**, 063031 (2013).

Low-Energy Model for Honeycomb Lattice

A.1 Honeycomb lattice and Dirac cones

Honeycomb lattice can host electrons with Dirac-like linear dispersion [43]. A minimal tight-binding Hamiltonian describing dispersion relation of π electron in graphene is [46]

$$H_0 = -t \sum_{\langle i,j \rangle, \sigma} (a_{i,\sigma}^\dagger b_{j,\sigma} + H.c.), \quad (\text{A.1})$$

where $a_{i,\sigma}$ ($b_{i,\sigma}$) annihilates a π electron at site i of sublattice A (B) and spin σ , $\langle i,j \rangle$ runs over two *nearest neighbors* (NNs) with hopping energy t (see figure 1.3). An effective 2×2 Dirac Hamiltonian at the K and K' points can be obtained by a straightforward Fourier transformation $a_{j,\sigma} = \sum_{\mathbf{k}} a_{\mathbf{k},\sigma} e^{i\mathbf{k} \cdot \mathbf{r}_j}$ and $b_{j,\sigma} = \sum_{\mathbf{k}} b_{\mathbf{k},\sigma} e^{i\mathbf{k} \cdot \mathbf{r}_j}$ with \mathbf{r}_j the position of site j [46, 136]. However, we provide a slightly different view of the Dirac physics in honeycomb lattice. The hopping matrix on the basis $[a_\sigma, b_\sigma]$ within a unit cell is

$$h_0 = -t \begin{pmatrix} 0 & 1 \\ 1 & 0 \end{pmatrix} \quad (\text{A.2})$$

with eigenvalues $\mp t$ and corresponding eigenvectors

$$\Psi_+ = \frac{1}{\sqrt{2}} \begin{pmatrix} 1 \\ 1 \end{pmatrix}, \Psi_- = \frac{1}{\sqrt{2}} \begin{pmatrix} -1 \\ 1 \end{pmatrix}, \quad (\text{A.3})$$

which are nothing but bonding and antibonding states of p_z electrons at two sublattice sites. It is interesting to know that Ψ_\pm are of opposite spatial parities under the inversion operator \mathcal{I} with inversion center at the bond linking two sublattice sites

$$\mathcal{I}\Psi_\pm = \pm \Psi_\pm. \quad (\text{A.4})$$

The hopping matrix along the lattice vector \vec{a}_1 , \vec{a}_2 and $\vec{a}_3 = \vec{a}_2 - \vec{a}_1$ on the basis $[a_\sigma, b_\sigma]$ are

$$h_1 = 0, h_2 = h_3 = -t \begin{pmatrix} 0 & 0 \\ 1 & 0 \end{pmatrix}, \quad (\text{A.5})$$

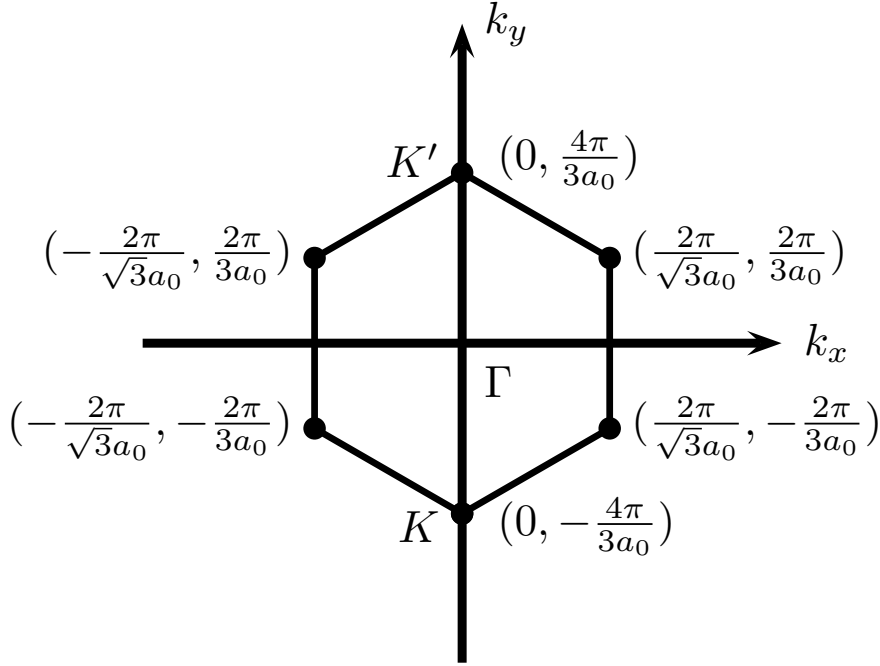


Figure A.1: Brillouin zone for honeycomb lattice.

Projecting above hopping matrix onto the basis $[\Psi_+, \Psi_-]$, we have

$$\tilde{h}_1 = 0, \tilde{h}_2 = \tilde{h}_3 = -\frac{t}{2} \begin{pmatrix} 1 & 1 \\ -1 & -1 \end{pmatrix}. \quad (\text{A.6})$$

Grouping sublattices A and B into a unit cell, the honeycomb lattice can be conveniently viewed as a triangular lattice with lattice vectors \vec{a}_1 and \vec{a}_2 , as shown in figure 1.3.

A Fourier transformation $\Psi_{\mathbf{r},\pm} = \sum_{\mathbf{k}} \Psi_{\mathbf{k},\pm} \exp(i\mathbf{k} \cdot \mathbf{r})$ immediately gives the momentum-space Hamiltonian

$$H_0(\mathbf{k}) = -t \begin{pmatrix} 1 + \omega(\mathbf{k}) & \gamma(\mathbf{k}) \\ \gamma^*(\mathbf{k}) & -1 - \omega(\mathbf{k}) \end{pmatrix} \quad (\text{A.7})$$

on the basis $\Psi_{\mathbf{k}} = [\Psi_+, \Psi_-]$, where $\omega(\mathbf{k}) = \cos[\mathbf{k} \cdot \vec{a}_2] + \cos[\mathbf{k} \cdot (\vec{a}_2 - \vec{a}_1)]$ and $\gamma(\mathbf{k}) = i \sin[\mathbf{k} \cdot \vec{a}_2] + i \sin[\mathbf{k} \cdot (\vec{a}_2 - \vec{a}_1)]$. In a simple case with $k_x = 0$, the Hamiltonian in Eq. (A.7) along the k_y axis reduces to

$$H_y(k_y) = -t \begin{bmatrix} 1 + \cos(k_y a_0/2) + \cos(k_y a_0) & i \sin(k_y a_0/2) + i \sin(k_y a_0) \\ -i \sin(k_y a_0/2) - i \sin(k_y a_0) & -1 - \cos(k_y a_0/2) - \cos(k_y a_0) \end{bmatrix} \quad (\text{A.8})$$

with $a_0 = |\vec{a}_1|$ the lattice constant and $k_y \in [-\frac{4\pi}{3a_0}, \frac{4\pi}{3a_0}]$. At the corner of the Brillouin zone of honeycomb lattice $K = (0, -\frac{4\pi}{3a_0})$ and the $K' = (0, \frac{4\pi}{3a_0})$ points (see figure A.1), there are two Dirac cones, as shown in figure A.2. The degeneracy is protected by the equivalence of two sublattices, known as sublattice symmetry [136].

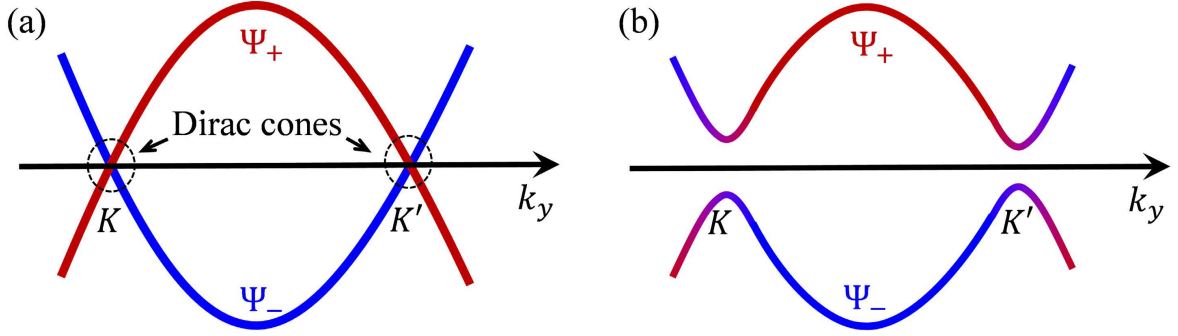


Figure A.2: Dispersion relation for honeycomb lattice (a) without and (b) with complex next-nearest-neighbor hopping included.

It was shown first that a quantum anomalous Hall effect (QAHE) can be realized when complex hopping integrals $t' = t_1 \exp(i\phi)$ among *next-nearest-neighbor* (NNN) sites of honeycomb lattice are taken into account [6] (see figure 1.3), where $t_1 = |t'|$ is the magnitude of t' . The hopping matrices projected onto the basis $[\Psi_+, \Psi_-]$ are

$$\tilde{h}'_1 = \tilde{h}'_3 = \tilde{h}'_2^\dagger = t_1 \begin{pmatrix} \cos \phi & i \sin \phi \\ i \sin \phi & \cos \phi \end{pmatrix} \quad (\text{A.9})$$

along the $\vec{a}_1, \vec{a}_2 - \vec{a}_1$ and \vec{a}_2 directions respectively. Transforming the Hamiltonian describing NNN hoppings into momentum space, we have

$$\begin{aligned} H_{\text{NNN}} &= 2t_1 \begin{bmatrix} \cos \phi \sum_{i=1,3} \cos(\mathbf{k} \cdot \vec{a}_i) & -\gamma'(\mathbf{k}) \sin \phi \\ -\gamma'(\mathbf{k}) \sin \phi & \cos \phi \sum_{i=1,3} \cos(\mathbf{k} \cdot \vec{a}_i) \end{bmatrix} \\ &= \left[2t_1 \cos \phi \sum_{i=1,3} \cos(\mathbf{k} \cdot \vec{a}_i) \right] \sigma_0 - [2t_1 \gamma'(\mathbf{k}) \sin \phi] \sigma_x \end{aligned} \quad (\text{A.10})$$

with $\gamma'(\mathbf{k}) = \sin(\mathbf{k} \cdot \vec{a}_1) - \sin(\mathbf{k} \cdot \vec{a}_2) + \sin(\mathbf{k} \cdot \vec{a}_3)$, which specifies hybridizations of bonding and antibonding states. It is easy to see that the first term in Eq. (A.10) simply shifts the location of the Fermi levels, and cannot affect topology of the system. The second term in Eq. (A.10) is $\pm 3\sqrt{3}t_1 \sin \phi$ at the K' and K points respectively. The effective low-energy Hamiltonian near the two valleys is

$$H[\mathbf{k} \rightarrow K(K')] = \begin{pmatrix} v_f k_x & 3\sqrt{3}v t_1 \sin \phi - i v_f v k_y \\ 3\sqrt{3}v t_1 \sin \phi + i v_f v k_y & -v_f k_x \end{pmatrix} \quad (\text{A.11})$$

on the basis $[\Psi_+, \Psi_-]$, where $v_f = \sqrt{3}a_0 t/2$. Similar to Section 1.2.3, the Berry curvatures at the two valleys can be evaluated easily and they are both $1/2$ or $-1/2$ depending on value of ϕ [6], which gives a QAHE characterized by the Chern number ± 1 .

A.2 Hamiltonian on basis of sublattice

Expanding Eqs. (A.7) and (A.10) around the K point up to the lowest order of \mathbf{k} on the basis $[a_{\mathbf{k}}, b_{\mathbf{k}}]$, we arrive at

$$H(\mathbf{k}) = \begin{pmatrix} 3\sqrt{3}\nu t_1 \sin \phi - 3t_1 \cos \phi & -v_f(k_x - i\nu k_y) \\ -v_f(k_x + i\nu k_y) & -3\sqrt{3}\nu t_1 \sin \phi - 3t_1 \cos \phi \end{pmatrix} \quad (\text{A.12})$$

where $\nu = \pm 1$ at the K and K' points respectively, $\mathbf{k} = (k_x, k_y)$ is measured from the K and K' points. The couplings between the bonding and antibonding states do not equal to zero even at the $K(K')$ points for all $\phi \neq n\pi$ ($n \in \mathbb{Z}$), i.e. a band gap opened at the $K(K')$ points are of opposite signs. With the broken time-reversal symmetry, the gap opened here is expected topologically nontrivial.

It has been revealed that the intrinsic spin-orbit coupling (SOC) in honeycomb lattice can provide this complex hopping integrals with $|\phi| = \pi/2$ [7, 8]. For the spin-up channel with $\phi = \pi/2$, the SOC term in the diagonal part of Hamiltonian (A.12) reduces to

$$H_{\uparrow}(\mathbf{k}) = \begin{pmatrix} 3\sqrt{3}\nu t_1 & 0 \\ 0 & -3\sqrt{3}\nu t_1 \end{pmatrix}. \quad (\text{A.13})$$

Due to the time-reversal symmetry, ϕ must be $-\pi/2$ to ensure a zero total net flux passing the system

$$H_{\downarrow}(\mathbf{k}) = \begin{pmatrix} -3\sqrt{3}\nu t_1 & 0 \\ 0 & 3\sqrt{3}\nu t_1 \end{pmatrix}. \quad (\text{A.14})$$

Summarizing Eqs. (A.13) and (A.14), the effective Hamiltonian of SOC at the two valleys K and K' is

$$H_{\text{soc}} = \lambda \tau_z \sigma_z s_z \quad (\text{A.15})$$

with s_z the Pauli matrix for spin degree of freedom, τ_z for the valley and σ_z for the sublattice, $\lambda = 3\sqrt{3}t_1$ the strength of spin-orbit coupling. The non-vanishing SOC in Eq. (3.5) opens a bulk band gap at the $K(K')$ points, which drives spinful electrons into a topological state with preserved time-reversal symmetry, known as quantum spin Hall effect (QSHE) [9, 11].

Winding Number and One-Dimensional Kitaev Model

A toy model describing an one-dimensional (1D) spinless p -wave superconductor was given in Eq. (5.28). By transforming the Hamiltonian (5.28) into the momentum space with the lattice constant taken as 1, we have

$$H_{\text{Kitaev}}(k) = \tau_x \Delta \sin k + \tau_z (2t \cos k - \mu) = d_x \tau_x + d_z \tau_z, \quad (\text{B.1})$$

on the basis $[c, c^\dagger]$ with τ_x and τ_z the Pauli matrices and $\Delta = |\Delta|e^{i\theta}$. Without losing generality, we assume $\phi = 0$. A straightforward unitary transformation gives

$$H(k) = U^\dagger H_{\text{Kitaev}}(k) U = -d_x \tau_y + d_z \tau_x \quad (\text{B.2})$$

with

$$U = \frac{1}{\sqrt{2}} \begin{pmatrix} 1 & 1 \\ -i & i \end{pmatrix}, \quad (\text{B.3})$$

for the convenience of analytical calculations in later part. The eigenenergies of Eq. (B.2) are

$$E_\pm = \pm \sqrt{d_x^2 + d_z^2} = \pm \sqrt{|\Delta|^2 \sin^2 k + (2t \cos k - \mu)^2} \quad (\text{B.4})$$

with corresponding eigenvectors

$$\Psi_\pm = \frac{1}{\sqrt{2}} \begin{bmatrix} \frac{id_x + d_z}{\sqrt{d_x^2 + d_z^2}} \\ \pm 1 \end{bmatrix}.$$

The accumulated Berry (Zak) phase for the occupied bands is

$$\Phi = \int_0^{2\pi} dk \langle \Psi_- | i \partial_k | \Psi_- \rangle = \frac{1}{2} \int_0^{2\pi} \frac{d_x \partial_k d_z - d_z \partial_k d_x}{d_x^2 + d_z^2}, \quad (\text{B.5})$$

which has a singularity when $d_x^2 + d_z^2 = 0$. By denoting $z = d_x + i d_z$, we have

$$\frac{dz}{z} = \frac{\partial_k d_x + i \partial_k d_z}{d_x + i d_z} = \frac{d_x \partial_k d_x + d_z \partial_k d_z}{d_x^2 + d_z^2} + i \frac{d_x \partial_k d_z - d_z \partial_k d_x}{d_x^2 + d_z^2}, \quad (\text{B.6})$$

indicating that Eq. (B.5) can be rewritten as an imaginary part of the contour integration of dz/z

$$\Phi = \frac{1}{2i} \text{Im} \oint_C \frac{dz}{z} \quad (\text{B.7})$$

In the case that the singular point $|z| = 0$ is inside the contour C , the Berry phase is $\Phi = 2\pi i/(2i) = \pi \bmod 2\pi$ by the Cauchy integral formula, resulting in a winding number $\nu = 1$. The modulus 2π comes from the gauge variance feature of the Berry phase. When the singular point is outside of the contour C , the system is topologically trivial with a winding number $0 \bmod 2\pi$.

Let us return back to the Kitaev model with $d_x = \Delta \sin k$ and $d_z = 2t \cos k - \mu$. The contour C parameterized by $k \in [0, 2\pi]$ is an ellipse. When $|\mu| > 2t$, the system is in a trivial state since the contour C does not include the original point $|z| = 0$. For $|\mu| < 2t$, the original point locates inside the C , which results in a topological state.